2020

Dosimetry and 4D Modelling for Advanced Radiotherapy Treatments: Towards MRI-Guided Lung SBRT

Natalia F. Roberts

UNIVERSITY
OF WOLLONGONG
AUSTRALIA

Dosimetry and 4D Modelling for Advanced Radiotherapy Treatments: Towards MRI-Guided Lung SBRT

Natalia F. Roberts
Bachelor of Medical Radiation Physics Advanced (Honours)

This thesis is presented as part of the requirements for the conferral of the degree:

Doctor of Philosophy

Supervisors:
Snr. Prof. Peter Metcalfe
Dr. Brad Oborn
Assoc. Prof. Lois Holloway

The University of Wollongong
School of Physics

2020

This research has been conducted with the support of an Australian Government Research Training Program Scholarship and a Centre for Oncology Education and Research Translation PhD Scholarship Top-Up.

Declaration

I, *Natalia F. Roberts*, declare that this thesis is submitted in partial fulfilment of the requirements for the conferral of the degree *Doctor of Philosophy*, from the University of Wollongong, is wholly my own work unless otherwise referenced or acknowledged. This document has not been submitted for qualifications at any other academic institution.

Natalia F. Roberts

July 23, 2020

Abstract

A major problem for radiation therapy of lung cancer is respiration-induced motion, which causes both the tumour and surrounding normal tissue to move during treatment. This motion often results in inadequate target coverage and increases the likelihood of additional healthy tissue exposure; therefore detracting from the therapeutic benefits and increasing the risk of radiation induced toxicity. Some motion-management techniques include additional treatment margins to encompass the range of tumour motion, monitoring the respiratory cycle and treating only when in a particular phase i.e. respiratory gating, or imaging the tumour during treatment and adapting the radiation beam aperture to follow the tumour i.e. image guidance and tracking.

Magnetic-Resonance-Imaging (MRI)-linacs are a form of image guided radiotherapy, these systems offer high soft-tissue contrast imaging (with MRI) while simultaneously treating with a therapeutic radiation beam (linear accelerator or linac). The effects of the magnetic field on dose deposition and detector response should be well understood to safely translate this technology to clinical treatments. For MRI-linacs where the magnetic field is inline with respect to the beam, the effects of the magnetic field on electron trajectories in lung can be significant and therefore it is important to study the impacts of this on dose distribution in order to treat lung SBRT on these systems.

In this thesis, a 4D Monte Carlo dose calculation tool is developed and implemented for assessing current radiotherapy techniques for lung Stereotactic Body Radiotherapy (SBRT). In recent years there has been an increasing interest in MRI-guided radiotherapy and its potential to be used for lung SBRT. With the higher doses per fraction used for SBRT there is an increased need for highly accurate dose calculations and localised delivery; particularly for MRI-linac lung treatments, where the magnetic field strongly

influences lung tissue and tumour dose distributions. This thesis also presents work towards translating the 4D Monte Carlo method for inline MRI-linacs.

A preliminary study was performed to assess the accuracy of the 4D Monte Carlo dose calculation tool for current treatments using a dynamic lung phantom. Comparing the dose from different calculation methods, the 4D Monte Carlo dose was in closest agreement to measurements. The study was extended further to investigate both motion and delivery tolerances for these treatments. Multi-leaf collimator (MLC) tolerances were shown to be specific to the motion-management treatment technique used for the phantom study. A lung patient study which considered varying tumour volumes and motions showed the impact of the interplay effect on treatment plans was minimal. MLC tolerances had a larger impact on these plans however no obvious trends were observed in relation to the size or motion amplitude of tumours. A similar study was translated to inline MRI-linac systems, considering in the first instance uniform magnetic fields of varying strengths. MLC tolerances did not vary with magnetic field strength for the plans considered, that is they remained the same as the 0 T plans.

In order to translate this 4D Monte Carlo tool to an MRI-linac system, the magnetic field and its effects on the dose deposition should be well understood and accurately modelled. To achieve this it is essential to perform measurements to characterise the radiation beam in the presence of the magnetic field using appropriate dosimeters. The microDiamond (PTW, Freiburg, Germany) and MO*Skin*$^{\text{TM}}$ (CMRP, Wollongong, Australia) detectors were used to measure the magnetically focused electron contamination region that is inherent to the Australian MRI-linac system. The skin dose, as measured with the MO*Skin*$^{\text{TM}}$, was 369.1% for a 11.8 $\times$ 11.5 cm^2 field. Techniques using Gafchromic® film were also developed in order to acquire accurate percentage depth doses (PDDs) and profiles. Using the experimental data, beam modelling was then carried out in a convolution-based treatment planning system (Pinnacle^3) and with Monte Carlo (Geant4). Initial results showed that Monte Carlo should be used alongside the treatment planning system to accurately model the dose distributions.

Overall, a 4D Monte Carlo dose calculation tool was developed which can be used

for quality assurance of treatment plans for current techniques of dynamic tumours and MRI-guided radiotherapy treatments. Methods were developed to experimentally and computationally characterise the Australian MRI-linac in order to translate the 4D tool for this system in future. This thesis constitutes steps towards the clinical implementation of an inline MRI-linac for lung SBRT.

Acknowledgements

This research was funded by an Australian Government Research Training Program Scholarship and a Centre for Oncology Education and Research Translations (CONCERT) PhD Scholarship Top-Up.

Firstly, I would like to acknowledge and thank my supervisors for their continuous support throughout my PhD. To Prof. Peter Metcalfe for always being available for coffee meetings and helping me move forward when I had problems. To Assoc. Prof. Lois Holloway for her advice over the years and motivating me to keep going; her cheery attitude towards research was highly infectious. To Dr. Brad Oborn for putting up with my constant emails (on any day and at any hour) about my simulation problems and for always being keen to discuss medical physics over beer.

I would like to thank all the medical physics staff and researchers at the Centre for Medical Radiation Physics (CMRP, UOW), Ingham Institute, Liverpool Hospital and Wollongong Hospital for their support and advice, and allowing me to use equipment. Special thanks goes to Dr Urszula Jelen who spent countless hours with me in the MRI-linac bunker, sharing her knowledge of the system and most importantly for making those long shifts in the bunker enjoyable. Thank you to Dr Matthew Williams for sharing his wealth of knowledge of clinical medical physics with me, he was an invaluable asset to my PhD. I would also like to thank Trent Causer and Lauren Bell, for all the times I could count on them to let me through the physics office doors at Wollongong hospital and answering all the clinical questions I threw at them during our bouldering sessions.

I would like to acknowledge fellow PhD students (and friends) who helped with experiments and added to my knowledge along the way, Sarah Alnaghy, Trent Causer,

Thahabah Alharthi and Elizabeth Patterson. Thanks also to my friends (from many areas of life) who have been a backbone to my sanity, particularly Emily Debrot, Elisa Jager and James Archer.

To Mum, Dad, Samantha, Heidi and Chris, thank you for the love and support you provide. I can always count on my family to make me laugh. Finally, I would like to thank Jarryd, for continuously helping me to see the light at the end of the PhD tunnel!

Publications and Presentations

Publications:

N. F. Roberts, M. Williams, L. Holloway, P. Metcalfe, B. M. Oborn, 2019. "NOTE: 4D Monte Carlo dose calculations for pre-treatment quality assurance of VMAT SBRT: a phantom-based feasibility study", Phys. Med. Biol. 64 (21), 21NT01 (10pp).

N. F. Roberts, E. Patterson, U. Jelen, T. Causer, L. Holloway, G. Liney, M. Lerch, A. B. Rosenfeld, D. Cutajar, B. M. Oborn P. Metcalfe, 2019. "Experimental characterization of magnetically focused electron contamination at the surface of a high-field inline MRI-linac", Med. Phys. 46 (12), 5780-5789.

N. Roberts, B. Oborn, U. Jelen, B. Dong, J. Begg, A. George, S. J. Alnaghy, T. Causer, T. Alharthi, L. Holloway, P. Metcalfe, 2019. "Modelling the x-ray source for the Australian MRI-Linac", J. Phys: Conf. Ser. 1154, p. 012025.

U. Jelen, B. Dong, J. Begg, N. Roberts, B. Whelan, P. Keall, G. Liney, 2020. "Dosimetric optimization and commissioning of a high field inline MRI-linac", Front. Oncol., 10:136.

S. J. Alnaghy, T. Causer, N. Roberts, B.M. Oborn, U. Jelen, B. Dong, M. Gargett, J. Begg, G. Liney, M. Petasecca , A.B. Rosenfeld, L. Holloway, P. Metcalfe, "High Resolution Silicon Array Detector Implementation in an Inline MRI-Linac", Med. Phys., accepted, doi = 10.1002/mp.14016.

S. J. Alnaghy, T. Causer, M. Gargett, N. Roberts , M. Petasecca , B.M. Oborn, A.B. Rosenfeld, L. Holloway, P. Metcalfe, 2019. "A Feasibility Study for High

Resolution Silicon Array Detector Performance in the Magnetic Field of a Permanent Magnet System", Med. Phys. 46 (9), 4224-4232.

L. Madden, J. Archer, E. Li, U. Jelen, B. Dong, N. Roberts, L. Holloway, A. Rosenfeld, 2019. "First measurements with a plastic scintillation dosimeter at the Australian MRI-LINAC", Phys. Med. Biol. 64 (17), 175015 (8pp).

E.M. Pogson, S. Arumugam, C.R. Hansen, M. Currie, S.J .Blake, N. Roberts, M. Carolan, P. Vial, T. Alharthi, L. Holloway, D.I. Thwaites, 2018. "Comparison of multi-institutional pre-treatment verification for VMAT of nasopharynx with delivery errors", Phys. Med. 53, pp. 25-31.

Presentations:

N. Roberts, B. Oborn, J. Begg, A. George, S.J. Alnaghy, T. Causer, T. Alharthi, L. Holloway, P. Metcalfe, "Modelling of a novel x-ray source for MR-guided radiotherapy", International Conference on Monte Carlo Techniques for Medical Applications, Naples, 15-18 October, 2017. Oral Presentation.

N. Roberts, L.Holloway, B. Oborn, P. Metcalfe, "Effects of MLC positional errors on the treatment of dynamic tumours: a lung phantom-based Monte Carlo study", Engineering and Physical Sciences in Medicine, Hobart, 29 October - 1 November, 2017. Oral Presentation.

N. Roberts, B. Oborn, U. Jelen, B. Dong, J. Begg, A. George, S.J. Alnaghy, T. Causer, T. Alharthi, L. Holloway, P. Metcalfe, "Modelling the x-ray source for the Australian MRI-Linac", Micro-Mini & Nano-Dosimetry & Innovative Technologies in Radiation Therapy, Mooloolaba, 6-11 February, 2018. Oral Presentation.

N. Roberts, B. Oborn, U. Jelen, T. Causser, F. Su, L. Holloway, M. Lerch, P. Metcalfe, "The dose response of the PTW 60019 microDiamond in magnetic fields: Characterisation for the Australian MRI-linac", 6th MR in RT, Utrecht, 1-3 July, 2018.

Poster Presentation.

N. Roberts, U.Jelen, B. Oborn, L.Holloway, G. Liney, M. Lerch, P. Metcalfe, “Diamond dosimetry on the Australian MRI-linac”, Engineering and Physical Sciences in Medicine, Adelaide, 29 October - 31 October, 2018. Oral Presentation.

N. Roberts, E. Patterson , U. Jelen, T. Causer, L. Holloway, G. Liney, M. Lerch, A. B. Rosenfeld, D. Cutajar, B. M. Oborn, P. Metcalfe “Skin Dose Measurements on an Inline 1 T MRI-linac”, 7th MR in RT, Toronto, 23-25 June, 2019. Oral Presentation.

Invited Presentations:

N. Roberts, B. Oborn, U. Jelen, T. Causser, F. Su, L. Holloway, M. Lerch, P. Metcalfe, “The dose response of the PTW 60019 microDiamond in magnetic fields: Characterisation for the Australian MRI-linac”, Satellite symposium on Standards and procedures for dosimetry and QA in MRgRT, Utrecht, 30 June, 2018. Oral Presentation.

Contents

Chapter 1

Introduction

1.1 Motivations

Radiotherapy aims to deliver ionizing radiation to the tumour while minimising the radiation dose to healthy tissues. Currently margins are added to target structures to account for treatment uncertainties, however this can result in nearby organs at risk (OARs) and surrounding normal tissue volumes receiving additional radiation dose. The treatment is further complicated when tumour motion is present, such as respiratory-induced motion during lung cancer treatments, which introduces additional uncertainties [1]. The position and shape of the tumour and surrounding OARs may also vary over the course of the treatment session. In this instance additional margins are typically placed around the target to account for motion which increases the chance of normal tissue toxicity [2]. Several techniques have been proposed to correct for motion, each of which may reduce the likelihood of normal tissue complications, however there is always an increased risk of missing part of the tumour. For improved accuracy of these treatments the dose calculation method should take into account motion, particularly when evaluating different motion management strategies and associated risks. This is particularly important for therapies such as Stereotactic Body Radiotherapy (SBRT), which utilises steep dose gradients with high doses delivered over fewer fractions compared to conventional radiotherapy and is therefore considered more complex. Firstly, this thesis evaluates current SBRT treatments for lung tumours using a novel four-dimensional (4D) Monte Carlo dose calculation tool, developed and implemented for this purpose.

An emerging technology which presents one solution to motion uncertainties are MRI-linacs. These systems offer high soft-tissue contrast imaging while simultaneously treating with a therapeutic radiation beam. MRI-linacs have the potential to adapt the treatment beam in response to changes in tumour position and shape; implementation of these systems should lead to reduction of tumour margins with subsequent reduction in normal tissue toxicity to surrounding organs [3]. However, the combination of a magnetic resonance imaging (MRI) scanner and a linear accelerator is non trivial due to the magnetic coupling between the two systems which compromises each systems performance. The presence of the magnetic field affects the trajectories of electrons via the Lorentz force and thus the dose deposited from contaminant and secondary electrons differs. These variations are more pronounced at air-tissue interfaces [4] which poses challenges for treatments of lung cancer sites. These differences in dose deposition in lung are also dependent on the radiation beam orientation with respect to the magnetic field, i.e. inline or perpendicular. Since MRI-guided lung SBRT could reduce treatment margins or provide individualised dose escalation it's potential should be further investigated. The second focus of this thesis is to set up a platform to perform such assessments for MRI-linacs, specifically for the Australian program.

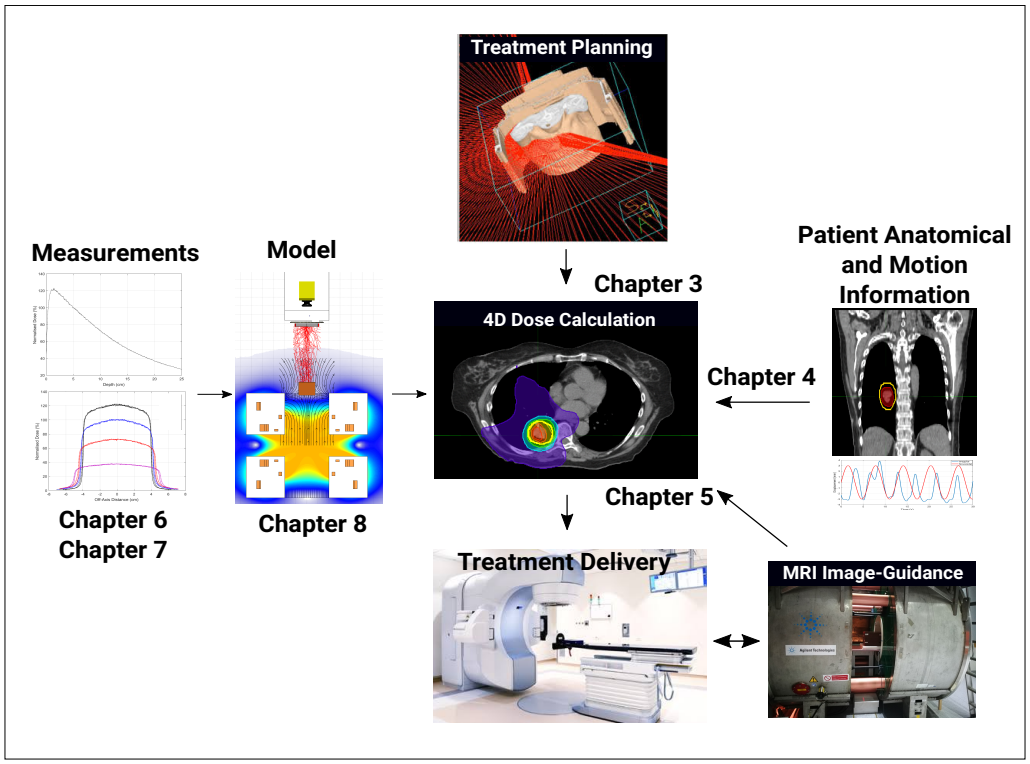

Figure 1.1: Diagram showing the processes of the (4D) radiotherapy treatment chain of interest in this thesis, each chapter is shown next to the process it addresses.

Overall, this thesis aims to improve our understanding of current treatment techniques and inline MRI-guided radiotherapy for lung SBRT of moving targets. This will be achieved through the development of 4D modelling and dosimetry methods. Figure 1.1 shows a diagram of the processes of the (4D) radiotherapy treatment chain, each chapter is shown next to the process it addresses.

1.2 Aims and Objectives

The aims of this thesis are:

Aim 1: To incorporate temporal information (4D) into an in-house Monte Carlo dose calculation system in order to take into account respiratory motion and the dynamic delivery of radiation.

Research Questions: Does modelling the complexities of motion and dynamic radiation delivery with a Monte Carlo dose engine improve agreement between measured and calculated dose?

This is addressed in Chapter 3.

Aim 2: To assess motion and radiation beam delivery uncertainties for lung volumetric arc therapy (VMAT) stereotactic body radiotherapy (SBRT) for current treatments and on inline MRI-linacs.
Research Questions: What is the impact of motion and delivery uncertainties on dosimetric endpoints? Does the impact vary for different motion management treatment techniques? Does the impact vary for different respiratory motion amplitudes and tumour geometries? Does an inline magnetic field improve or diminish the sensitivity of delivery uncertainties for lung treatments?
This is addressed in Chapters 3, 4 and 5.

Aim 3: To assess different methods of acquiring dosimetric data on an inline MRI-linac; the data should be suitable for beam modelling.
Research Questions: Which dosimeters are useful for acquiring specific measurements in MRI-guided radiotherapy (MRIgRT) environments? Do the effects of the magnetic field on dose depositions further challenge the choice of detector for beam data measurements? How can measurement limitations for these systems be addressed?
This is addressed in Chapters 6 and 7.

Aim 4: To model the Australian MRI-linac radiation beam in a convolution-based treatment planning system and with Monte Carlo.
Research Questions: Can we accurately model the beams behaviour using a convolution-based treatment planning system? Will the Australian MRI-linac system require Monte Carlo for dose verification?
This is addressed in Chapter 8.

Chapter 2

Literature Review

This chapter provides a brief overview of the stages or processes involved in radiation therapy. This is then followed by a review of the different strategies used for imaging and treating moving lung targets. The last section includes a summary of MRI-linac systems with focus on dosimetry and the associated challenges.

2.1 External Beam Radiation Therapy

External Beam Radiation Therapy (EBRT) involves delivering high doses of ionising radiation to the tumour by a linear accelerator (linac) while sparing the surrounding healthy tissues. Typically the machine rotates around the patient and the radiation beam is shaped by a multi-leaf collimator (MLC) to achieve the prescribed tumour dose and satisfy normal tissue dose constraints [5]. Each stage of the treatment process, to be described below, is important for ensuring the safe delivery of EBRT.

2.1.1 Imaging

In the first stage the patient is imaged in the intended treatment position. A three-dimensional (3D) image is acquired which accurately represents the patients anatomy and the tumour. It is important that the image has high spatial resolution and that contrast between different tissues is adequate. The main imaging modality used for EBRT is Computed Tomography (CT); however combining CT with other imaging modalities such as Magnetic Resonance Imaging (MRI) or Positron Emission Tomography (PET) is becoming increasingly widespread. CT uses the attenuation of x-rays through the body to generate an image. In short, a CT gives information on

the electronic cross sections of tissues in the body however at the expense of exposing the patient to low doses of ionising radiation. The workings of an MRI machine are quite complex and will not be described in detail here, for more information readers are referred to textbooks [6, 7]. MRI uses strong magnetic fields and radio waves to manipulate protons (hydrogen nuclei) in the body, more specifically their nuclear spins are magnetised. The radiofrequency signals produced by tissues in response to these magnetic fields are measured (using the technique of nuclear magnetic resonance analysis [8]) and from this information a 3D image can be generated. MRI offers improved soft tissue contrast compared with CT, without additional imaging dose. For these reasons there is increasing interest in using MRI in radiation therapy for the delineation of tumours [9]. However there are drawbacks in using MRI as a stand-alone imaging modality such as a lack of electron density information, which is necessary for dose calculations, and image distortion resulting in geometrical uncertainties (discussed more in section 2.3.2).

2.1.2 Delineation and Treatment Planning

Once an image is obtained, the tumour and organs at risk (OARs) are identified by contouring or delineating the structures on the 3D image. ICRU reports [10–12] define several tumour volumes that need to be delineated for tumour tissue; gross tumour volume (GTV) contains the visible tumour, this volume is expanded to the clinical target volume (CTV) which includes microscopic malignant tissue. An additional margin is added to the CTV to form a planning target volume (PTV), this margin incorporates geometric uncertainties in treatment e.g. patient setup errors. Uncertainties in volume delineation in radiation oncology, particularly variations between observers (or “delineators”), is an active area of research [13]. Subsequent to delineation of structures, tumour dose is prescribed along with maximum dose levels to surrounding critical structures. With this information the treatment planning systems (TPSs) algorithm creates a plan so that all these objectives are met. An optimised plan for treatments such as Intensity Modulated Radiotherapy (IMRT) and Volumetric Arc Therapy (VMAT) include varying beam angles, field sizes and dose rates.

2.1.3 Dose Calculations

Dose prescriptions are generally based off previous patient outcomes for that cancer type. It is therefore important that dose calculations of treatment plans are accurate to further our understanding on the biological response of certain tissues to radiation therapy [14] and thus maximize the therapeutic ratio [15]. Accuracy is also important to ensure safe treatments since a 5% difference in dose could lead to a 10-20% change in tumour control probability (TCP) and 20-30% on normal tissue complication probabilities (NTCP) [16]. The dose calculation algorithm used should not only be highly accurate but also computationally fast in order to maintain an efficient clinical workflow. The development of dose calculation algorithms has been ongoing since the late 1940s [17], and have seen a vast improvement due to advancements in computer-processing speed, medical equipment (e.g. dosimeters, CT scanners) and our knowledge of radiation physics. Some different types of dose calculation algorithms are discussed below.

Correction based algorithms require measurements of a range of photon beams in a water phantom which are then corrected to take into account factors such as beam modifiers (e.g. wedges) and patient composition (e.g. shape and inhomogeneities). Some patient inhomogeneity corrections include the equivalent path length method, power-law correction (Batho), equivalent tissue-air ratio and differential scatter-air ratio methods. The details of these corrections will not be discussed in this thesis however comprehensive overviews can be found in [18, 19].

Convolution algorithms (widely used in clinical TPSs) require a model of the beam fluence from the linear accelerator head, TERMA (total energy released per unit mass) and dose kernels to calculate dose deposited inside the patient [20]. Some examples include pencil beam convolution (PB), anisotropic analytical algorithm (AAA) and collapsed-cone convolution (CC). These algorithms can be further subdivided into those that do not consider changes in lateral transport of electrons (PB) and those that approximate the changes (CC, AAA) [21]. Collapsed-Cone Convolution [22] reduces computation time by collapsing all point-spread kernels from a cone along the central axis. Adaptive Convolution (AC) is a variation of this algorithm and is used for TPS calculations in this thesis. It reduces the calculation time even further by initially

assessing TERMA gradients; in regions where there is a low gradient, a coarse dose grid resolution is used and in regions of high TERMA gradients, a finer resolution is used [23]. Heterogeneities in both AC and CC algorithms are accounted for by density scaling of the energy deposition kernels. More detailed information on these algorithms can be found in the following [14, 24, 25].

The most accurate dose calculation methods solve the linear Boltzmann transport equations (LBTE). Monte Carlo indirectly solves these equations using stochastic methods. This method is considered to be the gold standard for dose calculations however is computationally intensive as it simulates the trajectories of individual particles [16]. Historically it was used to calculate the dose kernels used in other TPS algorithms [26]. The different Monte Carlo dose engines which are used in this thesis will be discussed in more detail in section 2.3.4. Another method is to explicitly solve these equations which is a relatively recent approach, a topical review of which can be found in [27]. Acuros® XB is an example of a commercial dose calculation algorithm classified as a LBTE solver.

2.1.4 Treatment Delivery

The delivery of radiation therapy involves setting the patient up on the treatment couch in the same position as treatment planning. Any variation of the patient position compared with planning (inter-fraction motion) may then be quantified and corrected prior to treatment delivery using on-board imaging systems such as kilovoltage (kV) cone beam computed tomography (CBCT) [28] or megavoltage (MV) portal imaging [29]. After the patient is correctly set up the treatment plan is delivered. For treatment sites which undergo motion during treatment delivery (intra-fraction motion), i.e. thoracic tumours, real-time imaging guidance may be necessary. Such methods are discussed further in section 2.2.5.

2.1.5 Lung SBRT

Stereotactic Body Radiotherapy (SBRT) is defined as delivering high radiation doses in fewer fractions (typically less than 10) so to disrupt tumour cell proliferation [30]. It is a promising treatment for early stage inoperable non-small cell-lung cancer [31] with

numerous clinical trials reporting improved local tumour control rates [32–34]. However increasing the dose per fraction results in an increased likelihood of radiation pneumonitis or pulmonary complications should lung tissue be irradiated [35]. Timmerman et al reported patients with grade 3 (12.7%) and 4 (3.6%) toxicities [34] following a phase 2 lung SBRT clinical trial. The treatment can be further complicated by target and lung motion and dose calculation accuracy (section 2.2.3). To safely deliver these treatments, every stage from imaging through to delivery should be highly accurate. In particular, to minimise toxicities, the dose gradient around the target should drop off rapidly and any motion of the tumour needs to be accounted for in planning, dose calculations and delivery.

2.1.6 Commissioning of a Linear Accelerator

Prior to being able to treat patients, commissioning of a treatment machine for clinical use must be performed. This is a process by which detailed measurements are taken to characterise the beam. It involves data acquisition (performed in water-equivalent phantoms), modelling the beam (in the TPS) and verification (compare measurements to TPS for more complex scenarios) [36]. This process is important for ensuring the safe delivery of radiotherapy; the procedures will be outlined here since this is a focus of chapters 7 and 8 (in the context of MRI-linacs).

AAPM Task Group 106 [37] reports on the equipment (phantoms and detectors) and procedures for collecting accurate beam data for linear accelerator commissioning. Data required for photon beams includes percentage depth doses (PDD) and profiles at various depths for all field sizes and wedge fields, MLC data (e.g. inter- and intraleaf leakage, penumbra, tongue and groove effects), scatter factors (collimator and total) and tray and wedge factors. The detector used for each measurements should be chosen carefully; it depends upon the resolution required and its suitability to the application and field size. Ion chambers (of size 4-6 mm in diameter) are commonly used for scanning water tank measurements however for small fields, the dose gradient is high and the comparatively large active volume of the detector leads to incorrect readings. For these field sizes detectors with small active volumes (e.g. stereotactic field diode) should be used [37].

2.1.7 Routine Quality Assurance and Treatment Tolerances

An integral part of each stage of the radiotherapy process is quality assurance (QA). QA in radiotherapy ensures accurate treatments by checking dosimetric and geometric accuracy. The equipment used for both imaging and treatment is routinely checked to verify that the output is within tolerance limits. These limits are set by a department and are typically based off recommendations in the literature. For complex treatment plans in which machine delivery parameters (e.g. gantry, MLC) are continuously varying such as VMAT, pre-treatment QA is essential to confirm the robustness of the plan to delivery.

Tolerances and action levels are in place for treatment machines to ensure safe deliveries; if a parameter falls out of the specified tolerance the treatment is halted. Recommendations for tolerances are given in AAPM Task Group 142 [38] and are specific to the machine type and the treatment techniques it delivers. A thorough understanding of the uncertainties associated with a treatment and the consequences is crucial in determining the tolerance levels for particular treatment parameters.

Delivery Uncertainties

Various studies have investigated the consequence of machine parameter errors on plan quality [39–45]. Mu et al. [40] demonstrated on average changes of 4% in $D_{0.1cc}$ of the spinal cord and brain stem for simple plans when introducing a 1 mm systematic error and a 12% difference for complex plans for head and neck patients. Blake et al. [45] investigated delivery uncertainties for lung SBRT and found an average difference of 4.5% for $D_{0.1cc}$ (Spinal Cord) for a 1 mm systematic leaf gap error and a 9.2% change for V_{20Gy} (Lung - PTV). Generally, MLC systematic errors were shown to have the greatest impact on treatment plans, and OAR DVH metrics were more sensitive to MLC errors than target metrics. In this thesis the sensitivity of lung SBRT for moving targets to MLC uncertainties are explored.

2.2 Radiation Therapy for a Moving Target

During the treatment of lung tumours, respiration-induced motion further complicates the therapy [46]. The position and shape of the tumour and surrounding tissues will

vary over the treatment time. Several methods have been proposed to correct for motion which include motion-encompassing margins, gating, breath-hold, image-guidance and real-time tracking [2]. Generally, methods used to treat moving targets involve the inclusion of temporal information, otherwise referred to as the 4th dimension.

2.2.1 Imaging

Four-dimensional Computed Tomography (4DCT) sorts CT images into phases of the breathing cycle, thus reducing motion artefacts in the images. The respiratory cycle is monitored during imaging by placing devices on or around the patients thoracic region, some examples include bellows and infra-red sensors. During image reconstruction, binning of CTs can be either phase- (based on percentage of the breathing cycle) or amplitude-binned (based on amplitude of the breathing cycle). 4DCT images may then be post-processed; a 3D minimum (MinIP), average (AIP) and/or maximum intensity projection (MIP) image can be calculated from the 4DCT dataset and used for delineation of structures or planning the treatment.

Other methods of imaging a moving target include breath-hold CT (the patient holds their breath during image acquisition of a three-dimensional CT (3DCT)), gated CT (the patient is imaged at a distinct period of the breathing cycle), and slow scan CT (the CT is acquired very slowing in order to include multiple phases therefore a time-averaged image is obtained).

2.2.2 Delineation and Treatment Planning

A visual representation of different methods used in delineation and treatment planning of moving targets is shown in figure 2.1 as compared to conventional techniques. Conventional free-breathing does not take the breathing trace into account while imaging or planning, this method leads to artefacts in the image and consequentially delineation errors [47]. The internal target volume (ITV) approach defines a treatment margin which encompasses the whole range of motion ensuring tumour coverage at the expense of increased dose to the lung volume [10]. This method may define the ITV on the MIP image or taking the union of the GTVs defined on individual phase CTs. The mid-ventilation method on the other hand uses a CT which represents the tumour in

the time-weighted average position and therefore allows for reduced treatment margins compared to the ITV method under the circumstances that individual patient tumour motion is considered [48]. Target definition for a gated treatment plan involves the union of GTVs within a 30%-duty cycle around the phase chosen for gating (typically the end-exhalation or end-inhalation positions) [49]. For the case of treating using the breath-hold technique, the structures are defined on the 3DCT obtained while the patient holds their breath and additional margins are added to account for uncertainties in tumour location for this method.

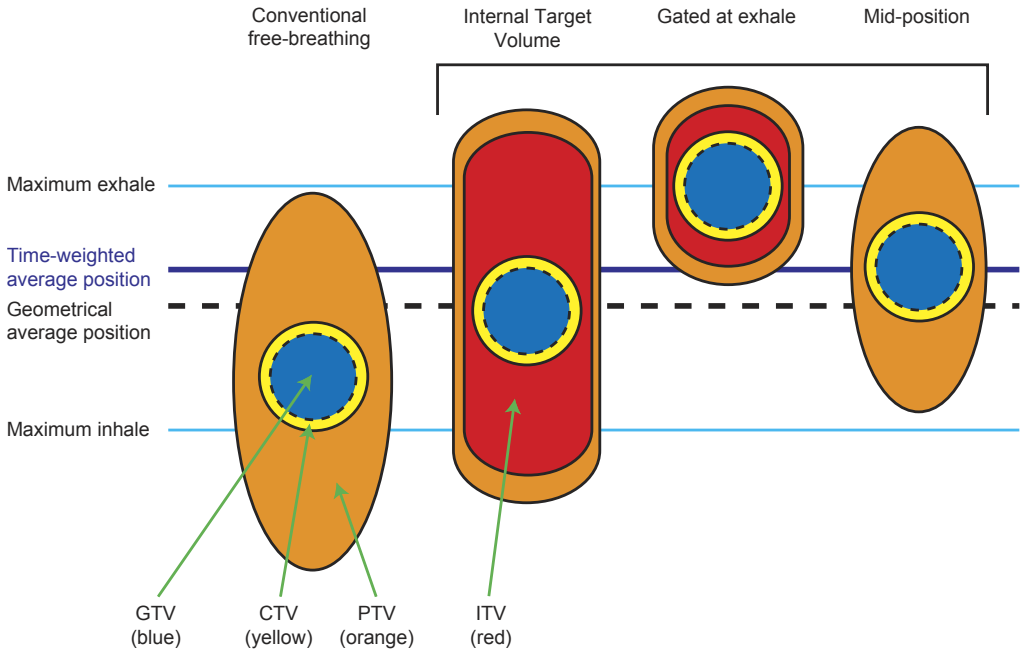

Figure 2.1: Different methods of delineation for treatment-planning of moving targets. Figure taken from Wolthaus et al. [50]. GTV = gross tumour volume; CTV = clinical target volume; PTV = planning target volume.

For lung treatment planning it is important to use an accurate dose algorithm for optimisation, as well as for the dose calculation, in order to obtain a high quality plan [51]. The image which is used for optimisation will also influence the resulting plan [52].

2.2.3 Dose Calculations in Lung

Dose calculations for lung cancer sites are the most challenging due to the low density of lung tissue surrounding the high density tumour which leads to lateral electronic disequilibrium conditions. The lateral range of secondary electrons in lung is large and

when the ranges are similar to the field size, charged particle equilibrium no longer exists. Many dose algorithms used in TPSs use approximations for lateral transport of electrons and therefore lack the accuracy required to calculate dose under electronic disequilibrium conditions. Numerous studies have shown differences between dose calculation algorithms for lung phantoms and patients [53–56], with Monte Carlo calculations being the most accurate [16].

For lung SBRT the accuracy of an algorithm needs to be investigated prior to clinical use owing to the small fields used in this treatment technique. Figure 2.2 is from a recent review on the accuracy of dose calculation algorithms for lung SBRT by Fogliata et al. [57]. Panettieri et al. [58] showed an underestimation by CC at the lung/GTV interface in a phantom geometry. Li et al. [59] and Hardcastle et al. [60] performed calculations with patient data; both results showed lower target and lung doses for CC compared to Monte Carlo.

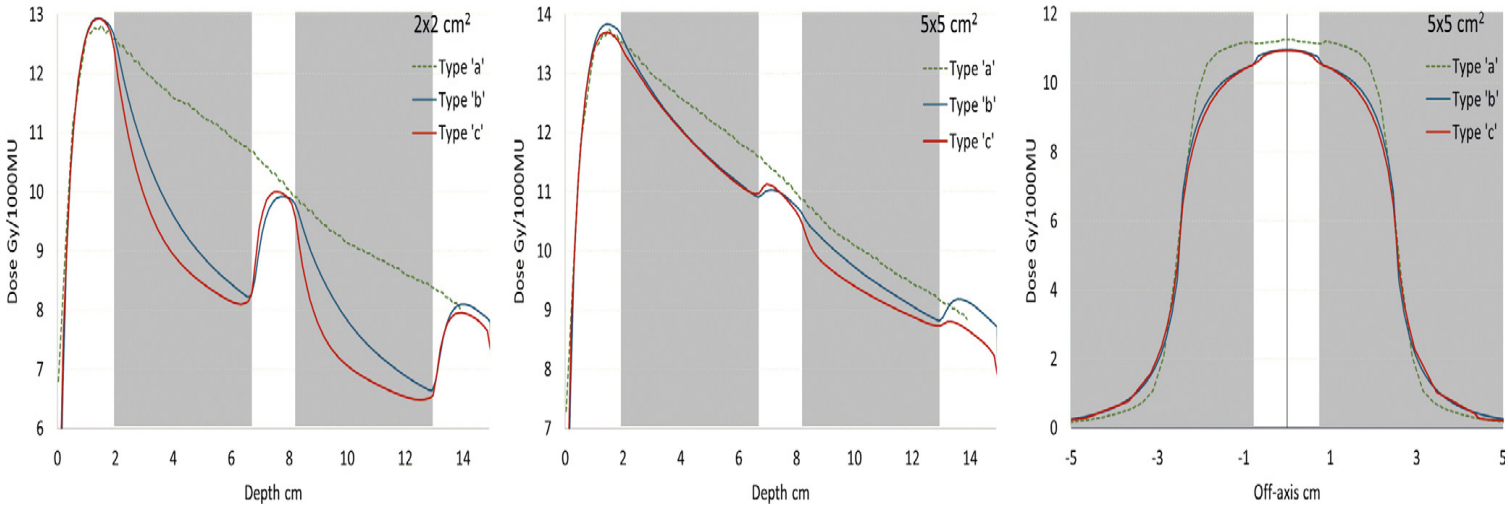

Figure 2.2: Comparison of dose calculation algorithms in a cubic lung phantom using SBRT field sizes. Figure taken from Fogliata et al. [57]. Grey shaded area is lung material. Type 'a' refers to algorithms which don't consider lateral transport of electrons (e.g. Pencil Beam). Type 'b' refers to algorithms which approximate lateral transport of electrons (e.g. Collapsed Cone Convolution). Type 'c' refers to principle based algorithms (e.g. Monte Carlo).

The physics of lung SBRT is further complicated by respiration-induced motion. The effects of motion on dose distributions include blurring (leads to reduction of PTV dose conformity), interplay effects (tumour moves out of the beam aperture which is shaped

by moving MLC) and deformation effects (the changing density of the tumour effects the probability of interactions of radiation) [61]. For improved accuracy the dose calculation stage should take into account motion, particularly when evaluating different strategies for treating a moving target.

2.2.4 4D Dose Calculations

Four dimensional dose calculations is a term that can imply any method which considers tumor motion information when calculating the dose distribution; typically these calculations use 4DCT images. These calculations have previously been performed by computing the dose from the whole plan on each phase and scaling by the number of phases [62–65] or by the time weight for each phase [66]. These methods have limited consideration of temporal components in their calculations and therefore cannot be used to assess effects of interplay between the beam delivery system and tumor motion. 4D dose calculations for post delivery verification have been proposed [67–70] whereby treatment log files from the machine and respiration monitoring device are used to simulate the control points delivered to each CT phase. Rao et al. [71] performed 4D calculations by splitting up the treatment plan among phases and calculating the dose in Pinnacle^3. Ehrbar et al. [72] presented a similar method where they assigned control points to the respiratory phases in Eclipse (Varian Medical Systems, CA, USA) assuming that each phase was equivalent to the duration of one control point and all patient cases had the same steady respiratory cycle.

Although commercial TPSs are improving their ability to incorporate 4D information into the dose calculation, they have limited ability to account for the interplay between temporal variables such as those that occur during a VMAT SBRT lung delivery. With higher temporal resolution, the accuracy of the dose calculation should improve; in this thesis the Monte Carlo dose engine is used for VMAT pre-treatment time-resolved 4D dose calculations by assigning parts of the dynamic plan to different 4DCT phases using temporal information.

2.2.5 Treatment Delivery

Some treatment techniques for moving tumours include the ITV approach, gating and breath-hold which have been discussed in sections 2.2.1 and 2.2.2. A step further in improving the treatment of moving tumours is to use image guidance and real-time tracking techniques [73–77]. Tracking techniques typically include the use of internal fiducials or external surface markers to track the location of the tumour, and the couch or MLC will shift position to ensure the treatment plan is mimicked. The image guidance systems currently used for tracking have low soft tissue contrast, deliver extra radiation dose to the patient and involve an invasive procedure when used in conjunction with internal fiducial markers. MRI on the other hand offers excellent soft tissue contrast while not delivering additional radiation dose.

2.2.6 Treatment Uncertainties

It is important to evaluate uncertainties for the motion-management techniques used in a radiotherapy department. The imaging modality used can lead to localisation uncertainties caused by artefacts resulting from variations in the breathing cycle during the acquisition, this is in addition to other limitations of the modality for example geometric distortions observed in MRI (see section 2.3.2). For tumour tracking techniques using external or internal markers as a surrogate, uncertainties in tumour position arise as well as latency between the systems. The time between registering the surrogates position and for the MLC or couch position correction needs to be evaluated. Both geometric and latency tolerances should be implemented in QA programs for these treatment techniques [78].

2.3 MRI-linacs

The concept of MRI-linacs is to adapt the radiation beam to deliver a more precise treatment by utilising knowledge of tumour position and shape obtained from the MRI in real time. This should allow for tighter dose margins with a subsequent reduction in dose to healthy tissue surrounding the target [79]. Currently there are four different MRI-linac designs in the world, two which are used clinically [80, 81] and two research systems [82, 83]. Each design has a unique variation of the radiation beam with respect to

the magnetic field, the magnetic field strength and the MRI bore design. The two possible beam to magnetic field orientations are perpendicular (transverse) and parallel (inline or longitudinal). The specific features of each system are summarised in table 2.1.

Table 2.1: The different features of the MRI-linac systems available

System	Linac	B_0 Orientation	B_0 Strength	Bore Design
ViewRay [80]	6 MV (replaced previous Co60 sources)	Perpendicular	0.35 T	Split
Elekta-Unity [81]	7 MV	Perpendicular	1.5 T	Closed
Cross Centre Institute, Canada [82]	6 MV	Perpendicular and Inline	0.5 T	Split
Ingham Institute, Australia [83]	6 MV	Perpendicular and Inline	1 T	Split

While there are many potential advantages to these systems, there are many engineering and dosimetric challenges to overcome.

2.3.1 Challenges of Integrating MRI and Linac Technology

Linac Induced Distortion and Interference on MR Imaging

Linacs can affect the operation of the MRI in three ways (1) magnetic materials in the linac cause inhomogeneities in the magnetic field, of most concern is the MLC [84], (2) RF noise produced from the magnetron interferes with the gradient coils [85] and (3) radiation causes eddy currents in the gradient coils [86]. All three reduce image quality and thus degrade the geometric accuracy of the system. Solutions to reduce these effects have been proposed; some examples include, RF decoupling by using a Faraday cage / RF shielding [87–90], increasing the distance between the two components [90, 91] and actively shimming the magnet [90].

Magnetic Field Effects on Linac Components and Dose Deposition

The magnetic field affects the trajectories of electrons via the Lorentz force resulting in changes in electron transport in the linac gun, waveguide and target as well as dose deposition in the patient. The influence of the magnetic field on the electron gun (e.g. output loss) has been well studied [91–93] as have alternate electron gun designs to resolve the issue [91, 94, 95] or magnetic shielding of the electron gun [96] or linac [97, 98]. Any form of shielding distorts the MRI scanners magnetic field and in turn affects imaging. Compromises must therefore be made between the design of the two systems.

The changes to the dose deposited in the patient for MRI-linacs can be divided into the characteristics observed in the perpendicular and inline orientations. In the perpendicular systems, the curved trajectory of electrons results in asymmetric point spread kernels with less depth penetration [99, 100], thus laterally shifted profiles and shallower build-ups are observed [101]. Increased dose occurs at material interfaces with high variation in density due to electrons curving back around in the low density material, termed the electron return effect (ERE) [4] (see figure 2.3), which is also dependent on the orientation of the interface [102]. For moving lung tumours this poses challenges as changes in tumour shape or orientation will effect the dose deposited, increasing uncertainty in dosimetry. Also observed on these systems are differences in entrance skin dose in [103] and out [104] of the primary beam due to these deflections. The magnitude of the aforementioned effects are strongly dependent on the field strength [99].

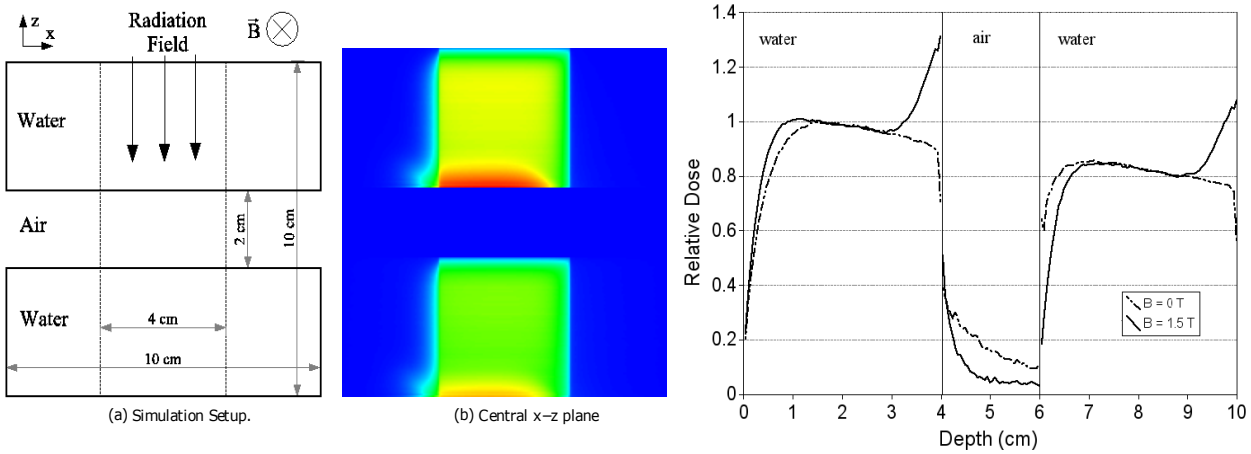

Figure 2.3: The electron return effect that occurs for perpendicular MRI-linac systems. Electrons curve back round in a low density material and results in increased dose at the surface of the high density material. Figures taken from Raaijmakers et al. [4].

For the case of inline systems the changes in dose distributions are minimised; with the field in the same direction as the beam ERE is mitigated. Instead increases in dose along the central axis are observed as the electrons are forward-directed. A reduction in lateral scattering of the electrons subject to an inline magnetic field results in penumbral trimming [105]. However, this orientation can lead to higher dose to the patient surface due to the magnet's fringe field [90, 103, 105–108]. Contaminant electrons produced in the linac head and air volume between the patient and linac would typically diverge with only some reaching the patient. The fringe field of the MRI focuses these electrons along the central axis resulting in high electron contamination at the surface. This effect can be lessened with the inclusion of a yoke to reduce the size of the fringe field [103, 108, 109]. The intensity and size of the high electron surface contamination is not only dependent upon the magnetic field's footprint but also the strength of the magnet (B_0), the radiation field size and the proximity of the linac components to the MRI. Measurements on the first prototype of the Australian MRI-linac system (a 1.5 T ex-clinical MRI) showed an approximate 300% increase in near surface dose for a 3 $\times$ 3 cm^2 field with a source-to-MRI-isocenter distance of 2.87 m [90]. Characterisation of these magnetically focussed contaminant electrons on the Australian MRI-linac system is the subject of chapter 6.

2.3.2 Lung SBRT for MRI-linacs

MRI-guidance could deliver lung SBRT with higher accuracy and precision [110] due to its potential to continuously track the tumour, resulting in a reduction of motion margins thus minimising dose to lung tissue. However there are challenges which need to be addressed with both radiation delivery and imaging.

Radiation

For perpendicular systems the ERE can be problematic at air-tissue interfaces [79] although it can be compensated for by using opposing beams [102, 111]. Bol et al [112] investigated ERE compensation for moving air cavities and concluded that IMRT plans optimised at 0 T can be used as the ERE is not prominent when the air cavities are fully covered by cross beams. An exception to this is for situations where air cavities appear and disappear during treatments in which case plans should be gated or re-optimised.

On the other hand, for inline magnetic fields the electrons are forward-directed. This means the dose kernels are elongated, and in lung substantial changes to penumbral widths are observed [113] as well as potential dose enhancement effects for lung tumours [114, 115] which has been demonstrated experimentally [116]. Oborn et al. [115] showed this enhancement was dependent on the tumours location, density and size. It is important that the dosimetry of dynamic lung tumours is well understood for progression towards inline MRI-linac lung SBRT patient treatments.

Other than the variations in dose distributions there are also uncertainties with dose calculations using MRI images as they do not provide information about electron density and attenuation coefficients. Dose calculations can only be performed by generation of synthetic or pseudo CTs [117] or registering the MR image to a planning CT [118], both methods which contribute uncertainties to the treatment process. The former is difficult in the thoracic region since the MR signal in lung is low (due to its low proton density) and therefore assigning densities to regions becomes problematic [110].

Imaging

The quality of MR images depends on the homogeneity of the main magnetic field as well as linearity in gradient fields [119], with the latter being the main contributor to systematic geometric distortions. To reduce these distortions the main magnetic field can be shimmed and algorithms are applied to correct for non-linearities in the gradients [120]. In addition to scanner specific distortions, the object or patient that is being imaged induces distortions. In terms of imaging in lung, magnetic susceptibility at lung-air interfaces contributes to significant artefacts in the image [121]. Due to the large differences in the magnetisation properties of air and lung, static local field gradients are formed at these interfaces which opposes the main magnetic field. The resulting distortions introduce artefacts.

Another challenge in MR imaging for lung are motion artefacts [122]. One solution, which is similar to 4DCT, is to monitor the patient's respiratory signal with pneumatic bellows and synchronise image acquisition with the breathing cycle [121]. Alternatively a navigator signal from MRI can be used to monitor motion. Imaging techniques used to overcome motion artefacts can be split into multi-slice 2D [123, 124] and 3D acquisitions [125, 126]. 4D-MRI refers to respiration-correlated, it is not time resolved as the speed of acquisitions is currently not fast-enough, a comprehensive review on 4D-MRI for radiotherapy is given by Stemkens et al [127].

2.3.3 Dosimetry for MRI-linacs

In addition to the physical changes in dose deposition, the dose response of detectors can also be influenced by the magnetic field. The density of the detector becomes important as to how it will affect the dose reading, also to note is the orientation of the detector in the magnetic field [128–130] and the presence of air gaps surrounding the detector [131]. Therefore, the choice of detector and its setup for specific dosimetry measurements should be considered even more carefully (than conventional radiotherapy) for these systems.

Ionisation chambers are the most widely used type of dosimeter for radiation measurements [132], particularly for reference dosimetry. However in magnetic

fields, the trajectories of secondary electrons in air (being low density) are significantly altered and therefore the response of ion chambers are affected. Many groups have explored ion chamber correction factors in these conditions [128, 129, 133–137] showing a strong dependence on chamber shape and orientation with respect to the magnetic field and beam. Other groups have investigated the dose response of point diodes [130] and diamond detectors [130, 138] in fields of both orientations and varying strengths.

Smit et al. [134] presented a prototype MRI compatible scanning water tank and evaluated CC01, CC04 and CC13 ion chambers for relative dosimetry. They found that it was possible to use these ion chambers with the prototype water tank for scanning measurements which is important for beam commissioning. O'Brien et al. [139] examined changes in the relative response for shielded and unshielded diodes, diamond and three different sized ionization chambers. This study concluded that the diodes and diamond were underestimating the lateral shift in profiles characteristic of perpendicular MRI-linacs. The diamond, however, was shown to be suitable for commissioning and output measurements provided that a correction was applied for this underestimation. The microDiamond (PTW, Feriburg, Germany) was characterised in a 1.5 T MRI-linac by Woodings et al. [140]. It was found that the effective point of measurement was in agreement with the vendor specification and depth dose and profiles agreed with CC04 ion chamber measurements. Additionally, depth dose measurements performed by Wegener et al. [141] for a range of different magnetic field strengths showed closest agreement between microDiamond and radiochromic film. These studies were all performed on systems with the magnetic field perpendicular to the radiation beam, the microDiamond's relative response in an inline system was not observed.

2D dosimetry is important for machine and patient QA therefore 2D detector devices should be tested in magnetic fields to validate their use for MRI-linacs. The IC PROFILER^{TM} (Sun Nuclear Corporation, Melbourne, FL) was characterised in a 1.5 T perpendicular MRI-linac system [142] and shown to be suitable for measuring profiles. Perik et al. [143] investigated the STARCHECK$^{MAXI\ MR}$ (PTW, Feriburg, Germany) in a perpendicular system and found it was suitable however should only be used when stationary. 2D silicon diode array detectors have been characterised in magnetic field

environments (both inline and perpendicular) [144, 145]. EPIDs have also been studied for MRI-linac dosimetric applications [146, 147] and shown feasibility as long as certain corrections are in place e.g. gantry angle dependence.

Radiochromic Film Dosimetry

Radiochromic films are used extensively for 2D dosimetry in radiotherapy clinics. The chemical principle of these films is polymerisation, which occurs when ionizing radiation interacts in the film emulsion (pentacosa-10,12-diyonic acid (monomers) immersed in a gelatin matrix) polymers are formed resulting in colourisation. The degree of colour formation is dependent on dose delivered however this is not a linear response and varies between film batches. Gafchromic® EBT film (Ashland, Covington, USA) is often used for megavoltage beams as it has minimal energy dependence, a high tissue equivalence for clinically relevant energies [148] and a high spatial resolution making it desirable for SBRT dosimetry [149]. These characteristics also make it a promising candidate for MRI-linac dosimetry. There is however concern that the polymerisation process would be effected by the magnetic field [150–153]. Reynoso et al. [150] found significant differences (up to 15%) in absolute dose for EBT2 film and, using scanning electron microscope imaging, visualised changes in the crystal structures orientation in the film. Barten et al. [152] studied film in a low magnetic field (0.35 T) whereas Billas et al. [153] investigated magnetic fields up to 2 T, both concluded that the changes caused by the magnetic field were small and that EBT3 is suitable for relative and absolute dosimetry.

2.3.4 Treatment Planning and Dose Calculations for MRI-linacs

The theory of algorithms used for treatment planning and dose calculations is quite involved, some details were included in sections 2.1.2, 2.1.3 and 2.2.3. This section is included to give a brief overview of the algorithms used for each MRI-linac system.

The ViewRay system uses a fast Monte Carlo based algorithm and a convex-nonlinear inverse optimisation algorithm for the TPS [154, 155] with the option to account for the magnetic field in secondary electron transport calculations. During the development of the Elekta-Unity system the optimisation procedure that was proposed used Geant4 to calculate beamlet dose kernels and optimise the beamlet weightsgeometrical using the

ORBIT algorithm [111]. The current commercial TPS for the Elekta-Unity (Monaco) uses GPUMCD, which is a fast GPU-oriented dose calculation platform [156] to calculate anatomy specific beamlets. Beamlets for each gantry angle are calculated if they intersect the target using a ray casting algorithm, and for beamlet weighting the optimisation algorithm FIDO is used [157]. The Alberta group have proposed using LBTE solvers for dose calculations instead of Monte Carlo, this is allows for the inclusion of electromagnetic fields in the first order LBTE [158–162].

The effects of the inline magnetic field on optimisation for lung plans were shown by Schrenk et al. [163] to reduce mean dose to lung however had no detrimental effects on PTV coverage. Current commercial TPSs are not capable of modelling the complete magnetic field, including the fringe field. Begg et al. [164] have shown that beyond the electron contamination region of the Australian MRI-linac, the relative dose deposition in water along the central axis remained unchanged with different inline magnetic fields strengths. Although there are small changes to penumbral widths in water [113], these changes could be modelled in the TPS. Therefore, it is expected that current commercial TPS systems will be able to model an inline MRI-linac if the magnetically focussed electron contaminants are somehow removed. Differences in lung tissue will be more significant than water [113]. To ensure that deviations caused by the magnetic field are minimal the Australian MRI-linac program has proposed a Monte Carlo dose verification system to calculate patient dose distributions with and without the magnetic field. A focus of this thesis is to test the feasibility of using a convolution-based TPS, Pinnacle^3 (Philips Healthcare, Fitchburg, USA), to model the radiation beam. A Monte Carlo model is also developed alongside the TPS model for the aforementioned dose verification system.

The Monte Carlo dose engines used in this thesis are EGSnrc [165] and Geant4 [166], the details of each are discussed below.

EGSnrc

EGSnrc is written in MORTRAN (macro from FORTRAN), it is split into BEAMnrc (which models the linear accelerator head) and DOSXYZnrc (which models the patient). A phasespace is used when running simulations between the two codes (i.e. BEAMnrc

and DOSXYZnrc). This is a file which stores information about particles crossing a defined plane, it will include the particle type, energy, momentum vector, and position. In recent years EGSnrc have implemented charged particle transport in magnetic fields [167] and as such studies have used the code to model dosimetry effects in MRI-linac systems [109, 136, 168, 169].

Geant4

The Geant4 toolkit is written in C++ programming language; it was originally intended for high energy physics however is now commonly used for medical physics applications. The user defines physics processes, geometry and tracking parameters allowing for customisation. The main classes used are Detector Construction (for defining geometries), Physics List (for defining physics processes) and Primary Generator Action (for defining the particles to generate including their properties). The user must also define an output for the simulation (may use additional class: Stepping Action), this could be the dose deposited in a geometry, or a phasespace of the particles crossing a specified plane. Geant4 has been previously been used to model radiation in the presence of magnetic fields [99, 100, 107, 115, 116, 128, 144, 170, 171] and proven to be accurate for this purpose.

Chapter 3

A 4D Monte Carlo Dose Calculation Tool for the Treatment of Dynamic Lung Tumours: a Phantom Study

Some of the results presented in this chapter have been published in the journal Physics in Medicine and Biology:

N. F. Roberts, M. Williams, L. Holloway, P. Metcalfe, B. M. Oborn, "NOTE: 4D Monte Carlo dose calculations for pre-treatment quality assurance of VMAT SBRT: a phantom-based feasibility study", Phys. Med. Biol. 64 (21), 21NT01 (10pp).

3.1 Overview

SBRT utilises steep dose gradients with high doses delivered over fewer fractions compared to conventional radiotherapy [172], and is a promising treatment for inoperable non-small cell-lung cancer [31]. VMAT can be used in SBRT to deliver highly conformal dose distributions with faster treatments times [173], however it involves gantry rotation, dynamic MLC motion and variable dose rates which increases the complexity of the treatment. Typically for lung cancer sites, respiration-induced motion can further complicate the therapy [46]. Several methods have been proposed to correct for respiration-induced motion which include motion-encompassing margins, gating and breath-hold techniques [2]. The ITV approach defines a treatment margin which encompasses the whole range of motion ensuring tumour coverage at the expense of higher lung dose. The use of image guidance and real-time tracking techniques is

also of interest [73–77]. Dynamic treatment-couch tracking is a method whereby the tumour motion is corrected for by moving the couch in the opposite direction. This method has not yet been used clinically however there are promising research systems available [174–176]. For improved accuracy of these treatments the dose calculation method should take into account motion, particularly when evaluating different motion management strategies and associated risks.

Dose calculations for lung SBRT are complicated by electronic disequilibrium conditions which exist in low density media (lung) and for small fields used in SBRT. The accuracy of algorithms available in commercial TPSs should always be evaluated prior to clinical use for these types of treatments [57]. Monte Carlo dose calculations are considered the gold-standard [16] and will inherently provide the most accurate dose calculation for small fields in lung tissue. The Monte Carlo dose engine is used in this chapter to inform on any deficiencies with the TPS algorithm, Adaptive Convolution. Commercial treatment planning systems (TPSs) are also limited in their ability to account for the interplay between temporal variables such as those that occur during lung VMAT SBRT delivery.

An in-house Monte Carlo system developed at the Illawarra Cancer Care Centre (Wollongong, Australia) for calculating radiotherapy dose distributions has been previously benchmarked [177]; it offers a flexible framework for incorporating 4D information into the dose calculation. This chapter reports on the development and implementation of a 4D Monte Carlo (4DMC) calculation method for use as pre-treatment quality assurance of lung VMAT SBRT plans. The 4DMC method was compared with 3D Monte Carlo (3DMC) and a 3D and 4D TPS approach. Experimental measurements were performed with radiochromic film in a dynamic thorax phantom. Additionally, the method was used to explore uncertainties in motion and delivery of lung VMAT SBRT with the phantom.

3.2 Materials and Methods

3.2.1 Phantom Imaging

A 4D CT dataset of a CIRS Dynamic Thorax Phantom Model 008A (CIRS Inc., Norfolk, VA, USA) was acquired. For this study the 3 cm diameter target insert was used and simple 1D sinusoidal motion in the superior-inferior direction was set with an amplitude of $\pm$15 mm and cycle time of 5 seconds. This direction of motion was chosen as it is the most prominent for thoracic tumours [178] and $\pm$15 mm amplitude was used to evaluate an extreme case. The 4D image dataset was acquired using a SIEMENS Sensation Open CT scanner with a spatial resolution of $0.98 \times 0.98 \times 2$ mm^3. The real-time position management (RPM) block (Varian, Medical Systems, CA, USA) was placed on the breathing platform to obtain a respiratory signal, the images were then sorted using phase-based binning into 8 phases and imported into the treatment planning system (TPS).

3.2.2 Treatment Planning

Two types of plans were generated in Pinnacle^3 V14. The first plan uses an ITV approach, where the treatment margin encompasses the whole range of motion. The ITV was contoured on the MIP dataset and transferred to the AIP dataset for optimisation; this will be referred to as the ITV-plan. An additional 5 mm isotropic margin was added to define the PTV. The second plan was to mimic dynamic treatment-couch tracking, a method whereby the tumour motion is corrected for by moving the couch in the opposite direction. The second plan was optimised on a single phase of the 4DCT dataset (the reference phase); this plan will be denoted as the TRACKING-plan. For this particular scenario the couch only needs to correct in 1D however for 3D tumour motion with deformation, planning with the intention of couch tracking would be more complicated. For the TRACKING-plan the GTV was contoured on the reference dataset and PTV was set to equal the GTV with an isotropic margin of 5 mm. Lung was defined on all datasets as the lung region minus the GTV (as defined on the reference phase). The dose prescription to the PTV was 60 Gy to be delivered over 3 fractions with a dose objective of $D_{95\%} \geq 60$ Gy and dose constraint of $V_{20} \leq 20\%$ to the lungs. Both plans were optimised using 6 MV (Varian 2100C) dual-arc VMAT techniques with a control point

Table 3.1: Summary of datasets used for planning, contour definition (including physical volume), 3D and 4D dose calculations (DC). AIP = Average Intensity Projection, MIP = Maximum Intensity Projection, RefP = Reference Phase, 4DCT = all phases of the 4DCT dataset.

Plan	Optimisation	ITV/GTV (volume, cm^3)	PTV (volume, cm^3)	3D DC	4D DC
ITV-	AIP	MIP (30.56)	AIP (68.11)	AIP	4DCT
TRACKING-	RefP	RefP (12.02)	RefP (32.63)	RefP	4DCT

gantry spacing of 4° (180 control points in total). The total number of MU for each plan was 7074 and 6824 for the ITV- and TRACKING-plan respectively. A summary of the datasets used for treatment planning, treatment volume definition and dose calculations is included in table 3.1.

3.2.3 3D Dose Calculations

3D Monte Carlo

A previously benchmarked, in-house EGSnrc based system developed at the ICCC [177] was used for the Monte Carlo simulations. The system uses BEAMnrc to model 6 MV beam production from a Varian 2100C linac. The particles are then stored in an IAEA phase space file which is read in by DOSXYZnrc to simulate transport through the patient or phantom. All DOSXYZnrc simulations had a photon cutoff energy of 0.01 MeV (PCUT) and electron cutoff energy of 0.521 MeV (ECUT) with dose grid resolution of $1.95 \times 1.95 \times 2$ mm^3. The number of primary histories was 4 x 10^{10} (electrons hitting the target) and at the phase space plane in the DOSXYZnrc simulations the particles were recycled 29 times giving an uncertainty in dose scored of $\pm 1.5\%$ of the maximum dose. An advantage of this system is that it is fully automated; a plan is exported from the TPS to a dedicated cluster and the simulations are built based off the RTPlan, CT and RTStruct DICOM files. After the simulations are complete the system then analyses the dose files produced and generates a report which compares the dose from the TPS (RTDose) and the Monte Carlo simulations.

3D Adaptive Convolution

Treatment planning system dose was calculated with a dose grid resolution of $2 \times 2 \times 2$ mm^3. 3D adaptive convolution (3DAC) dose calculations were performed on the respective datasets that the plans were optimised on and the DICOM files were exported for analysis. 3DMC dose calculations were performed on these corresponding datasets for comparison.

3.2.4 4D Dose Calculations

4D Monte Carlo

To perform 4DMC dose calculations, the RTPlan file for each of the plans mentioned in section 3.2.2 was modified using MATLAB® R2017a (Mathworks Inc., Natick, MA, USA) so that each phase was allocated part of the plan. This was achieved by determining the duration of each control point and then distributing the control point to the phases based off the respiration cycle, as shown in figure 3.1. A simulation was performed for each of the 8 phases, calculating the dose deposited in the phantom with input of the modified DICOM RTPlan files. For the TRACKING-plan the isocentre was shifted to match the centroid of the tumour on each phase, this is equivalent to the couch shifting position by this amount, and so emulates a tracking delivery. The time taken to run sub-plans for all phases was 2-3 hours performed on a dedicated cluster of 200 CPU cores.

4D Adaptive Convolution

4D adaptive convolution (4DAC) calculations were carried out by importing the modified DICOM RTPlan files into Pinnacle^3, calculating the dose for each phase and then exporting RTDose for analysis.

Dose Accumulation

The 4D target dose was calculated by firstly accumulating the dose from all 8 phases by aligning tumour centroids of each dose distribution to the reference phase centroid, see figure 3.1(d). A rigid registration is valid for this scenario since the tumour is not deforming in shape and motion is in the superior-inferior direction, therefore not changing with respect to edges of the lung.

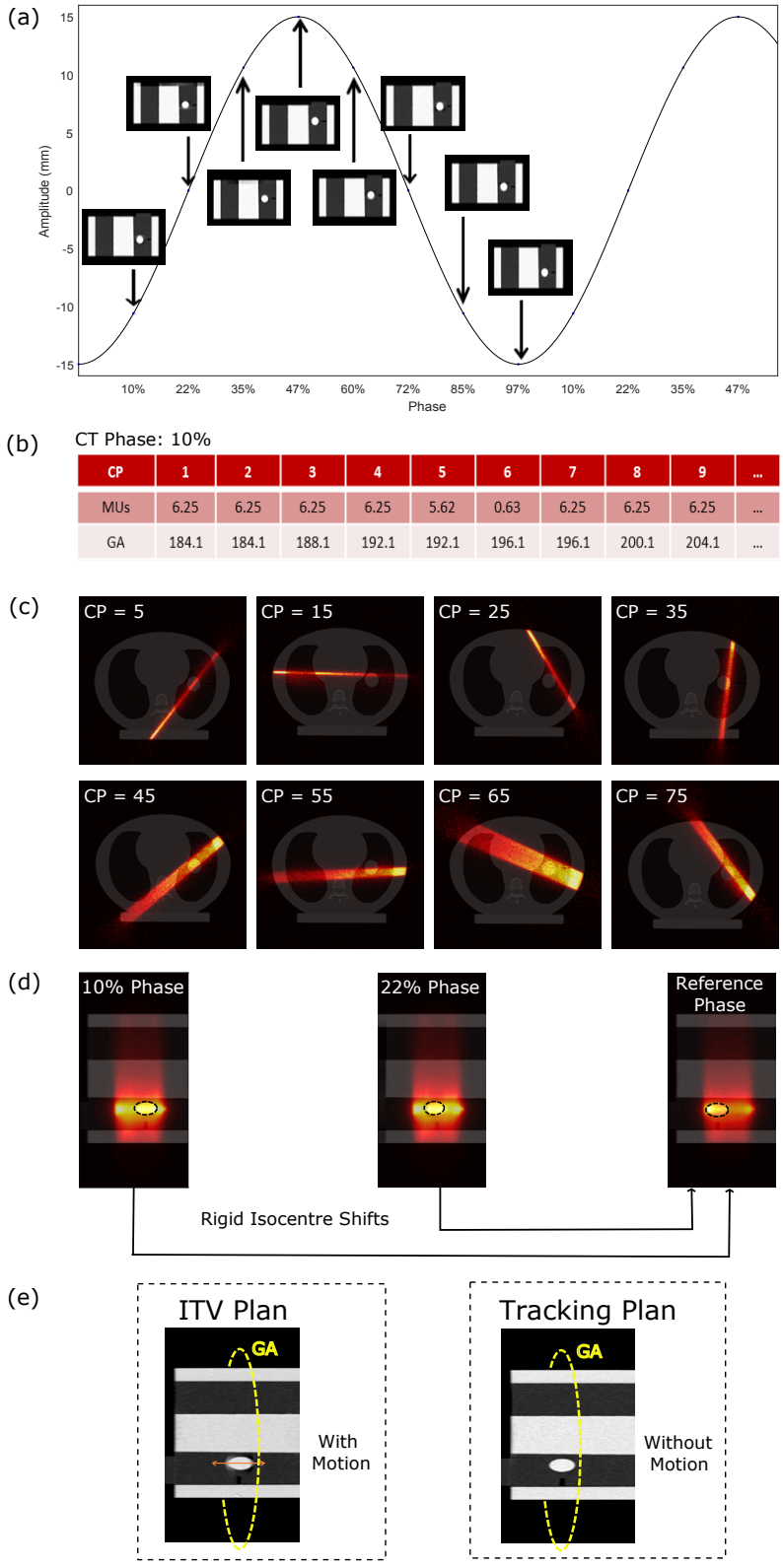

Figure 3.1: A breakdown of the 4D dose calculation method and measurements: (a) The breathing cycle; divided into the 8 phases, showing corresponding CTs (coronal slice through target). The plan is distributed among the phases using the time of each phase and the time of the control point to appropriately assign the MUs. (b) The first few modified CPs assigned to phase 10% are shown in the table. (c) Dose distribution from select control points for a single phase's sub-plan. (d) Total dose from select phases, these are accumulated to the reference phase by rigid tumour centroid shifts. (e) Display of how measurements were performed for both plan types. GA = Gantry Angle, CP = Control Point.

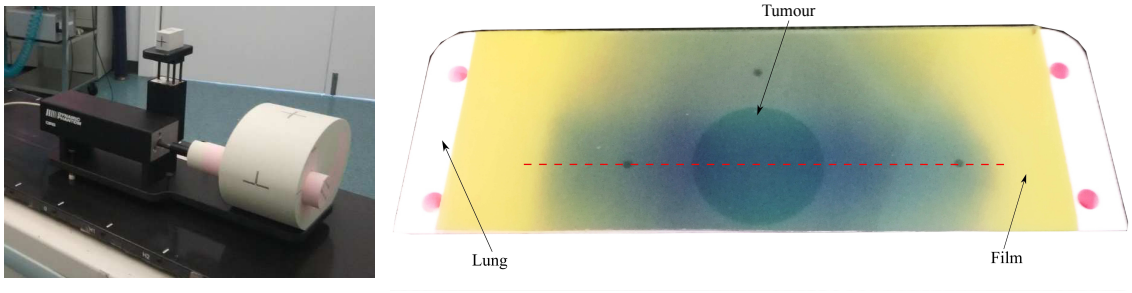

Figure 3.2: CIRS Dynamic Thorax Phantom (left) and SBRT insert (right) with Gafchromic® EBT3 film (after ITV-plan was delivered) overlaid. The 3 cm diameter tumour is visible behind the film. Dashed line represents direction of profile taken for results shown in figure 3.3. The dashed line is along the direction of motion.

3.2.5 DVH Metric Analysis

MATLAB® was used for all analysis. The DVH metrics that were calculated included $D_{98\%}$ (GTV), $D_{95\%}$ (PTV) and D_{mean} (Lung). For calculations on the 4DCT dataset, DVH metrics were evaluated using the contours defined on the reference phase. GTV DVH metrics for all methods were calculated using the GTV as defined on the reference phase of the 4DCT. PTV DVH metrics were evaluated using the PTV as defined on the dose calculation dataset e.g. on the AIP dataset the PTV was an expansion of the ITV. Mean dose to the lung was calculated by summing the mean dose from each phases simulation.

3.2.6 Treatment Delivery

Simulations were verified with Gafchromic® EBT3 film inside the CIRS SBRT insert (figure 3.2). This is identical to the imaging insert, however contains a slot for film placement through the middle of the tumour. Measurements were performed with film from the same batch, calibrated on the 6 MV linac used for all measurements. The film was scanned on an EPSON 10000XL flatbed scanner as 48-bit tiff format at 72 dpi using transmission mode with colour corrections turned off. All analysis was performed using the red channel and uncertainty was determined by evaluating a 95% confidence limit across 3 scans.

The ITV-plan was delivered to the moving phantom. A manual synchronisation of the beginning of the treatment beam with the starting phase (used in simulations) was performed. The TRACKING-plan was delivered to a stationary tumour to match

simulations and mimic a perfect tracking delivery i.e. assuming no uncertainties in the couch or tumour motion in this instance. Performing the delivery this way separates the effect of 'dose-smearing' between control points which is not accounted for in the simulations. The film's isocenter was aligned with the isocenter of the calculated dose distributions and global gamma analysis using criteria of 3%/3 mm and 5%/3 mm was performed to compare dose profiles.

3.2.7 Motion Uncertainties

Interplay between tumour motion and MLC motion can result in dose deviations and is particularly important to study in hypo-fractionated dose regimens (SBRT). To investigate uncertainties due to the interplay effect, sets of 4DMC simulations were run with a different starting phase. The starting phases investigated were at the extreme positions, begin- and end- exhalation and the mid position, mid-ventilation. This effect was only investigated for the ITV-plan since for the TRACKING-plan it is assumed that the tumour and MLC are inline for treatment and therefore the interplay effect is not of concern. It is recognised that treatment-couch lag for the TRACKING-plan is a source of uncertainty however this was beyond the scope of this thesis.

3.2.8 Delivery Uncertainties

To explore delivery uncertainties, systematic errors in the MLC leaf positions were introduced into the plans using MATLAB® and the dose for the error plan was recalculated with 4DMC. The leaf errors included shifts in both banks in the same direction by ± 0.5, ± 1 and ± 2 mm, defined at isocentre plane. The other simulated error type was a shift which resulted in the field size of the beam closing or opening, i.e. both banks are shifted inwards or outwards by a total magnitude of 0.5, 1 and 2 mm. Errors plans were compared to the 4DMC baseline plan by evaluating the relative difference between DVH metrics described in section 3.2.5. A difference of $\pm 5\%$ in $D_{95\%}$ (PTV) and mean dose to the lungs was considered significant [179].

A subset of error plans were also delivered to investigate the sensitivity of EBT3 in detecting small MLC errors. All open field size error plans that were deemed unacceptable with 4DMC, including the error plan below the threshold, were delivered.

The measured dose from the error plan was compared to the baseline measured plan by performing gamma analysis. The acceptance criteria of >95% points passing for 3%/3 mm global and >85% of pixels passing 2%/2 mm global was applied [180].

3.3 Results and Discussion

3.3.1 Comparison of Different Dose Calculation Methods

The accuracy of 3D dose calculations for dynamic tumours can be limited for particular motion-management techniques. When evaluating dose for plans that use the ITV-approach, differences between calculated and delivered dose can occur due to motion blurring effects, the interplay effect and differences in density [61]. This work showed deviations in 3D and 4D calculations when evaluating DVH metrics for the ITV-plan. Table 3.2 summarises the DVH metrics calculated from all dose calculation methods. 4DMC was used as the ground truth for the following comparisons and relative differences are quoted.

Table 3.2: DVH metrics calculated for the ITV- and TRACKING-plan, comparing dose calculation methods both 3D- and 4D- with AC and MC.

	ITV-Plan				TRACKING-Plan			
	3DAC	3DMC	4DAC	4DMC	3DAC	3DMC	4DAC	4DMC
$D_{98\%}$ GTV (Gy)	71.9	70.9	70.0	69.5	65.4	64.5	65.6	64.1
$D_{95\%}$ PTV (Gy)	61.6	62.0	61.6	62.0	61.2	62.4	61.0	61.1
D_{mean} Lung (Gy)	9.8	10.1	10.0	10.4	7.9	8.2	7.9	8.1

For the ITV-plan, the 3DAC showed the highest $D_{98\%}$ (GTV) overestimating by 3.5% while 3DMC showed a 2% overestimation. D_{mean} (Lung) was underestimated for both 3D- and 4D- AC methods compared to the MC methods. Whereas comparing 3DMC to 4DMC there was small variation in D_{mean} (Lung). The TRACKING-plan showed smaller deviations than the ITV-plan between calculation methods. $D_{98\%}$ (GTV) calculated with the 3DAC method overestimated by 2.0% and with 4DAC by 2.3%. For this plan D_{mean} (Lung) was lower for both AC methods as opposed to calculated with MC, however the deviations are not as significant. $D_{95\%}$ (PTV) for both plan types showed negligible

differences between calculation methods except 3DMC for the TRACKING-plan overestimated by 2.1%. This difference is likely due to variation in density between each phase's CT at the tumour periphery caused by imaging motion artefacts.

The simulation times of this 4DMC reasonable for clinical implementation. It is noted that the times will vary for patient datasets depending on the size of the dataset and the size of the tumour volume as this will determine the size of the beam apertures and hence the number of particle histories that need to be tracked in the simulation. An advantage of the 4DMC method over using the TPS approach for 4D calculations is that it is automated, whereas the TPS approach required manual export, modification and re-import of the plan parameters and then dose calculation on each phase.

3.3.2 Comparison of Dose Calculations to Measured Dose

Figure 3.3 shows dose profiles from each calculation method and measured data for each plan type. For the ITV-plan, the film and 4DMC dose profiles showed good agreement with a 3%/3mm global pass rate of 95.8%, whereas the agreement of the 3DAC with film was much poorer, and had a pass rate of only 50%. 3DMC also showed poor agreement to film with a pass rate of only 48.6% while for 4DAC the pass rate was 75%. Applying a less strict gamma criteria of 5%/3mm yields pass rates of 58.3%, 55.6%, 87.5% and 98.6% for 3DAC, 3DMC, 4DAC and 4DMC respectively. Differences between film and 4DMC profiles for the ITV-plan can be partially attributed to 'dose-smearing' that occurs between control points in the delivery, which the static control point approximations used in the 4D calculations do not take into account. In the simulations the motion of the phantom was modelled by 8 static CTs whereas in measurements motion was continuous, this 'motion-smearing' would also contribute to small differences. A large source of deviation would be due to measurement set-up error.

3D dose calculations, for both algorithms, for the ITV-plan varies from measurements beyond 15 mm from the isocentre. This variation is due to the higher density on the AIP dataset between 15-30 mm whereas for the measurements this region is classed as lung. Within the region of the dotted lines i.e. the GTV on the reference phase CT, the 4D dose was slightly higher than the 3D dose due to the higher density of the GTV on the

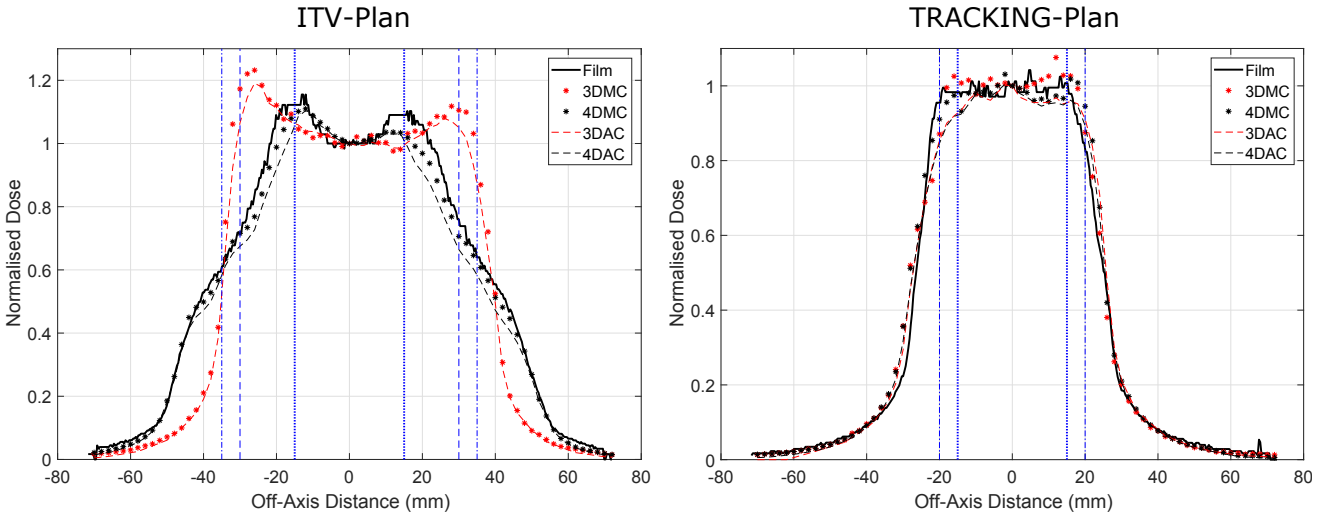

Figure 3.3: Comparison of measured, 3DAC, 3DMC, 4DAC and 4DMC dose profiles through the tumour isocenter for the ITV-plan (left) and the TRACKING-plan (right). Contours are displayed as horizontal lines on the graph. GTV $(\cdots)$ as defined on the reference phase, ITV $(- - -)$ as defined on the AIP CT dataset shown on the left graph and PTV $(\cdot\ -\cdot -)$ as defined on the AIP CT (left graph) and as defined on the reference phase (right graph). See figure 3.2, the dotted line indicates the location of given profiles. The isocentre dose is approximately 20 Gy. Estimated uncertainty in film measurements was $\pm 3\%$ and for 4DMC was $\pm 1.5\%$ of the maximum dose.

phase binned CTs compared to the AIP CT (see table 3.3). The expected tumour density is 1.06 g/cm^3 [181].

The TRACKING-plan showed better overall agreement for both 3D and 4D calculations with the largest disagreement between measured and calculated doses in the penumbral region and the PTV margin. For this set-up the tumour was stationary hence motion-smearing was not an issue. However dose-smearing between control points would be a contributing factor to the differences as this is not accounted for in the calculations. The gamma pass rate with 3%/3mm global analysis were 97.2% for 4DMC compared with measured and 94.4% for 3DMC. 3DAC and 4DAC compared with film both gave a 95.8% pass rate, for this plan the different dose calculation methods using AC made negligible difference to the profiles through isocentre. For a gamma criteria of 5%/3mm the pass rates were 100% for all dose calculations except 3DMC which was 95.8%.

Overall the estimated uncertainty was $\pm 3\%$ and $\pm 1.5\%$ of the maximum dose for the film

Table 3.3: GTV average density for each phase on the AIP CT dataset and the CT dataset corresponding to that phase, error calculated was 1 SD.

	GTV Mean Density (g/cm^3) $\pm$ SD	
Phase (%)	AIP CT	Phase binned CT
10	0.63 $\pm$ 0.12	1.03 $\pm$ 0.04
22	0.69 $\pm$ 0.11	1.03 $\pm$ 0.04
35	0.62 $\pm$ 0.12	1.04 $\pm$ 0.04
47	0.55 $\pm$ 0.14	1.04 $\pm$ 0.04
60	0.63 $\pm$ 0.13	1.03 $\pm$ 0.04
72	0.69 $\pm$ 0.12	1.03 $\pm$ 0.04
85	0.61 $\pm$ 0.13	1.04 $\pm$ 0.04
97	0.55 $\pm$ 0.14	1.04 $\pm$ 0.04

measurements and Monte Carlo calculations respectively. Taking into consideration all the aforementioned sources of error and these combined uncertainties, the high gamma pass rates between measurements and 4DMC dose demonstrate the improved accuracy of the 4DMC method compared to the considered 3D- and 4D- TPS methods.

3.3.3 Algorithm Accuracy

Comparing 3DMC and 3DAC dose profiles the most noticeable differences are at the periphery of the ITV for the ITV-plan and the periphery of the GTV for the TRACKING-plan. The differences between 4DMC and 4DAC occur around the high dose gradient regions in the profiles for both plan types. A general trend in DVH metrics was seen, the AC calculated a higher dose for $D_{98\%}$ (GTV) and lower dose D_{mean} (Lung). The collapsed cone convolution (CC) algorithm has been compared with MC for lung SBRT in previous studies. Panettieri et al. [58] showed an underestimation by CC at the lung/GTV interface in a phantom geometry, which agrees with the results presented here. Li et al. [59] and Hardcastle et al. [60] performed calculations with patient data; both results showed lower target and lung doses for CC compared to MC. The current work showed calculations using collapsed cone convolution (AC or CC) for lung SBRT fields should be used with caution.

3.3.4 Effect of Motion Uncertainties: Interplay Effect

Profiles through isocenter for each set of 4DMC simulations with a different starting phase for beam-on are shown in figure 3.4. Differences are observed in the PTV region (as defined on the phase-binned CTs) of the profiles. DVH metrics calculated for each starting phase set of simulations showed differences of less than 1% for $D_{98\%}$ (GTV), less than 0.5% for $D_{95\%}$ (PTV) and no difference for D_{mean} (Lung). This investigation of the interplay effect showed minor dose differences which is consistent with results found in other experimental phantom studies [182, 183]. These results support that the uncertainty in synchronising the starting phase with beam-on timing for the ITV-plan measurements would be negligible.

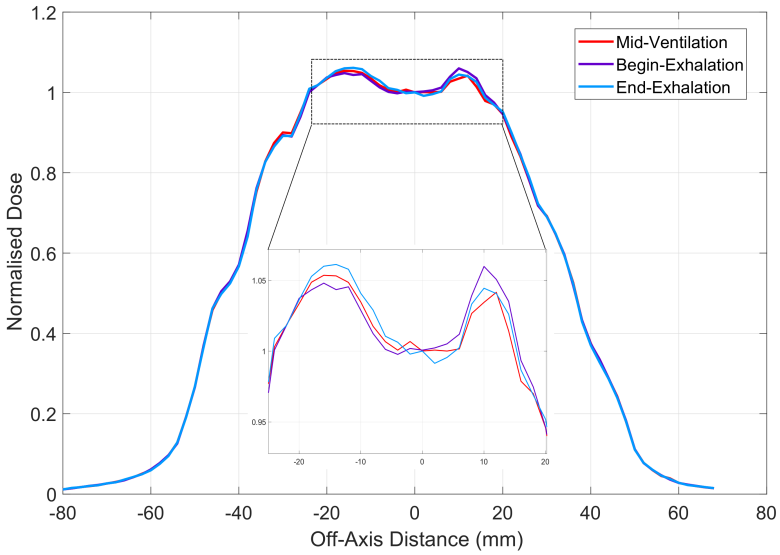

Figure 3.4: Profiles through isocenter (in direction of motion) for 4DMC dose calculations for the ITV-plan with different starting phases for beam-on. Starting phases include extreme positions, begin- and end- exhalation and the mid position, mid-ventilation. Inset of PTV region (as defined on the phase-binned CTs) showing differences between each starting phase set. Estimated uncertainty in 4DMC was $\pm$1.5% of the maximum dose.

3.3.5 Effect of Delivery Uncertainties: MLC Error Effects

The dose deviations of each simulated error plan from the baseline plan are shown for $D_{95\%}$ (PTV) in figure 3.5 for the the ITV-plan and figure 3.6 for the TRACKING-plan. For both plans dose deviations for D_{mean} (Lung) is shown in figure 3.7. Shifts in MLC in the same direction of up to 2 mm had no significant dose effects on either plan types. For the ITV-plan, MLC field size errors of 1 mm resulted in a dose difference of $\pm$ 5% or

greater for the lung mean dose. $D_{95\%}$ (PTV) for this error were just below the tolerance limits. While field size errors greater than 2 mm resulted in differences greater than 5% for the TRACKING-plan. The higher sensitivity of the ITV-plan to these systematic errors can be explained by the beam apertures being larger overall for this plan. In this instance the TRACKING-plan is more robust to MLC uncertainties however further investigation should be performed with patient datasets in order to make clinically relevant conclusions.

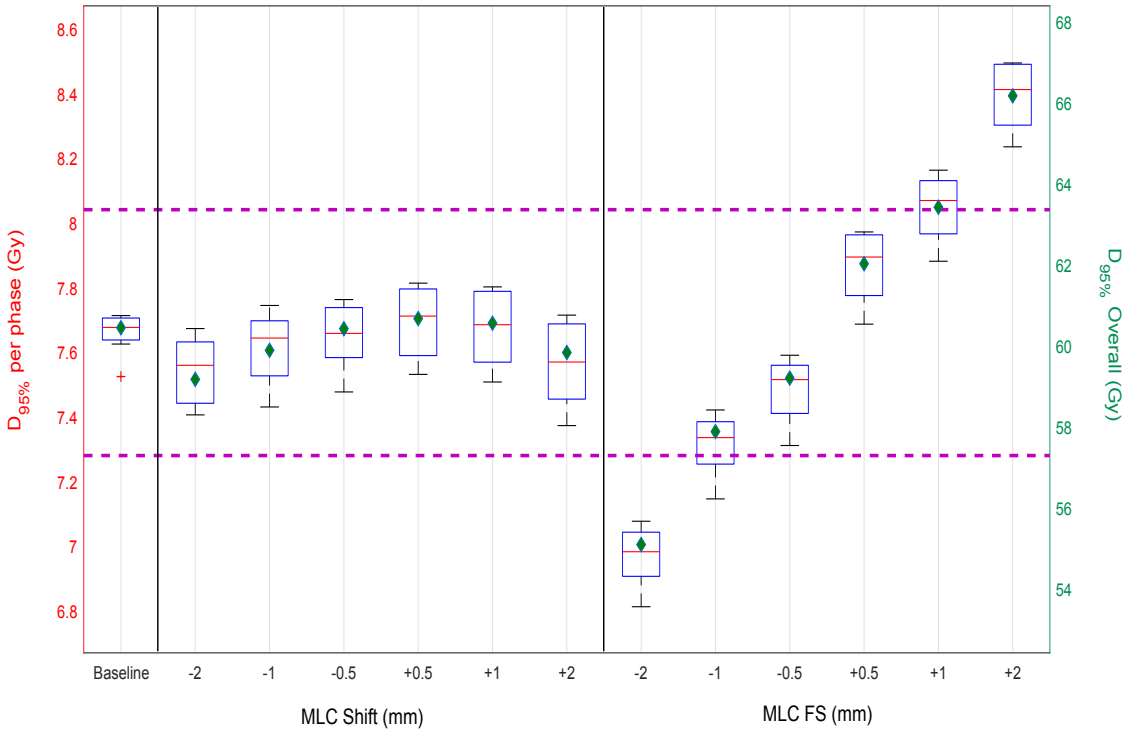

Figure 3.5: $D_{95\%}$ (PTV) for all MLC errors (shift and field size(FS)) for the ITV-plan. The left y-axis is $D_{95\%}$ per phase and is represented by the box plot, on the right y-axis is $D_{95\%}$ Overall and is represented by the green diamond markers. Dashed lines represent tolerance limits, $\pm 5\%$ dose deviation from baseline plans.

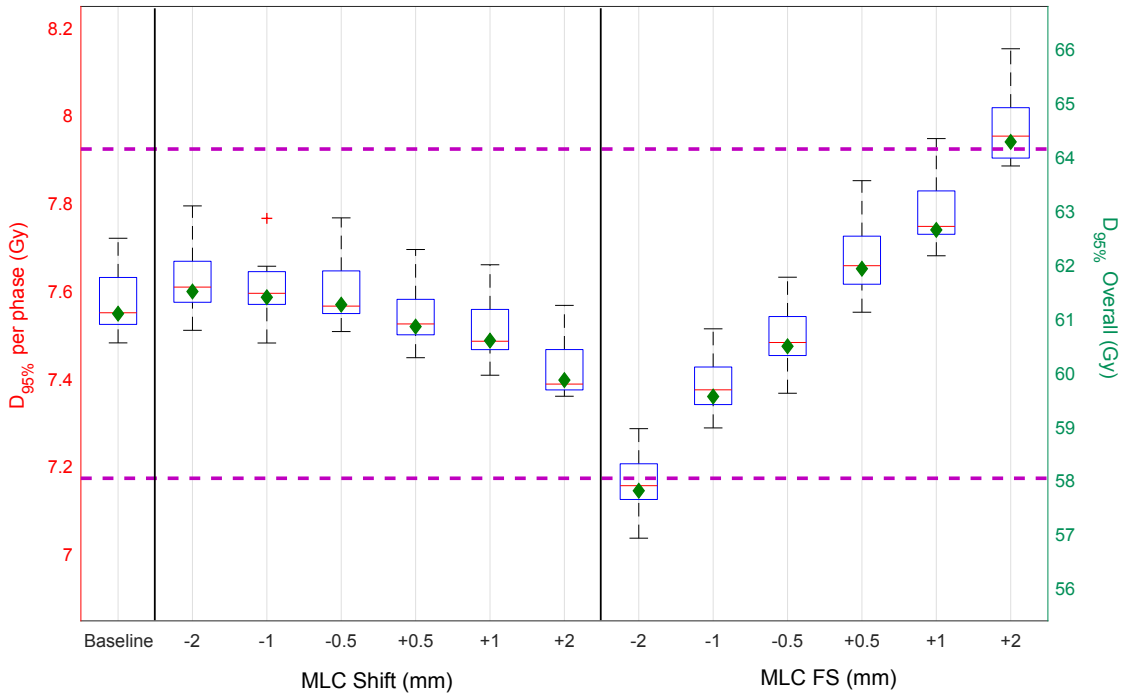

Figure 3.6: $D_{95\%}$ (PTV) for all MLC errors (shift and field size(FS)) for the TRACKING-plan. The left y-axis is $D_{95\%}$ per phase and is represented by the box plot, on the right y-axis is $D_{95\%}$ Overall and is represented by the green diamond markers. Dashed lines represent tolerance limits, $\pm 5\%$ dose deviation from baseline plans.

3.3.6 Effect of delivery uncertainties: MLC Error Detection

Measurements with gafchromic film of MLC open field size error plans were performed. The film dose between error and baseline plans were compared using gamma analysis. In the case of the ITV-plan, the plans failed gamma analysis for systematic open shifts of 1 mm and greater, these results are included in table 3.4. The film was capable of detecting the errors greater than 5% for this plan type using commonly applied gamma acceptance criteria. Isodose distributions for the ITV baseline and 2 mm error plan are displayed in figure 3.8; this shows expansion of isodose curves caused by the MLC systematic error as expected.

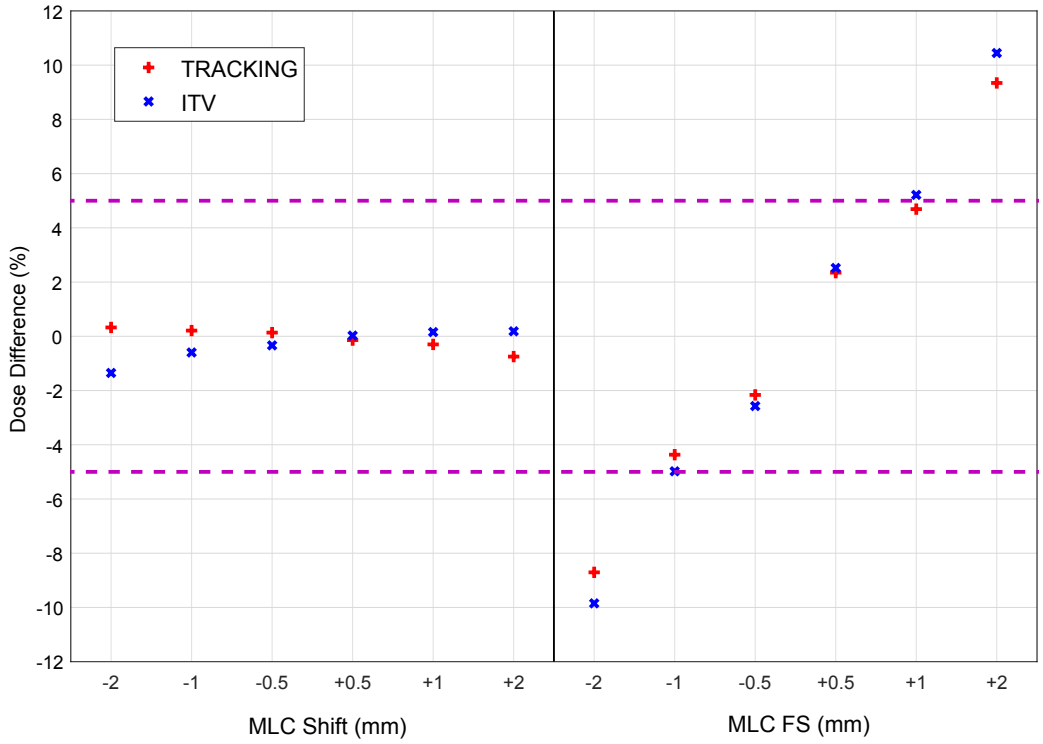

Figure 3.7: Dose difference of lung mean dose for all MLC errors (shift and field size(FS)) for both plan types. Dashed lines represent tolerance limits, ±5% dose deviation from baseline plans.

Table 3.4: Gamma passing rates for different criteria, comparing the film measured baseline ITV-plan to the film measured error plan. Only systematic open MLC field size errors were delivered. Criteria is displayed as % dose difference / distance to agreement, and specifies whether global or local analysis.

Error	3%/3 mm Global	3%/3 mm Local	2%/2 mm Global	2%/2 mm Local
0.5 mm	98.9%	98.3%	95.2%	92.4%
1 mm	91.3%	86.9%	66.8%	55.7%
2 mm	45.1%	36.9%	33.1%	19.6%

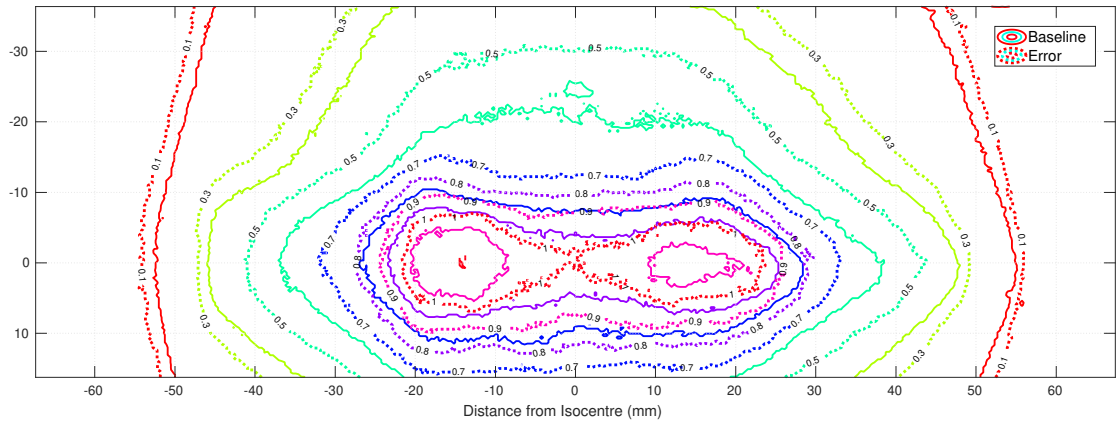

Figure 3.8: Film Isodose curves of the ITV-plan (baseline) represented by solid lines and 2 mm error plan represented by the dashed lines. This represents a coronal slice through the tumour isocentre. Dose normalised to the maximum dose of the baseline plan.

The gamma analysis results for the TRACKING-plan are shown in table 3.5, both 1 mm and 2 mm open systematic shifts failed. From the simulations the 1 mm error plan should be acceptable however the mean lung dose was just below 5% difference therefore it is possible that the 'dose-smearing' between control point during delivery, which is not accounted for in simulations, results in this plan failing in the delivery.

Table 3.5: Gamma passing rates for different criteria, comparing the film measured baseline TRACKING-plan to the specified film measured error plan. Only systematic open MLC field size errors were delivered. Criteria is displayed as % dose difference / distance to agreement, and specifies whether global or local analysis.

Error	3%/3 mm Global	3%/3 mm Local	2%/2 mm Global	2%/2 mm Local
1 mm	86.0%	83.8%	76.9%	70.8%
2 mm	69.5%	66.1%	64.5%	50.7%

3.3.7 Limitations of Study and Considerations

A limitation of the study is that only 1D sinusoidal motion and an extreme motion amplitude was considered. The dosimetric effects of motion will vary with tumour size and location as well as with motion amplitude, [184] the breathing curve and irregularities in motion [185]. A phantom is also not anatomically realistic and it is

expected that with more complex geometries the results could be more significant. The effects of uncertainties could too vary with these parameters for example a faster period could result in a more considerable result from the interplay effect.

The approximation of the treatment arc with 4° spacing is also a limitation of the 4DMC method, this method mimics the TPS, whereas in reality it is a continuous arc. The proposed method could be further improved by using a finer CP spacing resolution, which may reduce differences between measured and calculated. Although, for the TRACKING-plan, comparing the measurements and 4DMC calculations would indicate the effects of this approximation. Since the differences are small this would imply the approximation has minor effects on the result.

Another limitation of the 4D MC method is the use of 8 static CTs rather than continuously varying anatomy, this is addressed in the methods proposed by Gholampourkashi et al. [186]. Although such a method would improve the accuracy of the calculations the increase in time of the simulations should also be considered. Noting that the differences between the measured and calculated dose for the 4DMC method proposed here are small, the use of 4DCT phase data for the calculations may be acceptable.

The work in this chapter has omitted deformation in the first instance so as to eliminate uncertainties associated with deformable image registration. Chapter 4 includes translating this method to patient data therefore considers deformation.

3.4 Conclusion

In this chapter a 4DMC dose calculation method intended for pre-treatment lung VMAT SBRT quality assurance was developed and implemented. The method was compared with 3DMC as well as 3D- and 4D- convolution calculation methods. This work showed deviations in 3D and 4D calculations when evaluating DVH metrics for the ITV-plan. Differences in MC and AC calculations demonstrated collapsed cone convolution (AC or CC) for lung SBRT fields should be used with caution.

The 4D simulations were compared with experimental film measurements taken in a dynamic thorax phantom. Both plans showed better agreement with 4DMC compared to 3DAC. For the ITV-plan the 3DAC profile varied from film in the ITV periphery region due to the higher density on the AIP dataset whereas on the 4DCT datasets this region would be classed as lung. In the GTV region the 3DAC dose was lower than the 4DMC dose, this was due to the lower density for the AIP dataset in this region. The gamma pass rate for 4DMC was significantly better than the 3DAC dose comparing both with film measurements. The TRACKING-plan showed the largest disagreement between measured and calculated doses in the penumbral region however still displayed high gamma pass rates. The TRACKING-plan was superior for reducing dose to lung. Future work should consider a range of motion cases (amplitude, period and more dimensions) and different tumour sizes. Also of interest would be to study other motion management techniques using the phantom e.g. MLC-tracking or mid-ventilation, and to investigate how the 4DCT data affects the dosimetric results.

Uncertainties in motion and delivery were also investigated for these plans. For the ITV-plan the interplay effect showed minor dose differences whereas delivery errors were more significant; for MLC field size errors greater than 1 mm there was more than $\pm 5\%$ difference in DVH metrics. The TRACKING-plan exceeded these differences for 2 mm MLC field size error. The higher sensitivity of the ITV-plan to systematic MLC errors was due to the larger beam apertures present for this plan type. Errors which resulted in significant differences were delivered and detectable with EBT3 film; future work with clinical plans is required to further inform on suitable dosimeters for this purpose.

It is necessary to understand and quantify the limitations of 3D methods when calculating dose to a moving target, particularly in the case of lung where there are substantial variations in density. This work will be applied to clinical lung VMAT SBRT (in chapter 4) in an effort to better our understanding of quality assurance tolerances, for a range of respiratory motions and tumour volumes.

Chapter 4

Investigating Uncertainties for Lung SBRT using 4D Monte Carlo Dose Calculations: a Study with Patient Data

4.1 Overview

The higher doses per fraction in lung SBRT means the treatment is less forgiving of errors. It is therefore important to evaluate the effects of uncertainties associated with lung SBRT. A review by Schwarz et al. [187] on geometrical and dosimetrical uncertainties for lung SBRT describes studies which have investigated mean tumour position errors [188, 189] and the interplay effect [69, 71, 182–184]. Geometrical uncertainties in delivery parameters, such as MLCs, have been studied for lung SBRT [45] however no study has evaluated these uncertainties to a moving target. The 4D Monte Carlo dose calculation method which was proposed in chapter 3 can be used to evaluate errors in motion and delivery. This chapter presents 4D dose calculations for patient lung datasets, investigating the impact of the interplay effect (motion) and systematic MLC (delivery) uncertainties for different motion amplitudes and tumour geometries.

4.2 Materials and Methods

4.2.1 Patient Lung SBRT Plans

Ten 4DCT datasets (10 phases) from lung cancer patients previously treated with SBRT at Odense University Hospital, Denmark were used. The patient cohort had variation in

Table 4.1: Respiratory and tumour information for ten patients. The volume of the GTV and PTV as well as tumour location is listed. The location of the tumours are defined (by RTOG0915) as: near-rib, the GTV is within 1.5 cm of rib; central, the GTV is within 2 cm of bronchi; and free, the GTV is further than 1.5 cm from rib. The amplitude and period of the tumour motion is included.

Name	GTV / PTV (cm^3)	Tumour Location	Motion Amplitude (mm)	Period (s)
Patient 1	26.2 / 79.8	Central	13.4	2.6
Patient 2	4.3 / 27.0	Central	5.2	5.0
Patient 3	12.4 / 45.6	Central	0.6	2.7
Patient 4	1.0 / 10.8	Central	4.2	4.4
Patient 5	13.1 / 46.4	Free	18.8	3.0
Patient 6	7.6 / 33.4	Central	1.4	2.9
Patient 7	11.5 / 47.9	Free	7.0	3.0
Patient 8	4.2 / 28.4	Central	8.2	4.8
Patient 9	28.2 / 87.4	Central	0.2	2.7
Patient 10	1.4 / 12.7	Near-Rib	9.0	3.2

tumour size and motion characteristics. The mid-ventilation method had been used to define tumour contours for these patients, with PTV expansion of 5 mm in all directions except in the cranial-caudal which was 10 mm. VMAT SBRT plans were generated using Pinnacle^3 V16 for a 6 MV Varian TrueBeam. Plans consisted of two 200° arcs with 4° control point spacing. The location of the tumours are defined (by RTOG0915) as: near-rib, the GTV is within 1.5 cm of rib; central, the GTV is within 2 cm of bronchi; and free, the GTV is further than 1.5 cm from rib. The prescriptions were 48 Gy/4 fx (near-rib), 50 Gy/5 fx (central) and 54 Gy/3 fx (free). Note these datasets and corresponding plans have been used in previous studies [45, 190, 191]. Respiratory and tumour information for each patient is included in table 4.1. The motion amplitude was calculated using $\sqrt{CC^2 + AP^2 + LR^2}$ where CC is cranial-caudal motion, AP is anterior-posterior motion and LR is left-right motion.

4.2.2 Monte Carlo Simulations

4DMC simulations of the treatment plans were carried out as described in section 3.2.3 and 3.2.4. A simulation was performed for each of the 10 phases, calculating the dose deposited in the patient for each phase. The dose from each phase was then deformed and accumulated on the reference phase dataset (see section 4.2.3).

4.2.3 Deformable Image Registration

Dose accumulation was performed using the VoxAlign Deformation Engine which is an intensity-based, free-form deformable registration algorithm [192] in MIM-Maestro v6.8.5 (MIM Software Inc., Cleveland, OH). This algorithm has been used previously for dose accumulation in lung SBRT [193, 194]. Initially a rigid fusion between CTs (reference and secondary) was performed and used to assist in the deformable registration (for each of the phase CTs); the resulting deformation matrices are then used to deform and accumulate dose on to the reference phase (see figure 4.1).

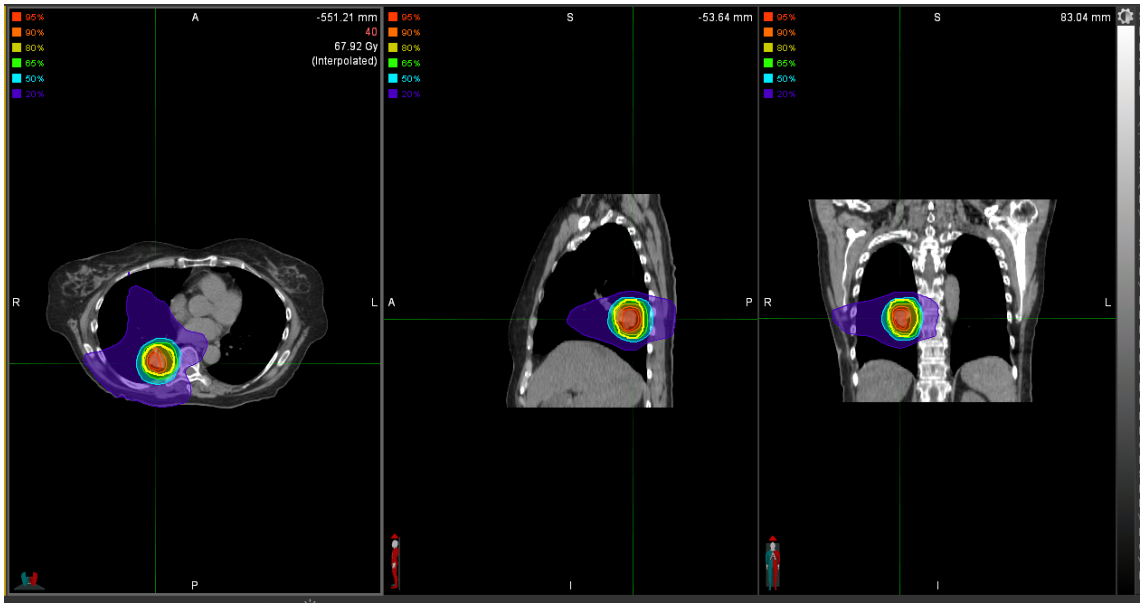

Figure 4.1: The reference phase CT for patient 5, accumulated dose overlaid with the PTV outlined in yellow.

4.2.4 DVH Metric Analysis

The accumulated RTDose DICOM was exported from MIM and analysed using MATLAB®. The DVH metrics evaluated for comparison were D_{mean} (PTV), $V_{95\%}$ (PTV), $V_{100\%}$ (PTV), D_{mean} (Spinal Cord), $D_{0.1cc}$ (Spinal Cord), D_{mean} (Lung - PTV)

and V_{20Gy} (Lung - PTV). Following the criteria set by the Blake et al. study [45], a relative difference of 2% in a DVH metric was considered significant.

4.2.5 Motion Uncertainties

Simulations were run with two different starting phases with beam-on, these were the extreme positions of the breathing cycle. DVH metrics were compared among the two different simulations to observe if the interplay effect resulted in significant deviations.

4.2.6 Delivery Uncertainties

Systematic leaf position errors that result in a change in field size were investigated here. The MLC field size shifts simulated were therefore of total magnitude 1 mm i.e. both banks shift inwards or outwards by 0.5 mm (therefore smaller than that investigated by Blake et al.). The relative dose difference of DVH metrics (section 4.2.4) between error plans and the baseline plan were calculated to quantify the impact of MLC uncertainties on plans.

4.3 Results and Discussion

4.3.1 Motion Uncertainties

Differences in DVH metrics as a result of varying the starting phase with beam-on are shown in figures 4.2 and 4.3 for the target and OAR metrics respectively. The direction of tumour motion for these patients is prominently in the cranial-caudal direction which is perpendicular to gantry and MLC motion therefore it is likely that the interplay effect would be minimal. For the cohort of lung patients considered, minor differences in DVH metrics were observed as the result of the interplay effect, with a maximum relative difference of 1% for $D_{0.1cc}$ (Spinal Cord). The impact of interplay effect was greater for OAR DVH metrics however still less than 2%. Previous patient studies which used 4D dose calculations to investigate the effect also observed minor dose differences [69–72]. In this work, no trends were observed for increasing tumour motion amplitude. The effects of motion uncertainties as a function of period were also investigated as time is an important factor for the interplay effect. However, no trend was observed even though there is a significant spread in tumour motion period for this patient cohort.

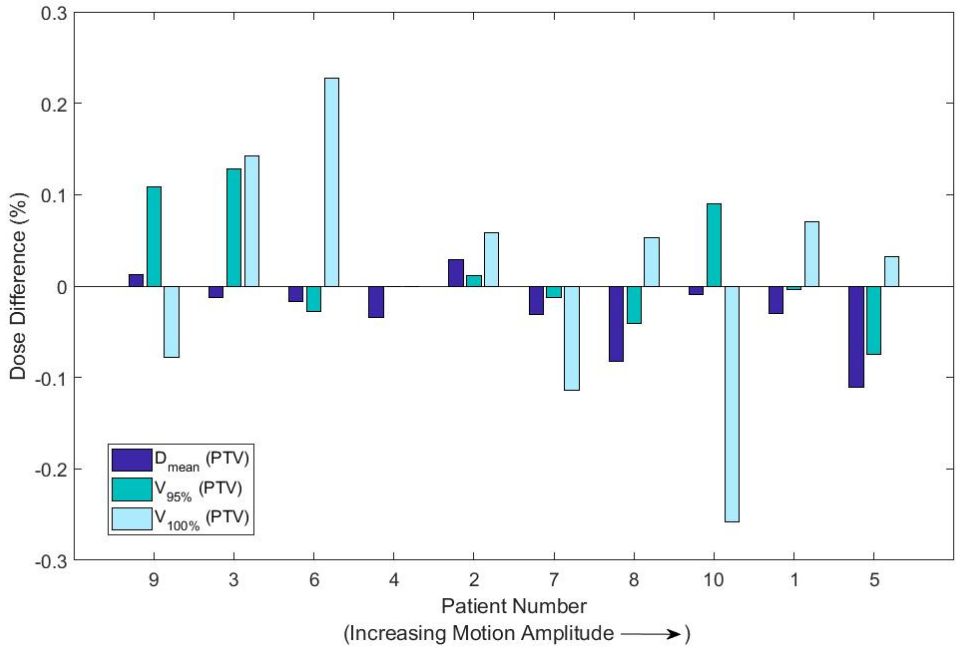

Figure 4.2: Differences of target DVH metrics in response to varying the starting phase. Patients are in increasing order of motion amplitude (from left to right).

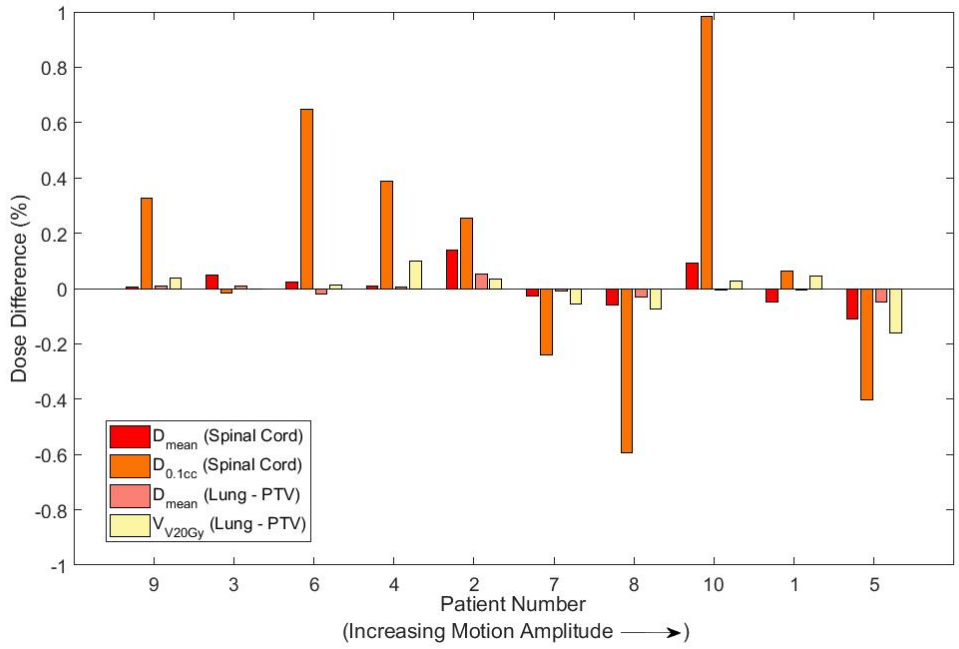

Figure 4.3: Differences of OAR DVH metrics in response to varying the starting phase. Patients are in increasing order of motion amplitude (from left to right).

4.3.2 Delivery Uncertainties

Blake et al. [45] investigated delivery uncertainties for the same patient datasets and showed ± 1 mm MLC field size errors resulted in significant differences in OAR DVH metrics. It was expected that even greater differences would be observed when taking into account tumour motion since greater volumes of OARs would be exposed.

Figure 4.4 shows the response of target DVH metrics to 0.5 mm MLC error that resulted in an increase in field size (of total +1 mm change) and figure 4.5 shows the response for OAR DVH metrics. For all patients at least one OAR DVH metric exceeded a 2% difference for this MLC error while the target DVH metrics were exceeded for a small subset of patients with $V_{100\%}$ (PTV) being the most sensitive. The smallest motion amplitude patient cases appeared to be impacted the most in terms of target DVH metrics therefore it is possible that the motion decreases the effects of MLC increase field size errors on target coverage. This should be evaluated further on a larger patient cohort in order to draw a statistically valid conclusion.

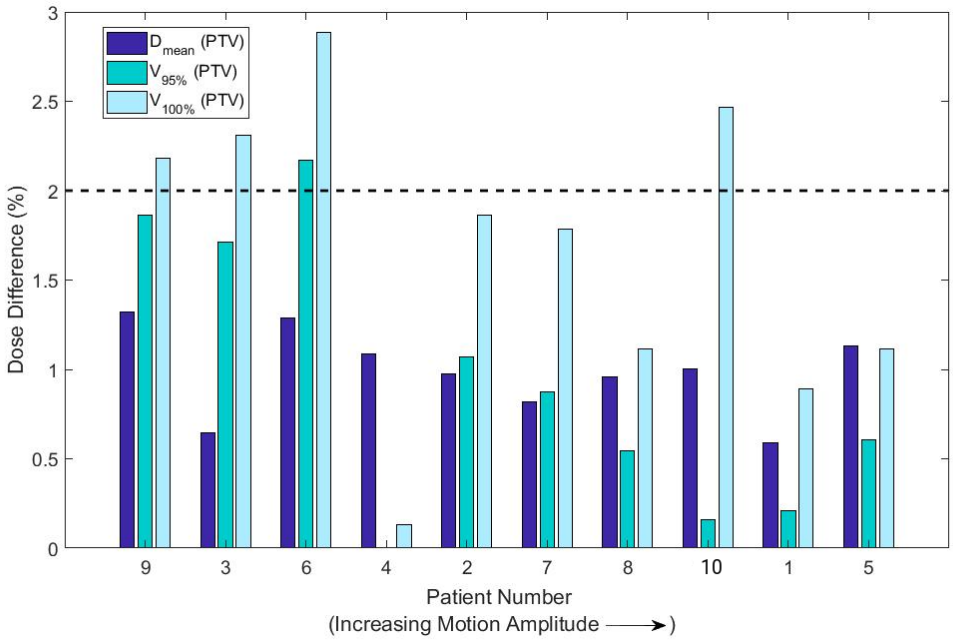

Figure 4.4: Differences of target DVH metrics for a MLC field size error of +1 mm, i.e. both banks of MLC shift outwards by 0.5 mm each. Patients are in increasing order of motion amplitude (from left to right).

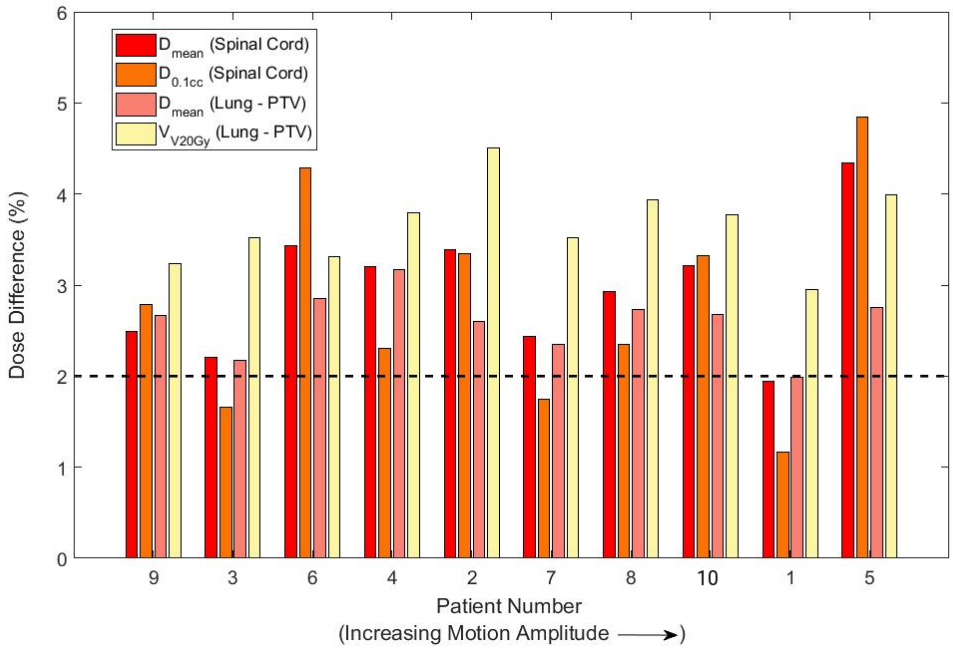

Figure 4.5: Differences of OAR DVH metrics for a MLC field size error of +1 mm, i.e. both banks of MLC shift outwards by 0.5 mm each. Patients are in increasing order of motion amplitude (from left to right).

For a 0.5 mm MLC error that resulted in a decrease in field size (of total +1 mm change), differences are shown in figures 4.6 and 4.7 for target and OAR DVH metrics respectively. Similarly to the increased field size error OAR DVH metrics were more sensitive to the error than target metrics. V_{20Gy} (Lung - PTV) was the most sensitive metric. All patient plans exceeded the 2% tolerance with these deviations observed for two or more OAR metrics.

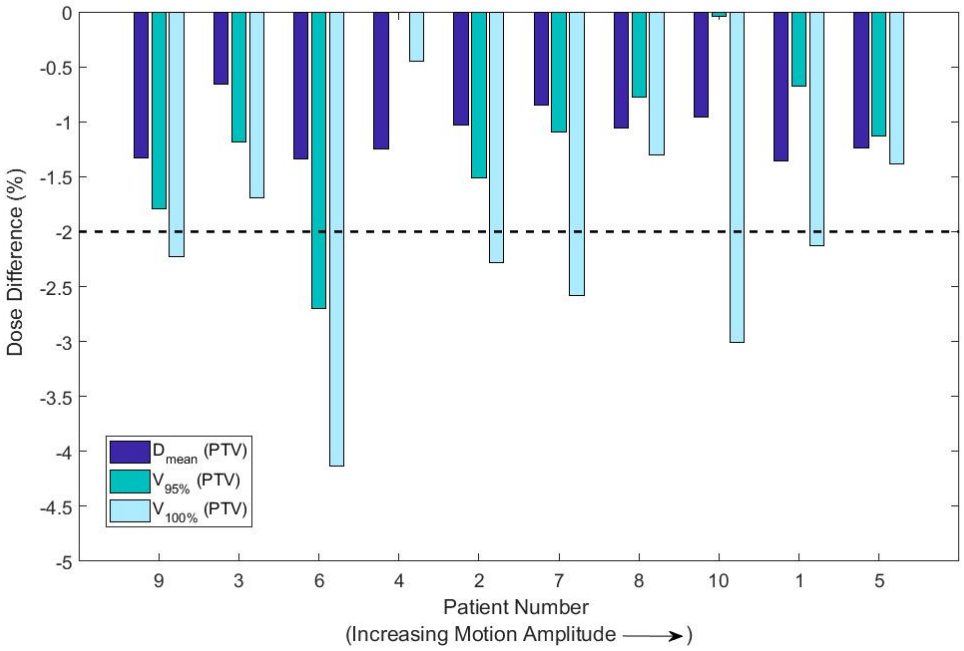

Figure 4.6: Differences of target DVH metrics for a MLC field size error of -1 mm, i.e. both banks of MLC shift inwards by 0.5 mm each. Patients are in increasing order of motion amplitude (from left to right).

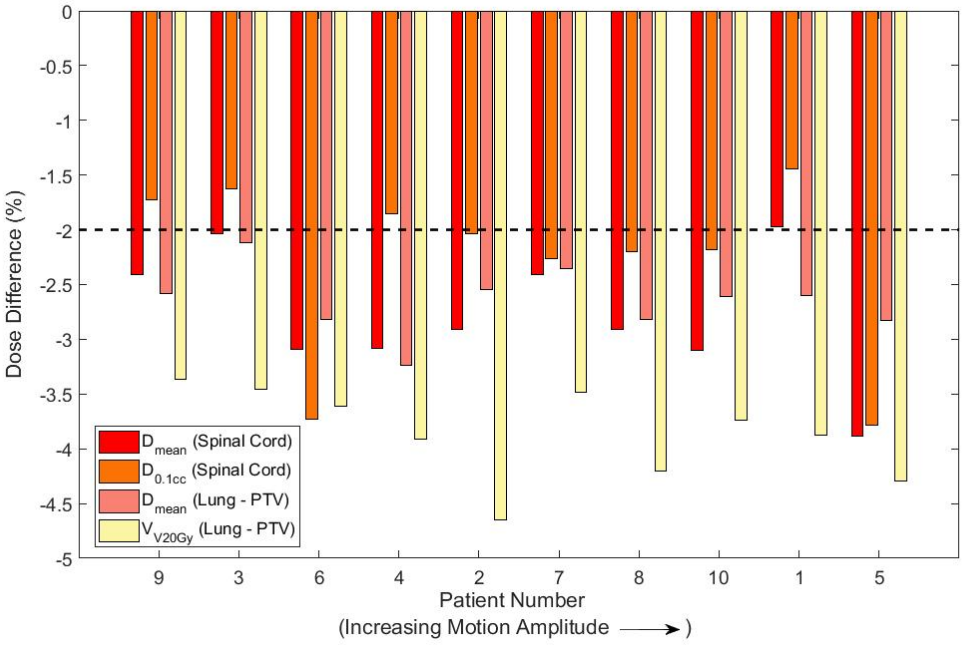

Figure 4.7: Differences of OAR DVH metrics for a MLC field size error of -1 mm, i.e. both banks of MLC shift inwards by 0.5 mm each. Patients are in increasing order of motion amplitude (from left to right).

It was expected that tumour size might effect the sensitivity of the plans to MLC

uncertainties since this was evident in chapter 3 when comparing plans with different PTV sizes. In this chapter no trend was observed for dose variations to MLC uncertainties as a function of tumour size. It is important to note that the planning techniques are different between the two studies and in chapter 3 the differences in PTV size are greater.

4.3.3 Limitations of Study and Considerations

In the first instance, this study only investigated MLC delivery uncertainties due to the volume of data per patient. Further work involving other delivery parameters e.g. gantry and collimator angle should be carried out. This study could be further extended to experimentally test the sensitivity of different dosimetry systems in detecting these purposely introduced errors.

Another limitation of the current study is the assumption that each phase was equally time-weighted; irregular breathing cycles could be considered in future studies. To create a realistic representation of the treatment 4D online imaging from each fraction could be used for calculations, as this includes information about variations in tumour motion compared with only using motion at the time of the planning 4DCT. However it is recognised that image quality is poorer for CBCT and therefore this could effect the dose calculations. Some other things to consider would be patient size and conditions of their lungs e.g. collapsed vs non collapsed, when evaluating the results.

A method to evaluate the uncertainties in accumulated dose using deformable image registration should be considered. Many different methods of which are proposed in the literature [195, 196], however this was beyond the scope of this thesis.

4.4 Conclusion

In this chapter 4D dose calculations for patient lung datasets were performed. The 4D Monte Carlo method proposed in chapter 3 was used to investigate the impact of motion and delivery uncertainties for different motion amplitudes and tumour geometries. The effect of interplay between MLC motion and target motion was minimal for all observed patient plans implying that for the mid-ventilation technique which was used for these

patients, is not prone to these uncertainties.

Uncertainties in MLC leaf positions impacted the plans more significantly, in particular OAR DVH metrics were sensitive to these errors, with at least one of the OAR DVH metrics varying by more than 2% compared to the baseline plan. Target coverage for the small motion amplitude cases appeared to be impacted more than extreme motion cases. It is possible that motion decreased the impacts of MLC leaf position errors however this should be evaluated further on a larger patient cohort. No trends were observed between the impacts of MLC uncertainties for varying tumour sizes.

Future work should involve investigating other types of delivery uncertainties. Smaller MLC errors should also be evaluated since the errors simulated in this study all resulted in significant differences. Thus in order to determine a specific tolerance for the technique studied here, further work needs to be carried out.

Chapter 5

4D Dose Calculations of Lung SBRT for Inline MRI-linac Systems: a Phantom Study

5.1 Overview

While there has been a great deal of research on delivery uncertainties for standard EBRT, no studies have investigated these errors on MRI-linac systems. This chapter investigates the effects of MLC systematic errors for a range of magnetic field strengths for inline MRI-linac systems. Two planning techniques for lung VMAT SBRT for a dynamic phantom were considered, an ITV-plan which encompasses the whole range of motion, and a TRACKING-plan where the couch is shifted to counteract the tumour moving. The latter being the likely treatment scenario on an MRI-linac. The 4DMC method which was introduced in chapter 3 was used to simulate the treatment plans. The primary aim of this study was to understand how or if delivery tolerances differ for inline MRI-linac systems as a function of the magnetic field strength.

5.2 Materials and Methods

5.2.1 Monte Carlo Simulations

The system as described in section 3.2.3 and 3.2.4 was used however rather than DOSXYZnrc for the phantom simulation, Geant4 version 10.5 was used. A magnetic field was included in the last stage of the simulation i.e. surrounding the phantom. The

assumption here is that the linac components are not affected by the magnetic field given that shielding can be placed around the electron gun and target. The Geant4 application reads in the phase space file produced by BEAMnrc from the treatment head simulations it sets the collimator and gantry angle around the patient/phantom. The Livermore Low-Energy physics models were used with a step limiter set to 1/3 of the voxel resolution. The dose grid resolution was $1.95 \times 1.95 \times 2$ mm^3 for the lung phantom. CT data was modelled as water with varying densities with 0.05 g/cm^3 bins ranging from 0.1 to 2.0 g/cm^3, similar to calculations performed in Pinnacle^3. The G4NestedParameterisation class was used for parameterisation of voxels as this reduces memory size and speeds up the simulation [197].

Since the Australian MRI-linac Monte Carlo model was under development at the time this study was undertaken, a conventional linac beam model was used. For consistency with the work presented in chapter 3 the same phantom 4DCT images and plans were used here. That is to say the plans were optimised without a magnetic field and the source-to-axis-distance (SAD) was 100 cm.

All magnetic fields modelled were uniform and inline with the beam direction. The strengths considered were 0.5, 1 and 1.5 T, these field strengths are approximately the same (in field strength) as the current MRI-linac designs. It was expected that for perpendicular magnetic fields that the differences in lung compared to without a magnetic field would be considerable due to the ERE [4]. Bol et al has shown that the ERE in perpendicular MRI-linacs can be compensated for by using opposing beams [112]. The work presented in this chapter focuses on inline systems since no compensation for the magnetic field was considered in plan optimisation.

5.2.2 MLC Errors Plans

Systematic MLC errors were deliberately introduced into the plans which included field size open and close shifts. These were chosen as they were deemed clinically unacceptable in chapter 3; that is they resulted in differences in $D_{95\%}$ (PTV) and/or D_{mean} (Lung) of $\pm 5\%$ [179]. The error plan just below the threshold was also simulated. Error plans for a given magnetic field strength were compared with the baseline plan i.e.

same field strength with no errors introduced; analysis as described in section 3.2.8 was performed.

5.3 Results and Discussion

5.3.1 Magnetic Field Strength Effects on Baseline Plans

All error plans were run without a magnetic field to ensure there was no change in results when running the patient simulations with Geant4 rather than DOSXYZ. The maximum variation observed in the dose differences between the two Monte Carlo codes without a magnetic field was 0.3% demonstrating the accuracy of the Geant4 application.

Table 5.1 gives the dose metrics ($D_{95\%}$ (PTV), D_{mean} (Lung)) of the baseline plans for all magnetic field strengths that were modelled. The mean dose to the lungs does not change with the magnetic field strength however PTV dose increases. This effect has been previously observed [115]. The forward focussing of the inline magnetic field results in reduced lateral scatter (usually prominent in lung) and thus the dose to the tumour is increased. The trend of increasing PTV dose with increasing magnetic field strength plateaus at 1.0 T. For the PTV volumes considered, 68.1 cm^3 for the ITV-plan and 32.6 cm^3 for the TRACKING-plan, the dose enhancement effect due to the inline magnetic field was not expected to be as significant as for smaller PTV volumes which was observed by Oborn et al. [115]. The plateau at 1.0 T was not observed in their study for smaller PTV volumes. The rate of increase in PTV dose with magnetic field strength has no strong dependence on plan type, also possibly due to the size of the PTV volume. A larger difference for the TRACKING-plan, as opposed to the ITV-plan, might be observed for smaller targets since the TRACKING-plan uses smaller fields thus lateral electronic disequilibrium (as a result of field size) would also take effect.

5.3.2 Magnetic Field Strength dependence for MLC errors

Figure 5.1 shows the dose differences in $D_{95\%}$ (PTV) and D_{mean} (Lung) for the ITV-plan calculated for varying magnetic field strengths for MLC field size errors. The change in mean dose to lung for different MLC errors is unaffected by the strength of the magnetic field. Similar results were seen for the TRACKING-plan in figure 5.2 with no change in

Table 5.1: Dose metrics calculated for the ITV- and TRACKING-plan, comparing the baseline plans for different magnetic field strengths.

	ITV-Plan		TRACKING-Plan	
	$D_{95\%}$ PTV (Gy)	D_{mean} Lungs (Gy)	$D_{95\%}$ PTV (Gy)	D_{mean} Lungs (Gy)
0 T	62.7	10.4	60.3	8.1
0.5 T	65.6	10.4	63.4	8.1
1 T	67.9	10.4	65.1	8.1
1.5 T	68.6	10.4	65.3	8.1

the dose difference for D_{mean} (Lung) when varying the magnetic field strength. For $D_{95\%}$ (PTV) all magnetic field strengths appeared to tighten the dose for a 2 mm field size error to within the $\pm 5\%$ tolerance limits. However, since D_{mean} (Lung) for the 2 mm error is greater than $\pm 5\%$ the plans would be deemed unacceptable regardless.

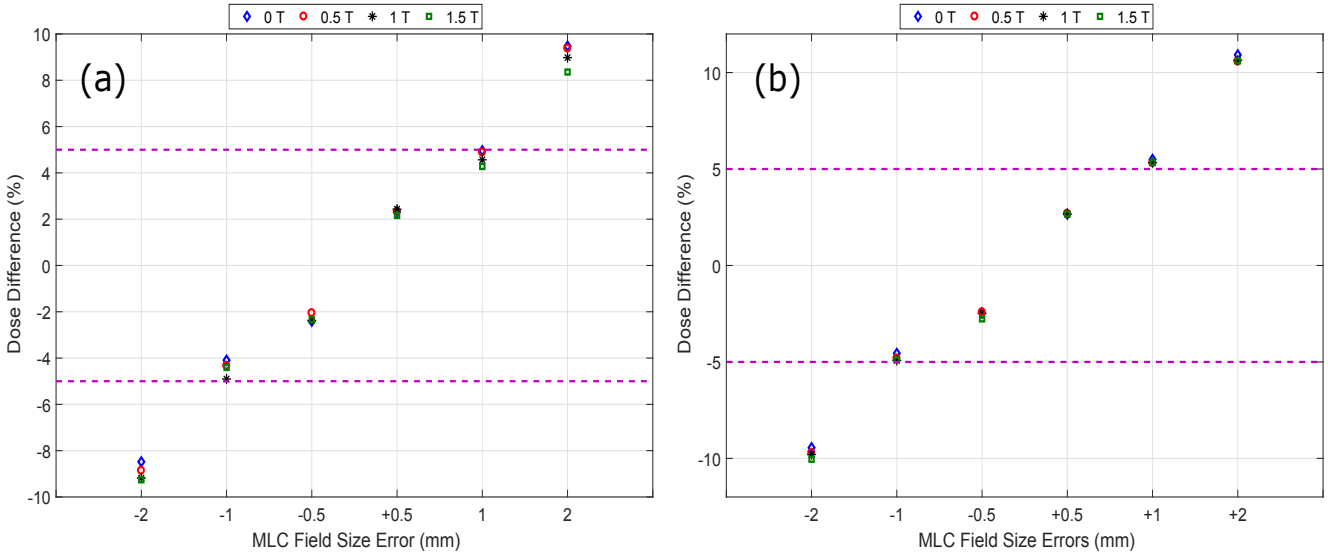

Figure 5.1: Dose difference of (a) $D_{95\%}$ (PTV) (b) and D_{mean} (Lung) for MLC field size errors for the ITV-plan. Dashed lines represent tolerance limits, $\pm 5\%$ dose deviation from baseline plans.

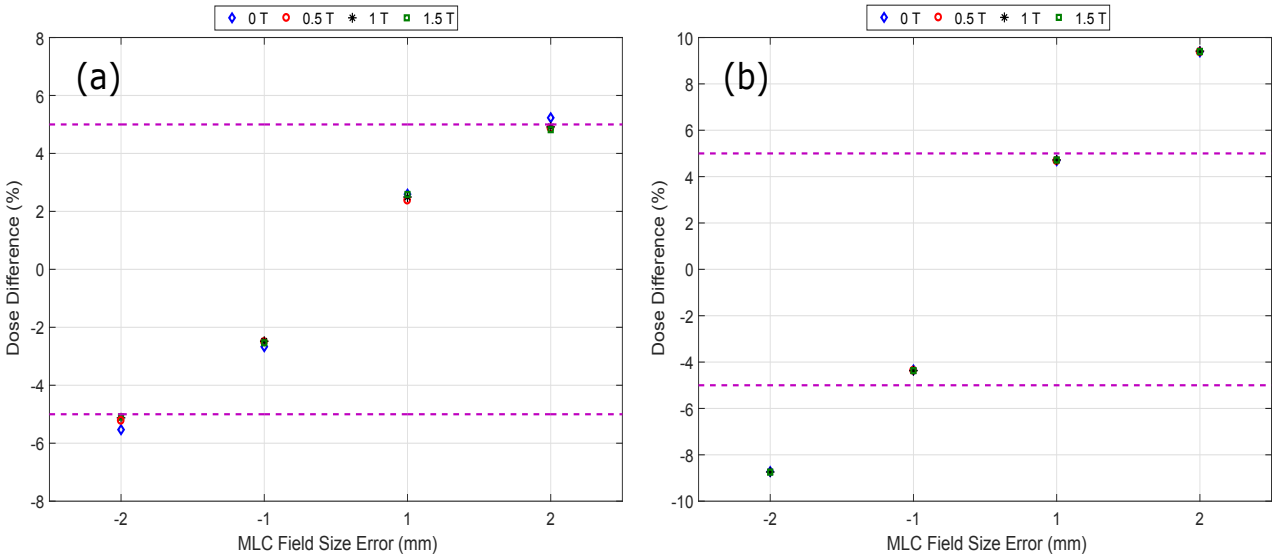

Figure 5.2: Dose difference of (a) $D_{95\%}$ (PTV) (b) and D_{mean} (Lung) for MLC field size errors for the TRACKING-plan. Dashed lines represent tolerance limits, $\pm 5\%$ dose deviation from baseline plans.

5.3.3 Limitations of Study and Considerations

This study only considered MLC uncertainties; since the Australian MRI-linac uses a fixed horizontal beam, gantry and collimator angle are non-existent. In the case of this system, any errors in MLC leaf gaps or modelling the leaf ends are magnified due to the greater SAD. What would be considered an inconsequential error at standard SADs could result in a significant difference for this system. It would be beneficial to consider these uncertainties at extended SADs e.g. 1.8 m and 2.4 m since these are the intended positions of treatment on the Australian system. Moving forward, it would be useful to model the radiation beam and magnetic field of the Australian MRI-linac. The 4D MC dose calculation tool could then be validated for MR-guided radiotherapy and used for quality assurance purposes; noting that to achieve this there are a lot of steps and procedures which would need to be developed.

Another limitation in the current study is that only one motion pattern and tumour size was considered. The simplicity of the phantom geometry is also a limiting factor. After addressing the aforementioned limitations the next steps would be to evaluate plans from patient data, similar to the work presented in chapter 4.

5.4 Conclusion

Simulations of two treatment plans for a dynamic lung phantom were performed for different inline magnetic field strengths. Overall, the inline magnetic field resulted in an increase in dose to the target while not changing lung dose. Increasing the magnetic field strength resulted in further increase in target dose, which has been previously observed. The trend between the dose enhancement and field strength will also vary with field size, therefore future work should consider smaller PTV sizes.

MLC systematic uncertainties were simulated for the different inline magnetic fields. The impact of delivery uncertainties did not vary with magnetic field strength however it is suspected that this might not be the case for smaller target volumes. In terms of the Australian MRI-linac system, any errors in MLC leaf gaps or modelling the leaf ends are magnified due to the greater SAD.

Future work should include simulations using the 4DMC framework of with the Australian MRI-linac beam model at the intended treatment SAD and investigate a range of different tumour sizes and respiratory motion patterns. In order for this to be achievable, a model of the Australian MRI-linac beam must be developed in both the TPS and Monte Carlo.

Chapter 6

High Resolution Dosimetry in Magnetic Fields for the Characterisation of Magnetically Focused Contaminant Electrons

Some of the results presented in this chapter have been published in the journal Medical Physics:

N. F. Roberts, E. Patterson, U. Jelen, T. Causer, L. Holloway, G. Liney, M. Lerch, A. B. Rosenfeld, D. Cutajar, B. M. Oborn P. Metcalfe, "Experimental characterization of magnetically focused electron contamination at the surface of a high-field inline MRI-linac", Med. Phys. 46 (12), 5780-5789.

6.1 Overview

The dose response of detectors can be influenced by magnetic fields [128–130, 133, 137, 138]. This chapter investigates the response of solid state detectors, namely the microDiamond (PTW, Feriburg, Germany) and MO*Skin*^{TM} (CMRP, Wollongong, Australia) in MRIgRT environments. While Gafchromic film is a high resolution 2D dosimeter, solid state detectors are advantageous as they are not single-use and they have real-time readout systems. The microDiamond is a commercial detector commonly used for small field dosimetry due to its high spatial resolution and approximate water equivalence [198]. The microDiamond's performance in transverse MRI-linacs has been

previously studied [139–141] and has proven to be suitable for MRI-linac commissioning and quality assurance. The MO*Skin*™ is a metal oxide semiconductor field effect transistor (MOSFET) detector developed by CMRP. It has a high spatial resolution in the micron range. The effective point of measurement (EPOM) of the MO*Skin*™ is equivalent to the radiosensitive layer in the skin defined by ICRP as 0.07 mm [199]. I-V characteristics of this detector system have been tested in a magnetic field [200], compared with 0 T, differences were shown to be insignificant in a 1 T magnetic field for both beam to magnetic field orientations. The MO*Skin*™s relative response in MRIgRT environments is still to be tested.

On the Australian MRI-linac a measure of surface dose is important to be able to characterise the high electron contamination region [107]. This region exhibits a high dose gradient and therefore dosimetric measurements require detectors with a high spatial resolution. MO*Skin*™ has been shown to accurately measure skin dose [201] and the build-up region [202] on standard clinical linacs which exhibit a steep dose gradient, electronic disequilibrium conditions and contain electron contaminants. It was therefore expected that the MO*Skin*™ would give an accurate measure of the magnetically focused contaminant electrons on the Australian MRI-linac.

This chapter primarily investigates the relative response of these detectors in magnetic fields, determining which measurements on inline MRI-linacs they would be most useful. The second objective was to characterise the high electron contamination region of the Australian MRI-linac.

6.2 Materials and Methods

6.2.1 Detectors and Film

The detectors and dosimeter used in this chapter were a synthetic microDiamond 60019 (PTW, Freiburg, Germany), MO*Skin*™ and Gafchromic® EBT3 film. Some details of each have been included in table 6.1 while any additional information is given in the text.

Table 6.1: Characteristics of the detectors and dosimeter used in this chapter, these are specification given by the vendors. *This is based on the scanning resolution used in this study.

Detector / Dosimeter	Spatial Resolution (mm)	Sensitive Volume (mm^3)	EPOM (mm)	Covering Layer(s)	$\approx$ Z
microDiamond	2.2	0.004	1	0.3 mm RW3, 0.6 mm epoxy, 0.01 mm aluminum	6
MO*Skin*™	0.00065	0.0000015	0.07	0.05 mm polyamide	14
Gafchromic® EBT3	0.35*	N/A	0.139	0.125 mm polyester substrates, 0.014 mm active layer	6.71

The microDiamond detector was connected to a UNIDOS electrometer for read out of measurements with the detector oriented with the long axis parallel to the beam unless otherwise specified.

The MO*Skin*™ detector and readout system were developed by CMRP. The operation of the detector relies on secondary electrons generated from interactions in the polyamide layer creating electron-hole pairs in the gate oxide, reducing the current across the source and drain (beneath the gate). The readout system gives a measure of the voltage required to push a fixed current between the source and drain, defined as the threshold voltage [203]. The sensitivity of the detector to radiation dose decreases over large voltage ranges, therefore this was corrected for by taking a reference reading at the beginning and end of each set of measurements. The MO*Skin*™ is a silicon detector and has been shown to over-respond at low energies due to the photoelectric effect being dominant for higher Z materials [204].

Gafchromic® EBT3 film was used as a reference since previous studies have shown the effect of the magnetic field on the relative response is negligible [152, 153, 170]. The guidelines outlined in AAPM Task Group 55 [205] for using radiochromic film for dosimetry were followed. The film was scanned on a EPSON 10000XL flatbed scanner with resolution of 72 dpi, in 48-bit RGB format and colour corrections turned off. Each film was placed in a consistent location on the scanner for the post and pre scans. The batch of film used was calibrated on Varian Truebeam (6X FFF) (see figure 6.1). All analysis was performed using MATLAB®. Data presented in this chapter takes into account the EPOM for each detector and film.

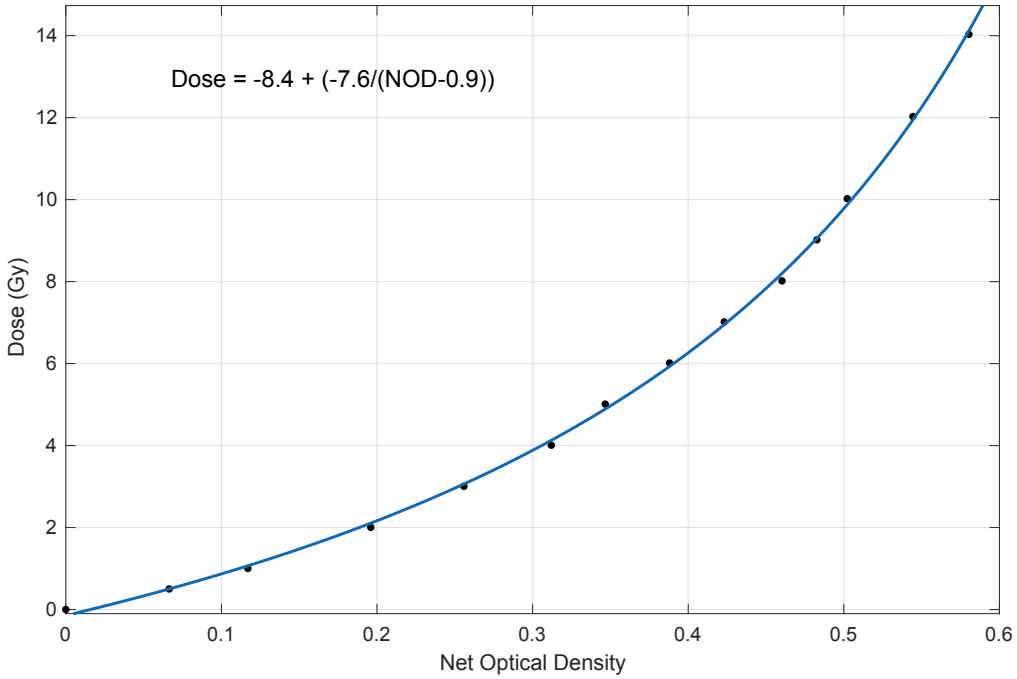

Figure 6.1: Gafchromic EBT3 calibration curve. Equation used to calculate dose (Gy) from the net optical density.

6.2.2 Measurements and Simulations on MARDOS

MARDOS

A permanent magnet system named Magnetic Apparatus for RaDiation Oncology Studies (MARDOS), which has been previously described [116] was used to test the microDiamond's response in a magnetic field. MARDOS consists of neodymium-iron-boron magnets with steel focusing cones [116] which are used to

concentrate the flux over a small volume; a smaller gap results in a stronger magnetic field. The system is used in combination with a clinical linac, typically positioned at 1.5 m source-to-isocentre with the beam entering horizontally, the setup is shown in figure 6.2. The magnetic field was 0.95 T for all MARDOS measurements presented in this chapter. The steel cones can be removed from the system and setup in an identical jig in order to replicate the scattering conditions for 0 T measurements.

Simulations

The Monte Carlo toolkit, Geant4 (version 10.02.p01) was used to run simulations with a water-only geometry, allowing for separation of the detector response from effects of the magnetic field on the radiation beam. The magnetic field and beam model used for these simulations have been previously benchmarked [116, 144, 177]. The number of electrons incident on the linac target were 2×10^8 which were scored in a phasespace 0.942 mm above the magnets isocentre, particles were recycled 199 times at that plane.

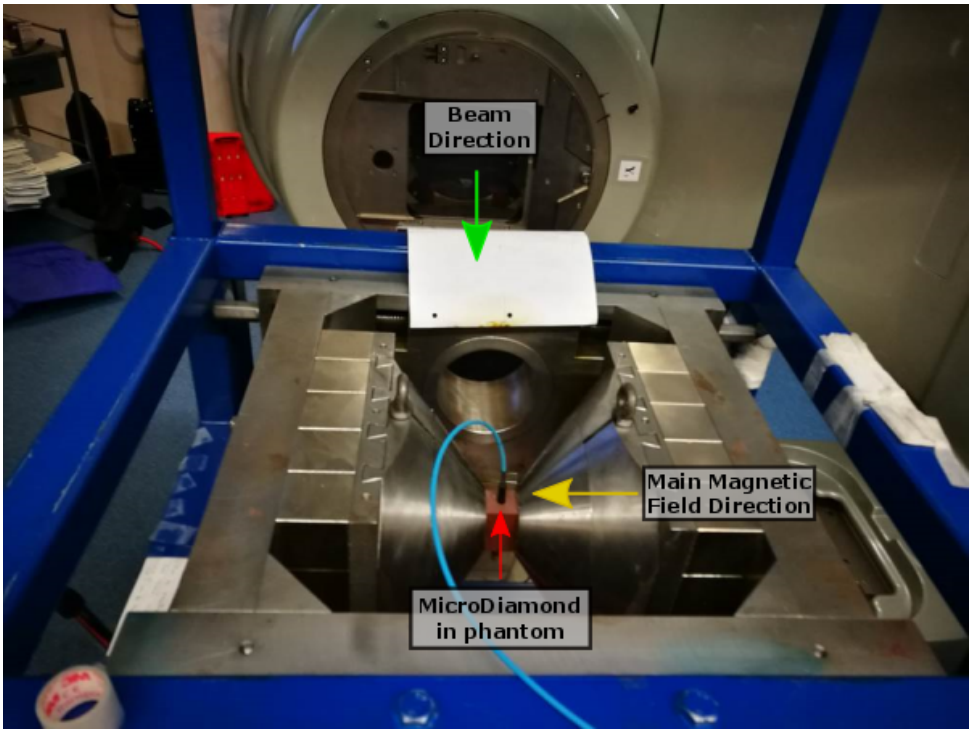

Figure 6.2: MicroDiamond in a solid water phantom inside MARDOS with the linac beam entering horizontally, this shows the perpendicular magnetic field orientation.

Perpendicular Orientation

The magnet system was orientated perpendicular to the clinical beam. The microDiamond was positioned at 1.5 cm depth in a solid water phantom (Gammex-RMI, Middleton, WI, USA) with the long axis perpendicular to the beam and magnetic field. Profiles of a 0.9×0.9 cm^2 beam were taken with and without the magnetic field. Simulations calculating dose to water were performed as a reference, since it was expected that microDiamond would underestimate the magnetic field induced lateral shift of the profile [139].

Inline Orientation

Measurements were also performed with the magnetic field inline with the radiation beam; the microDiamond was at 1.5 cm depth with the detector's long axis parallel to the beam. These measurements replicate the conditions and intended setup of the microDiamond for the Australian MRI-linac. Output factors for a range of square jaw defined field sizes, from 0.9 to 2.4 cm^2, at 0 T and 0.95 T were taken to quantify the dose response of microDiamond in MRIgRT environments. Simulations were used in this instance to determine the increase in dose per incident particle as a result of the inline magnetic field.

6.2.3 Measurements and Simulations on the MRI-linac

MRI-linac

The current prototype of the Australian MRI-linac includes a 6 MV flattening filter free (FFF) linac, Varian Linatron-MP (Varex, UT, USA), a stand-alone multileaf collimator and a 1 T split-bore MRI (Agilent Technologies, Oxford UK). The linac does not rotate around the patient as a typical linac would, because the beam must always be parallel to the magnetic field the only options to achieve different beam angles are to rotate the magnet with the beam around the patient or rotate the patient with a fixed beam. The Australian MRI-linac has been setup for the latter, therefore the linac beam is always horizontal to the phantom/patient. This system has the unique feature that the linac and MLC are mounted on a rail system so that the source-to-MRI-isocentre (SID) distance can be varied. This also allows for measurements to be performed with the phantom at different magnetic field strengths while maintaining a constant source to surface distance (SSD).

SIDs of 3.269 m and 1.819 m were used in this chapter which correspond to the maximum and minimum distances (from the MRI) achievable with the rail system. The two set ups are shown in figure 6.3 with an overlay of the magnetic field map. With the linac at the furthest position from the MRI, the phantom was positioned in the region of the fringe field where there is a point of inflection; the magnet has been actively shielded to achieve a low fringe field here. This is where the magnetic field is closest to 0 T, hereon referred to as near 0 T measurements. The field strengths quoted were measured with a gauss meter. The largest magnitude for near 0 T measurements was at the back of the phantom reading 0.05 T. The magnetic field strength at the linac target in this setup is 0.0007 T. When the linac source was at 1.819 m from isocenter, the phantom was set up with the surface in the center of the bore, where the magnetic field is 1 T. For this set-up the linac is within the fringe field of the magnet with a measured magnetic field strength around the target of 0.033 T.

To reduce the effect the magnetic field has upon the beam characteristics, magnetic shielding was placed around the linac target so that beam profile symmetry fulfilled IEC 60976/977 criteria [206, 207]. This criteria states that the ratio of absorbed doses at two positions symmetrically displaced from the radiation beam axis and within the flattened area at a standard measurement depth should be less than 103%.

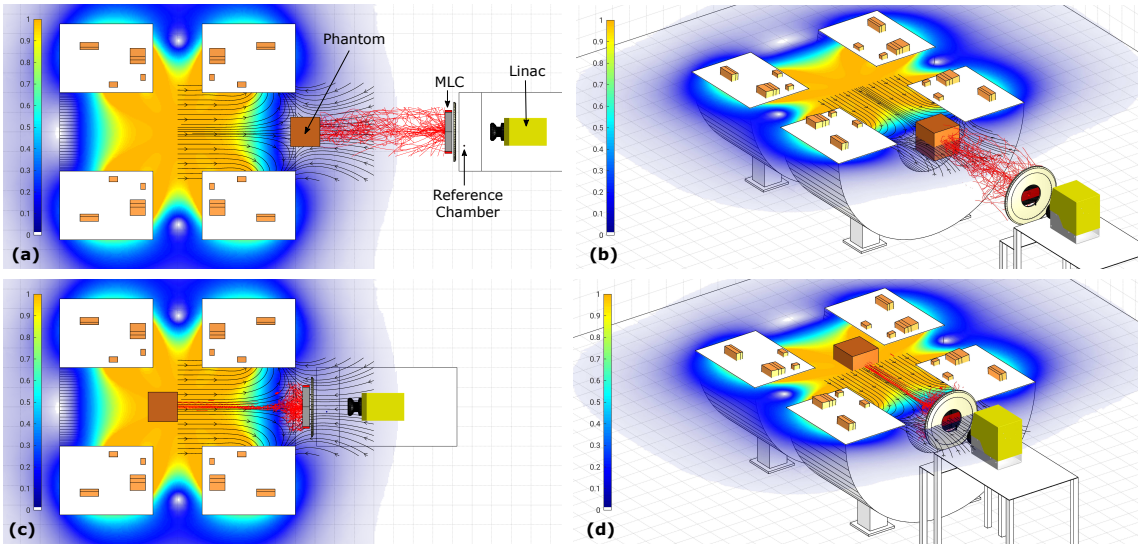

Figure 6.3: Visualization of two different setups. (a-b) Near 0 T setup with source-to-MRI-isocenter distance of 3.269 m and the phantom positioned at 1.819 m from the source. (c-d) 1 T setup with source-to-MRI-isocenter distance of 1.819 m and the phantom position 1.819 m from the source. Magnetic field maps are overlaid (units: T). The red paths represent the secondary electron tracks between the MLC and phantom surface. The magnetic focussing of the electrons can be seen in (c-d).

Phantom Setup

The phantom used for all measurements was a 30 $\times$ 30 $\times$ 30 cm^3 solid water block. A piece of solid water was machined for each detector to minimise air gaps, these are shown in figure 6.4. Although solid water phantoms are not recommended for MRI-linac dosimetry, the presence of air gaps in an inline magnetic field is expected to have minimal impacts as opposed to the perpendicular systems [109].

Angular Dependence

Woodings et al. [140] investigated the angular dependence of the microDiamond in a perpendicular magnetic field and found variations up to 9.7% for a 60° angle. Since the Australian MRI-linac is a fixed, horizontal beam the detector would only be used in the face-on orientation, i.e. with the stem parallel to the beam axis, or edge-on with the stem perpendicular to the beam axis. The detector was at 15 cm depth with measurements taken at 0° (detector face-on) and then rotating the phantom by 90° (detector edge-on), in both rotational directions, see figure 6.5. The SID distance used was 1.819 m and field size of 10.1 $\times$ 9.7 cm^2.

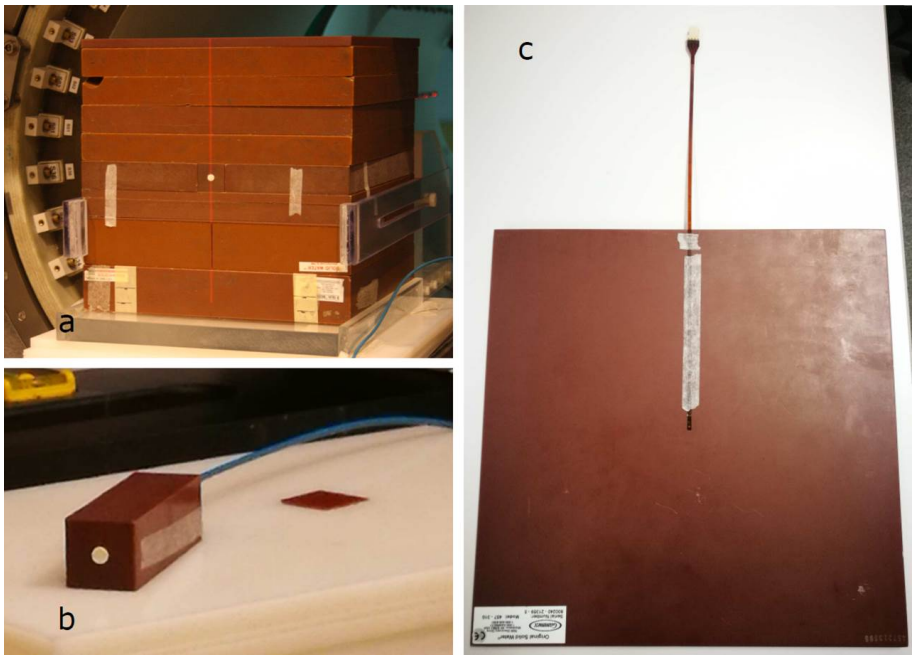

Figure 6.4: (a) 30 × 30 × 30 cm^3 phantom outside of the MRI with dedicated stand to hold vertical solid water slabs, (b) the microDiamond phantom, (c) the MO*Skin*™ phantom.

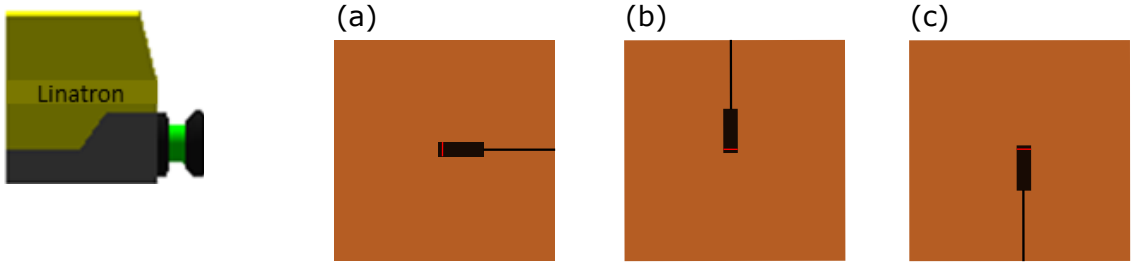

Figure 6.5: Central slice of phantom, looking from above at (a) 0° (detector face-on), (b) -90° (detector edge-on), (c) +90° (detector edge-on). Linatron not to scale.

Beam Data Measurements

PDDs were collected with each detector for a range of field sizes, these were 2.2 × 1.9, 6.1 × 5.8, 11.8 × 11.5, 23.5 × 23 cm^2 (field size at the phantom surface). MO*Skin*™ measurements were taken with the solid water phantom placed vertically, the SSD remained constant while the depth was varied by placing solid water pieces in front of the detector and shifting it back on a dedicated stand (pictured in figure 6.4a). Skin dose was measured with the MO*Skin*™ at the surface layer. The microDiamond detector was placed in the solid water phantom orientated horizontally, the depth was varied by shifting the detector inside its machined rectangular block back and placing in front equivalent sized square pieces (3 × 3 cm^2) of solid water (both pictured in figure 6.4b).

The phantom was set up in the two different magnetic field regions of near 0 T and 1 T; an SSD of 1.8 m was maintained. Film was placed at selected depths of 1, 10, 15, 20, and 50 mm, whereas MO*Skin*^{TM} and microDiamond were used to obtain a high resolution PDD near the surface and depths up to 200 mm. To ensure the detectors were placed in the centre of the high electron contamination region for measurements inside the magnetic field, film was placed on the surface and visually inspected prior to performing the set of detector measurements. All depth dose curves were normalised at 50 mm depth, this was chosen because for measurements inside the MRI bore this depth is far beyond the contaminant electron region. However the PDDs are expressed as the percentage dose of the maximum dose for the near 0 T measurements.

The dose delivered was adjusted depending on the detector type and the depth in order to maintain a high signal to noise ratio. The linac output was monitored with a Farmer-type ionisation chamber FC-65G (Scanditronix Wellhöfer) with readout from the FLUKE 35040 Advanced Therapy Dosimeter. The reference chamber was placed in air, between the linac and MLC, within the beams field so each measurement could be corrected for variations in the linac output (see figure 6.3). The reference chamber was in the same position within the fringe field for the 1 T setup (0.05 T) therefore magnetic field conditions were consistent across these measurements.

Simulations

The setup with the phantom at 1 T was simulated with Geant4 (version 10.05) in order to investigate the energy spectra of the contaminant electrons. The Monte Carlo beam model which will be described in greater detail in chapter 8 was used, with the magnetic field map (shown in figure 6.3). A phasespace of particles passing through a plane were scored at various depths in the phantom (position at isocentre), the depths were the surface and up to 5 mm with a plane at every 1 mm. The field size simulated was the 11.8×11.5 cm^2.

6.3 Results and Discussion

6.3.1 Measurements and Simulations on MARDOS

Perpendicular Orientation

Profiles of a 0.9 × 0.9 cm^2 beam measured with MARDOS setup in the perpendicular orientation are shown in figure 6.6. The lateral shift measured in water is 0.6 mm on both the left and right side of the profile. The microDiamond measurements appear to underestimate the shift however since the uncertainty in positioning the detector is comparable to the shift, it is difficult to quantify the underestimation for this field size. In order to accurately acquire profiles with the microDiamond orientation this way it would be beneficial to use a translational stage in a water tank to increment the detector position, although such a system would need to be specifically designed to operate in magnetic fields. The microDiamond was expected to underestimate the shift due to the high-Z materials in the detector housing [208] which would reduce the path length of the secondary electrons which are moving in circular trajectories. These results were previously observed by O'Brien et al. [139].

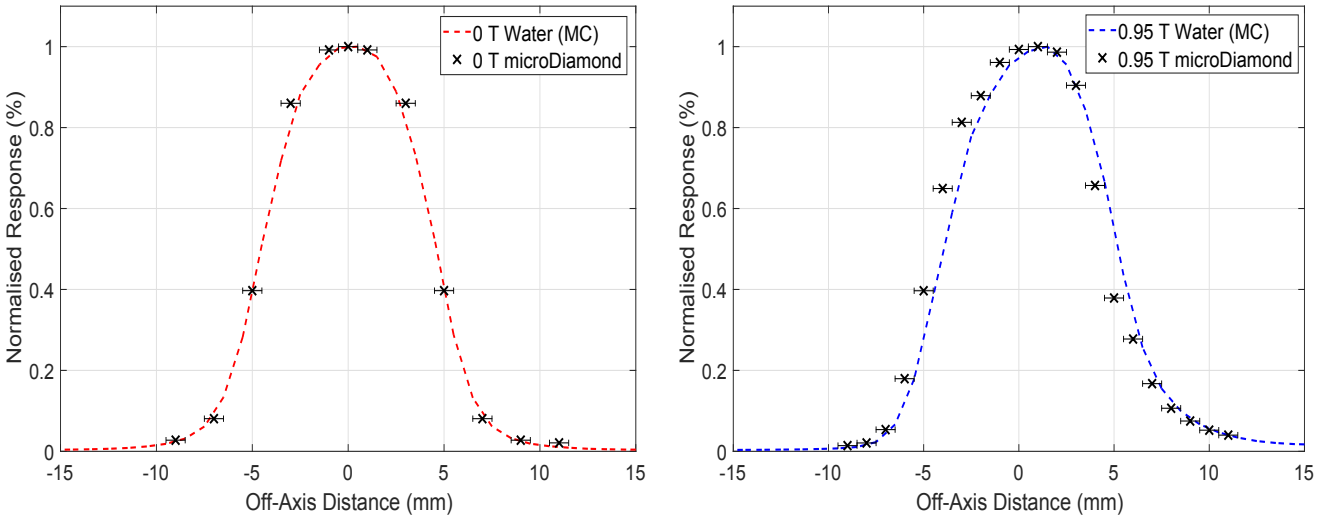

Figure 6.6: microDiamond-measured (×) and Water-Monte Carlo (MC) generated (- - -) profiles of a 0.9 × 0.9 cm^2 radiation field, at 0 T (a) and in the presence of a 0.95 T magnetic field (b). Profiles were acquired with MARDOS in the perpendicular configuration. Uncertainty in detector position of ±0.5 mm.

Inline Orientation

The microDiamond under non-magnetic field conditions has been shown to over-respond for small field sizes i.e. less than 2 cm^2 [209] due to the detector housing perturbing the charged particle fluence. The response in an inline magnetic field with the detector in the orientation intended for the Australian MRI-linac was investigated for a range of field sizes, as shown in figure 6.7. The response increases as field size decreases for square fields less than 1.8 cm^2, whereas for the larger field sizes it is a relatively constant over-response of 1.5%. Simulations predict a 1% increase in dose to water along the central axis in this magnetic field (compared to 0 T), therefore the remaining 0.5% of the increase measured is an over-response caused by the magnetic field. For field sizes smaller than 1.8 cm^2, the increase in response with decreasing field size is a similar trend to the over-response seen for small field sizes in non-magnetic field conditions. These results inferred that for a 1 T inline magnetic field the microDiamond could be used for field sizes greater than 1.8 cm^2 without having to apply field size corrections. The large uncertainty in the measurements, particularly at the smaller field sizes, is due to the positional accuracy of the jaws.

6.3.2 Measurements on the MRI-linac

Angular Dependence

The angular dependence of the microDiamond was investigated by measuring the extreme cases for the system i.e. with the detector at a 90° angle, both negative and positive with respect to the beam direction. Results are expressed as a ratio of the reading at a 90° angle to the reading at 0°. When the detector was at +90° the response was 1.015 ± 0.004 whereas for -90° it was 1.003 ± 0.002. Differences in response between the two detector arrangements could be due to the direction of rotation of the spiralling electrons with respect to the detector housing. If the detector face is in the direction where the electrons spiral towards it the response will be higher. When the detector is in the other orientation, the electrons will be passing through the materials behind the sensitive volume which have a higher density therefore more electrons will be stopped before reaching it. These results indicate that the largest possible change as a result of the inline field was 1.5% which is within the range specified by the manufacturer [198] for measurements taken without a magnetic field. An angular dependence for the microDiamond has been observed

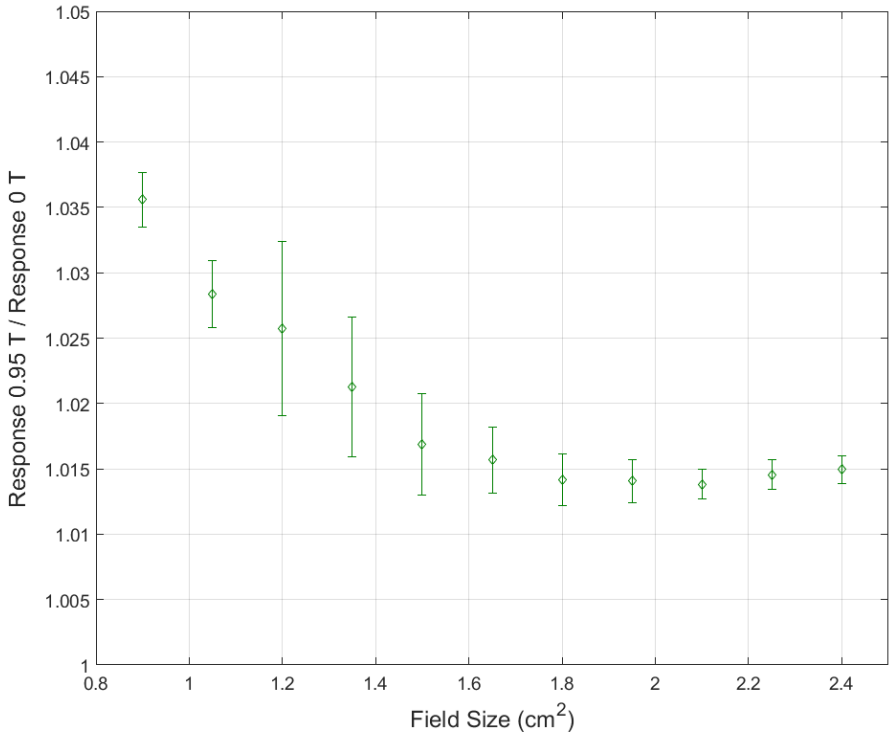

Figure 6.7: Ratio of the response of microDiamond in a 0.95 T inline magnetic field to the response without a magnetic field for a range of field sizes, from 0.9 to 2.4 cm^2. Uncertainties include one standard deviation of measurements.

in a transverse 1.5 T field [140]. On the other hand other studies indicate minimal dependence for the PTW60003 diamond detector [130, 138] for a low field strength and inline orientation which is in agreement with the results presented.

Beam Profiles

In order to determine the magnitude of dose and size of the high electron contamination region, film measurements to encapsulate the entire field were taken at 1 mm depth for the 11.8 $\times$ 11.5 cm^2 field size inside and outside the magnetic field. Profiles are shown in figure 6.8, the 2D dose distribution in the magnetic field is also represented on the right side. The in field hot spot for this field size, peaking at 306%, has a diameter of approximately 8 cm and displays a steep dose gradient moving off-axis. Therefore both longitudinal and lateral electronic disequilibrium exists in this region. The near 0 T profile has a larger umbra region compared to the 1 T profile which rapidly drops off to zero. The contaminant electrons produced in the linac head which reach the patient deposit their energy in the first few millimetres, the dose in the umbra region outside the magnetic field

is caused by the energy deposition of these contaminant electrons. When the phantom is inside the magnetic field the contaminant electrons are focused along the central axis and therefore the dose from the umbra region is shifted to the central region, hence the rapid drop off at the field edge for the 1 T profile.

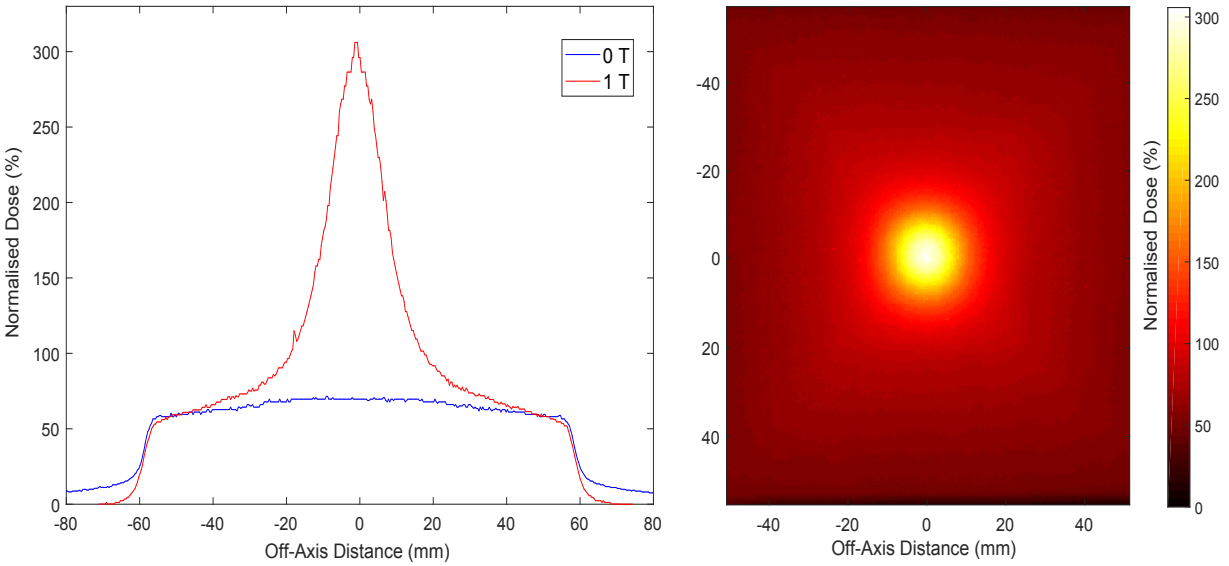

Figure 6.8: Profiles at 1 mm depth for a 11.8 × 11.5 cm^2 field both inside the magnet (1 T) and outside the magnet (near 0 T) as measured with EBT3 film. On the right is a 2D dose distribution from the film inside the magnet, displaying the high electron contamination region. All film data was normalised at 50 mm depth however expressed as the percentage dose of the maximum dose for the near 0 T measurements.

Percentage Depth Dose Curves

PDD results for the smallest field size, 2.2 × 1.9 cm^2, for both magnetic field setups are shown in figure 6.9. These measurements were acquired with microDiamond, MO*Skin*™ and Gafchromic® EBT3 film. Both detectors agreed with film within uncertainty for the near 0 T measurements with the exception of the microDiamond at 1 mm depth. The MO*Skin*™ detector showed no change in relative response in a magnetic field for depths greater than 20 mm. The uncertainties of the MO*Skin*™ measurements are displayed as shaded error bands, microDiamond showed minor deviations between repeated measurements therefore uncertainties are too small to be seen on graphs. The estimated uncertainty in film results is 3.4%, inclusive of scanner uniformity, film reproducibility and calibration uncertainties [210]. The film uncertainties within the region of the high electron contamination region (i.e. the first 20 mm) also include the range of the

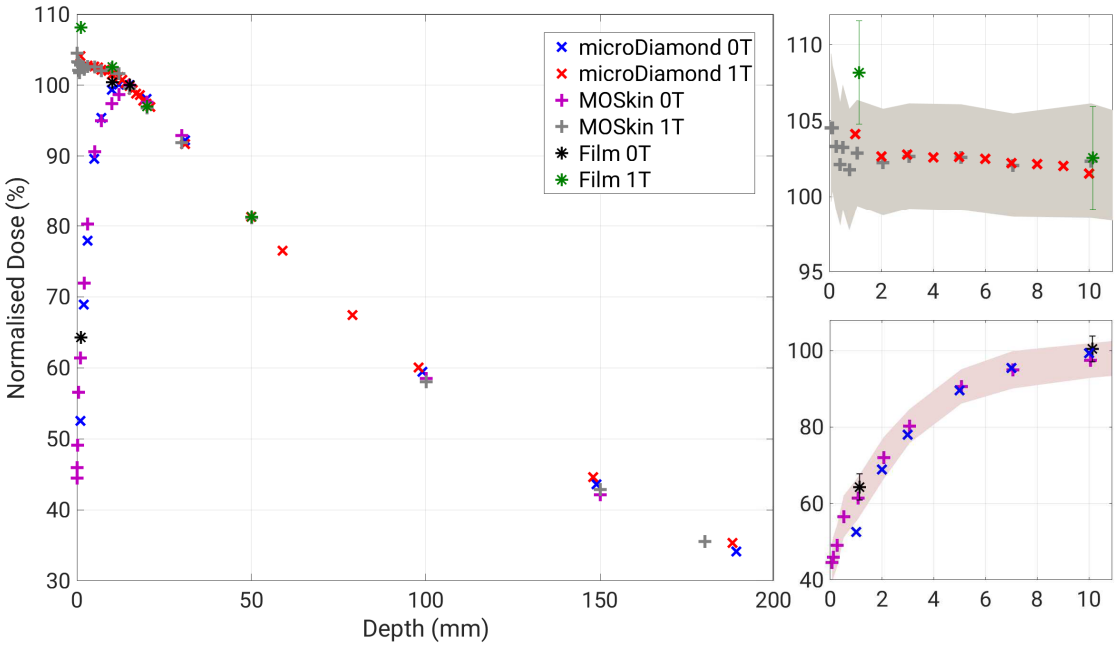

Figure 6.9: Depth dose curves for a 2.1 × 1.9 cm^2 field as measured with microDiamond (×), MO*Skin*^{TM} (+), and EBT3 film (*) in both magnetic field regions. The top right graph is the 1 T near-surface data magnified and the bottom right graph is the near 0 T near-surface data magnified. microDiamond had a maximum uncertainty of 0.4% (near 0 T) and 0.3% (1 T). MO*Skin*^{TM} uncertainties are displayed as shaded error bands.

maximum doses measured with film. For the 1 T measurements at approximately 1 mm depth, microDiamond (104.1%) and MO*Skin*^{TM} (102.9%) agree, film gives a significantly higher dose (108.2%) however taking into account the uncertainty in film and MO*Skin*^{TM} in this region they are in agreement. It should be noted that the effective depth of each detector and film are different therefore it is not possible to directly compare depth points between the detectors particularly within high dose gradient regions.

Figure 6.10 displays the 6.1 × 5.8 cm^2 PDD results, between 20-200 mm there is good agreement comparing near 0 T and 1 T measurements for both detectors. Similar trends in detector response were observed for the 11.8 × 11.5 cm^2 PDD, represented in figure 6.11, and the largest field size, 23.5 × 23 cm^2, shown in figure 6.12. Overall the relative response of both microDiamond and MO*Skin*^{TM} were confirmed to be unaffected by the magnetic field. This result was shown for the microDiamond in previous studies for perpendicular systems [140, 141]. Film results at 20 mm depth agreed with both detectors in all setups, further demonstrating the relative response of these detectors does not change in the presence of a 1 T inline magnetic field.

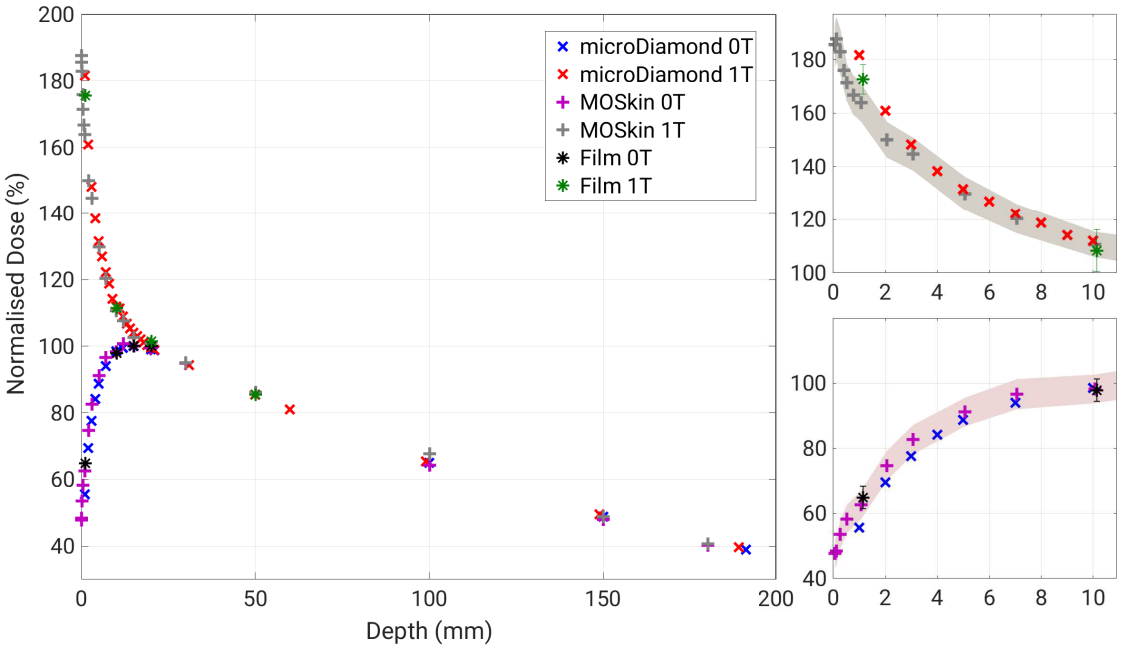

Figure 6.10: Depth dose curves for a 6.1 × 5.8 cm^2 field as measured with microDiamond (×), MO*Skin*^{TM} (+), and EBT3 film (*) in both magnetic field regions. The top right graph is the 1 T near-surface data magnified and the bottom right graph is the near 0 T near-surface data magnified. microDiamond had a maximum uncertainty of 0.1% (near 0 T) and 0.3% (1 T). MO*Skin*^{TM} uncertainties are displayed as shaded error bands.

Overall the biggest differences between the detectors for the 1 T setup were in the near surface region, seen by graphs in the top right side of figures 6.9-6.12. MO*Skin*^{TM} measurements produced a shallower dose gradient near the surface compared to microDiamond. The dose gradient in the first 5 mm is steep therefore giving rise to larger uncertainties in this region. These differences could be due to positioning the detector in the centre of the high electron contamination region, however this is less likely since measurements performed over multiple days gave consistent results. It is possible that the microDiamond was over-responding in this region; since there is a high fluence of low energy electrons the microDiamond detector components could result in perturbations of the charged particle fluence. In electronic disequilibrium conditions, it has been shown that high density detectors will over-respond [209, 211]. Although the sensitive volume of the microDiamond is small, the detector houses high density materials such as 400 μm thick diamond chip and an aluminium electrode [208], which could explain why the measurements near the surface at 1 T are higher than film and MO*Skin*^{TM}. The spatial resolution of the microDiamond (2.2 mm) could result in volume averaging in this high dose gradient region, potentially reducing the over-response. The

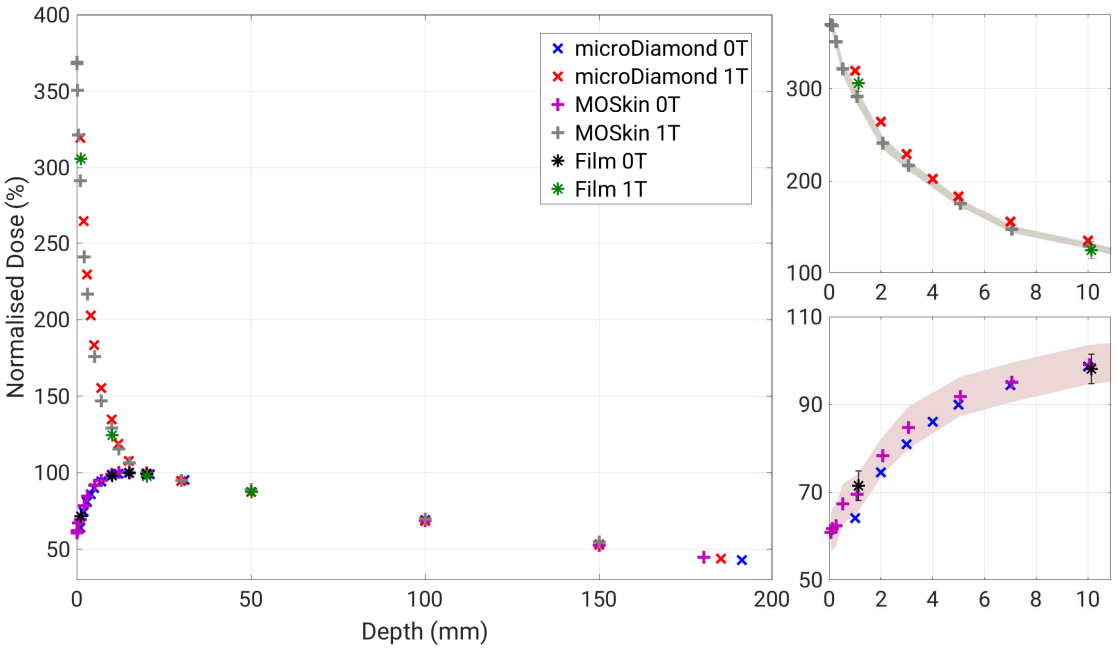

Figure 6.11: Depth dose curves for a 11.8 × 11.5 cm^2 field as measured with microDiamond (×), MO*Skin*^{TM} (+), and EBT3 film (*) in both magnetic field regions. The top right graph is the 1 T near-surface data magnified and the bottom right graph is the near 0 T near-surface data magnified. microDiamond had a maximum uncertainty of 0.1% (near 0 T) and 0.5% (1 T). MO*Skin*^{TM} uncertainties are displayed as shaded error bands.

response of the microDiamond near the surface for the near 0 T data is lower than film and MO*Skin*^{TM}. This difference near the surface compared to other detectors has been observed by previous studies [141, 212].

Skin Dose

Skin dose measurements, with the MO*Skin*^{TM} detector, are shown in table 6.2. These were performed at the two SIDs of 3.269 m (near 0 T) and 1.819 m (1 T). The surface dose for the near 0 T measurements is higher than standard 6 MV linacs, this can be attributed to the extended SSD (1.8 m) and the beam being flattening filter free [213]. It was expected that the relationship between field size and skin dose was linear for the 1 T measurements as more contamination will pass through the MLC opening and there is a larger surface area for MLC contaminant electrons to be produced.

The MO*Skin*^{TM} detector has been previously characterized for measuring skin [201] and build-up dose [202] for standard linear accelerators. In this region it has been shown

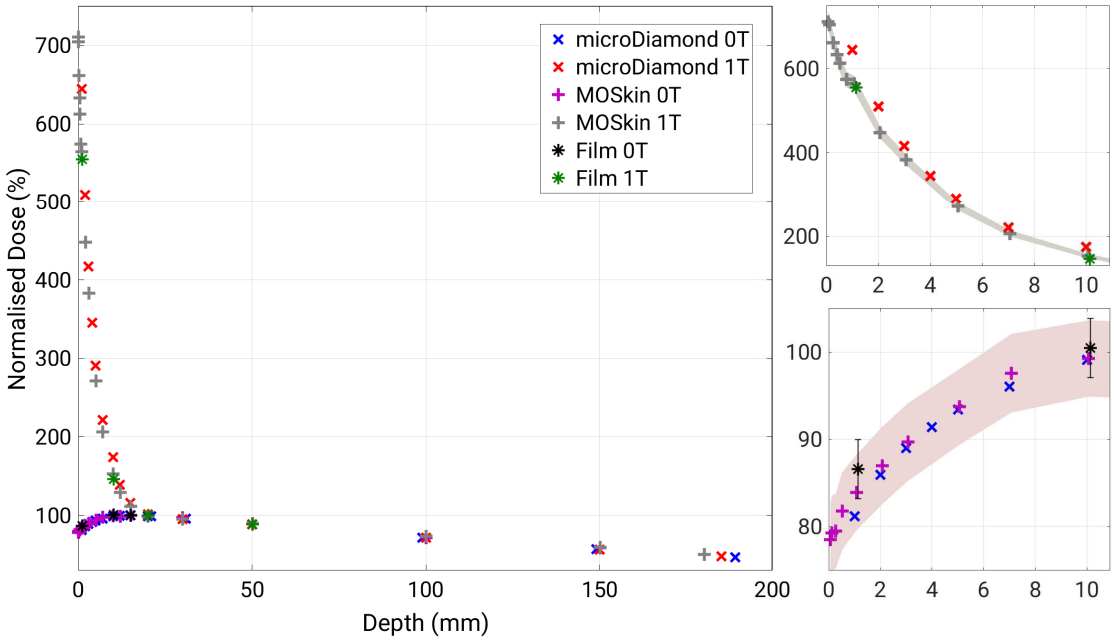

Figure 6.12: Depth dose curves for a 23.5 × 23 cm^2 field as measured with microDiamond (×), MO*Skin*^{TM} (+), and EBT3 film (*) in both magnetic field regions. The top right graph is the 1 T near-surface data magnified and the bottom right graph is the near 0 T near-surface data magnified. Uncertainty in 1 T film at 1,139 mm depth was 6.4% (not visible due to large y-axis range). microDiamond had a maximum uncertainty of 0.2% (near 0 T) and 1.0% (1 T). MO*Skin*^{TM} uncertainties are displayed as shaded error bands.

that electron contaminants have a significant contribution to the dose [214] therefore it is expected that the MO*Skin*^{TM} would give an accurate measure of the dose deposited by the magnetically focused contaminant electrons. Based off simulations which investigated the energy spectra of electrons crossing the surface and up to 5 mm depth in the phantom (see figure 6.13), it is known that low energy electrons (with a peak energy at 100 keV) are depositing dose. Silicon is known to over-respond to low energy (kilovoltage) photons due to the photoelectric effect being dominant for higher Z materials [204] whereas EBT3 has been shown to under-respond at these energies [215]. In this study, the agreement of film and MO*Skin*^{TM} near the surface indicates neither over- or under-respond to the high fluence of electrons.

A previous simulation study by Oborn et. al. [107] predicted high skin dose as a result of the large fringe field of the Australian MRI-linac magnet. The current work was the first experimental measurements of skin dose, defined at 0.07 mm depth, on this system. Oborn et. al. [107] predicted a skin dose of 250% for a 5 × 5 cm^2 field, 550% for a 10 × 10 cm^2 field and 1400% for a 20 × 20 cm^2 field which are higher than

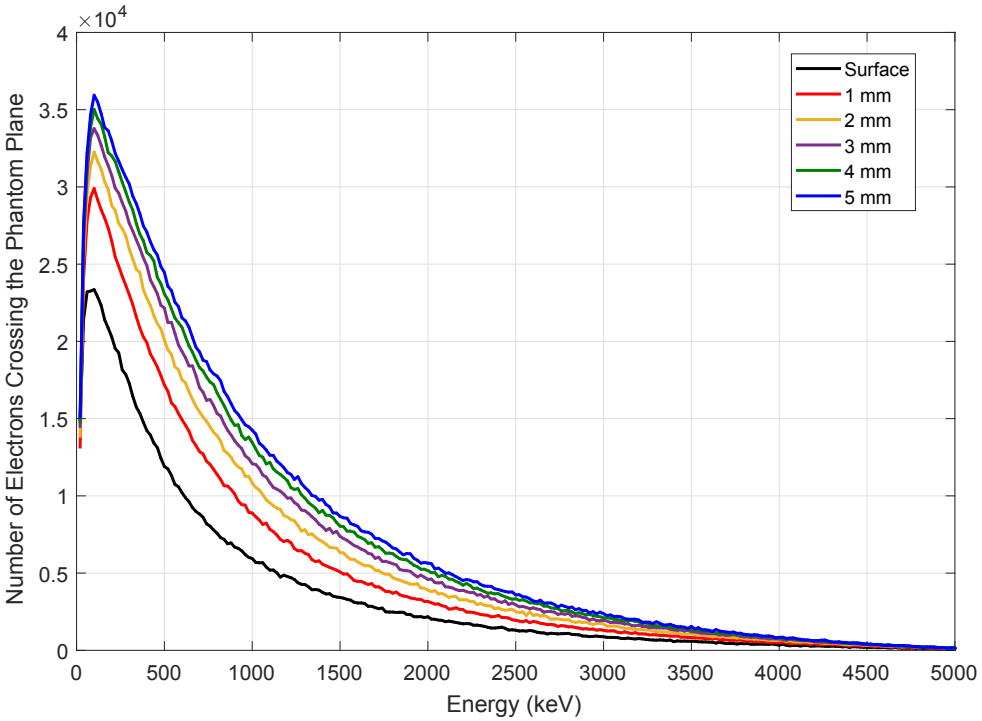

Figure 6.13: Electron energy spectra at different depths in the phantom, obtained from Geant4 simulations. 4×10^{11} electrons hitting the target.

Table 6.2: Skin Dose for field sizes at near 0 T and 1 T, measured with MO*Skin*™ detector. Dose normalised at 50 mm depth, expressed as percentage of maximum dose for near 0 T measurements.

Field Size (cm^2)	near 0 T	1 T
2.1×1.9	44.5%	104.5%
6.1×5.8	47.8%	185.6%
11.8×11.5	60.8%	369.1%
23.5×23	78.5%	711.1%

the values measured with the MO*Skin*™ detector (table 6.2). There are dissimilarities between the simulation and experimental setup which explain these differences. Firstly, the source-to-isocenter distance is shorter by 20 cm in the simulations, since the linac head components are in closer proximity to the fringe field electrons are less likely to naturally diverge and are focused along the magnetic field lines thus the simulation skin dose would be higher. In order to achieve the same field size at the phantom, an increased source-to-isocenter distance would require a smaller field size set by the MLC and

therefore would block more head contamination. The beam modeled in the simulations is a 6 MV Varian 2100C whereas the Australian MRI-linac is a FFF beam which typically leads to less head scatter; the system is also jaw-less which would reduce scatter further. It is also suspected that the magnetic shielding around the target of the linac would contribute to differences in the beam spectrum.

Increased skin dose has been observed with simulations for another inline MRI-linac design, although they observed dose increases in the range of 6%-19% for a 6 MV radiation beam [108]. This group experimentally observed this effect in a low-field electromagnet using a parallel-plate chamber to measure near-surface dose [109]. For the Australian MRI-linac, the location of the linac with respect to the magnet as well as the magnet's strength and footprint leads to significantly higher surface doses as observed in this study. The MO*Skin*^{TM} detector's small sensitive volume was advantageous for measuring the high dose gradient electron contamination region on this system.

Detectors that are commonly used in the clinic for measuring surface dose such as the Attix (GammaX-RMI, Middleton, WI, USA) and Advanced Markus (PTW, Freiburg, Germany) parallel-plate chambers have large sensitive volumes, 1.25 cm and 0.53 cm diameter respectively, for this purpose they are too large and would result in volume averaging. The MO*Skin*^{TM} detector could potentially be used for measuring the increased relative surface dose out of the beam caused by spiralling contaminant electrons reported for perpendicular systems [104] and for measuring increased exit dose on these systems [216–218].

6.4 Conclusion

In this chapter the microDiamond was tested for use in inline magnetic fields as well as one application in the perpendicular orientation. Results indicate that the microDiamond's response needs to be corrected for field sizes smaller than 1.8 cm^2 when used in an inline magnetic field. In order to accurately acquire profiles for small field sizes with the microDiamond it would be beneficial to use a translational stage to increment the detector position since uncertainty in manual positioning was large. The microDiamond proved to be useful for measuring PDDs on the Australian MRI-linac.

However measurements in the first few millimetres depth showed differences from the other dosimeters, likely due to the charged particle fluence at these depths causing an over-response rather than a magnetic field effect.

The high surface dose caused by magnetically focused contaminant electrons on the Australian MRI-linac was measured for a range of field sizes. The extremely high dose gradient and electronic disequilibrium conditions of this region pose challenges to dosimetry. The MO*Skin*^{TM} was advantageous for obtaining high resolution data to characterize the effect. The relative response of the microDiamond and MO*Skin*^{TM} detectors, beyond the electron contamination region, were shown to be unaffected by the 1 T inline magnetic field since there was agreement between measurements at near 0 T and 1 T and both agreed with film within uncertainty.

Future work will involve using these detectors while testing methods to remove the high electron contamination region from the primary beam in order to obtain a clinically useful beam. Treating off-axis has been shown to separate the photon and electron components [90] as the electrons remain at isocentre, removing them from the intended delivery. A simpler approach, which has been used for first rat treatments on the system [219], is to place a beam spoiler in front of the treatment beam however this brings D_{max} to the surface. Some other methods have been previously simulated i.e. purging the electrons at the level of the MLC and placing a helium gas region between the linac and patient in order to reduce the interactions which occur in the air column [107]. These methods offer the benefit that they remove the electrons which are causing the hot spot rather then absorbing them along with the primary beam. This would also mean the patient could be treated in the center of the magnet where image quality is highest.

Chapter 7

Experimental Measurements of Radiation Beam Data for an Inline MRI-linac

Some of the results presented in this chapter have been published in the Journal of Physics: Conference Series.

N. Roberts, B. Oborn, U. Jelen, B. Dong, J. Begg, A. George, S. J. Alnaghy, T. Causer, T. Alharthi, L. Holloway, P. Metcalfe, "Modelling the x-ray source for the Australian MRI-Linac", J. Phys: Conf. Ser. 1154, p. 012025, 2019.

Some of the methods presented in this chapter have been published in the Frontiers in Oncology.

U. Jelen, B. Dong, J. Begg, N. Roberts, B. Whelan, P. Keall, G. Liney, 2020. "Dosimetric optimization and commissioning of a high field inline MRI-linac", Front. Oncol., 10:136.

7.1 Overview

Commissioning a radiotherapy machine is an important step to ensure safe patient treatments. The process to commission clinical linear accelerators is quite detailed and time consuming [37]. MRI-linac radiation beam commissioning proves to be a further challenge because of the limitations in equipment which can be used in the presence of a magnetic field and therefore requires adaptation of standard methods. There are currently

no published guidelines for radiation beam commissioning for MRI-guided radiotherapy, although many centres have described methods to acquire (or what to avoid when acquiring) accurate beam data [139, 220–222]. Further, inline systems have different considerations to those published (for perpendicular systems) owing to differences in their design.

Collection of radiation beam data for the Australian MRI-linac system is detailed here. The proximity of the treatment machine to the imaging machine, or SID, can be varied as described in section 6.2.3. This chapter describes the acquisition of beam data measurements at three different SIDs. The measured data was intended for the development of both a convolution-based TPS and Monte Carlo beam models as are described in chapter 8. The recommendations of AAPM Task Group 106 [37] were followed to characterise the beam with any limitations of the measurements described throughout.

7.2 Materials and Methods

7.2.1 MRI-linac

The Australian MRI-linac was previously described in chapter 6. The 1 T measurements presented in this chapter were for three SIDs of 2.869 m, 2.469 m and 1.819 m. The first distance was, at the time, intended to be used for patient treatments however it became possible to treat at a closer distance by placing shielding around the linac target. Prior to shielding, it was hypothesised that the magnetic field was causing the electron beam to bend and therefore not hitting the target orthogonally. Shielding the target resulted in higher output and lead to profile symmetry passing IEC60976/ criteria [206, 206] for the SID 2.469 m and a subset of field sizes at 1.819 m. To resolve the problem of high electron contamination at the surface (observed in chapter 6), a 2 cm thick beam spoiler was placed 5 cm in front of the phantom. This was performed for all data collected at SIDs 2.469 m and 1.819 m for PDDs and profiles. PDDs were also measured without a beam spoiler for these SIDs to allow for finer tuning of the magnetic field map used for the Monte Carlo model.

Table 7.1 gives the field sizes measured for the 1 T setup for the different SIDs. Many procedures outlined in AAPM Task Group 106 [37] were not applicable to this system including tray and wedge factors and electron beam measurements. With the system being jaw-less, the measurements required for TPS modelling were further reduced. For all field sizes the closed MLC leaves were placed off axis so that dose from leaf end transmission was not measured on the film. Near 0 T measurements were performed with the linac at 3.269 m from isocentre and the phantom at SSD 0.743 m, the field size for this dataset was 9.0×8.8 cm^2.

7.2.2 Film Dosimetry

Gafchromic® EBT3 film was used to measure percentage depth dose curves and profiles of the radiation beam. A standard scanning water tank was not used due to incompatibility with the magnetic field and size restrictions of the system. Film was chosen for these measurements as previous studies have shown the effects of the magnetic field on the relative response is negligible [151, 170], as well as having a high spatial resolution and near tissue equivalence. The dosimeter was placed within a solid water phantom as shown in figure 7.1. For measurements with the film parallel to the beam i.e. PDDs, the film was aligned to the edge of the phantom by placing a slab in front during setup and ensuring the film edge was straight with the surface. Pressure was applied from the solid water slabs placed on top of film therefore minimising air gaps [223]. It was also suspected that the phantom would have been slightly tilted due to the weight on the board it was placed on and therefore the film would be at an angle to the beam which is recommended for parallel films [224]. Tests were performed by purposely introducing air gaps into the phantom and observing the resulting artefacts, such artefacts were not seen in the PDD data presented here.

The guidelines outlined in AAPM Task Group 55 [205] for using radiochromic film for dosimetry were followed. An EPSON V700 flatbed scanner (Seiko Epson Corp, Nagano, Japan) was used to scan film before and after irradiation, orientation was kept consistent as were scanning parameters. The scanning resolution was 72 dpi with a format of 48-bit RGB and colour corrections were turn turned off. A black paper template was placed on the scanning bed to consistently position the film reducing uncertainties in scanner

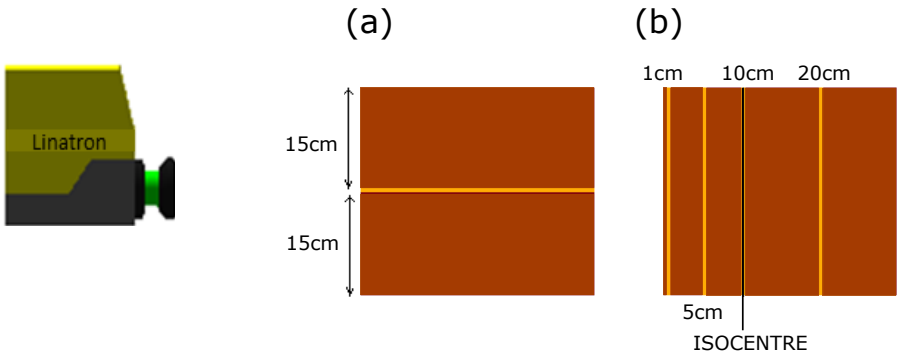

Figure 7.1: Setup of measurements with radiation beam (linatron) direction from the left and solid water phantom with film placed for (a) percentage depth dose curves and (b) profiles. Side-on view. Linatron not to scale.

uniformity. All analysis was performed using MATLAB®, taking the red channel from the scans.

Following conversion of optical density to absolute dose, PDD curves were acquired from the 2D dose distributions by creating a 10 pixels wide region of interest (in the direction perpendicular to the CAX) and then calculating median dose across the 10 pixels. This resulted in reduced noise from fluctuations in the data while maintaining the high dose gradient on films that included the high electron contamination region. PDD depths were defined by using marks at 10 cm depth on the film. Beam profiles were taken by a line profile through the laser marks, for X profiles this method was preferred since the field edge (defined by leaf-ends) would be blurred when taking a region of interest. The profiles were centred based off the lasers marked in the alternate profile direction. All data presented in this chapter was normalised to 5 cm depth.

7.2.3 STARCHECK$^{MAXI\ MR}$ Dosimeter

The STARCHECK$^{MAXI\ MR}$ (PTW Freiburg, Germany) is an ionisation chamber 2D array that is MRI compatible, safe for use up to 1.5 T. It consists of 707 air-vented ionisation chambers with 3 mm spacing, the chambers are $2.5 \times 8.0 \times 2.5$ mm^3. The array has been characterized on the Australian MRI-linac [225] based on IEC60731 standards [226]. Profiles of the field sizes listed in table 7.1 for an SID of 2.869 m were acquired to validate film dosimetry methods at 1 T. The STARCHECK$^{MAXI\ MR}$ was placed at an effective depth of 10 cm (solid water) for all fields.

Table 7.1: Summary of data collected at different source-to-MRI-isocentre positions. FS = Field Size.

Nominal FS	Source to MRI Isocentre Distance		
x × y (cm^2)	2.869 m [FS at Phantom (cm^2)]	2.469 m [FS at Phantom (cm^2)]	1.819 m [FS at Phantom (cm^2)]
1 × 1	3.6 × 3.1	3.2 × 2.6	2.2 × 1.9
2 × 2	6.7 × 5.9	5.8 × 5.1	4.2 × 3.8
3 × 3	9.9 × 9.3	8.4 × 7.9	6.1 × 5.8
4 × 4	13.0 × 12.1	11.0 × 10.3	8.0 × 7.7
5 × 5	16.2 × 15.5	13.7 × 13.2	10.1 × 9.7
6 × 6	-	16.3 × 15.6	11.8 × 11.5
7 × 7	-	18.8 × 18.4	13.9 × 13.5
8 × 8	-	-	15.8 × 15.3
9 × 9	-	-	17.8 × 17.4
6 × 2	19.3 × 5.9	-	-
2 × 6	6.7 × 18.4	-	-
7 × 2	-	18.8 × 5.1	-
2 × 7	-	5.8 × 18.4	-
9 × 3	-	-	17.8 × 5.8
3 × 9	-	-	6.1 × 17.4

7.2.4 CC13 Ionisation Chamber

The CC13 Ionisation Chamber (IBA Dosimetry GmbH, Schwarzenbruck, Germany) is commonly used clinically for PDD measurements and therefore was used to verify film measured PDDs. The chamber was positioned vertically in solid water and the chamber holder was filled with water to avoid air gaps. The dose was measured at select depths (beyond the electron contamination region near the surface) and normalised to the response at 5 cm depth. The data for SID of 2.469 m for a nominal field size 7 × 7 cm^2 is included.

7.3 Results and Discussion

7.3.1 0 T measurements

Figure 7.2(a) shows the PDD for the 9.0 × 8.8 cm^2 field size measured outside the magnetic field. D_{max} was calculated to be 1.4 ± 0.1 cm for this shorter SSD, this uncertainty in depth arises from determining which pixel is 0 cm in the film scans. These measurements were performed for the purposes of Monte Carlo 0 T beam modelling, when the phantom is closer to the source the electron beam modelling parameters become more sensitive to variations and therefore a precise model can be developed. Water tank measurements acquired prior to the installation of the MRI were measured at SSDs comparable to the distances which would be used for treatments on the Australian MRI-linac. These 0 T measurements are included in chapter 8 to compare with the beam models in both Pinnacle[3] and Monte Carlo. Figure 7.2(b) shows wider X profiles than the Y profiles due to the fields being MLC defined and therefore transmission through the leaf ends results in the larger penumbra for the X profiles. This becomes more pronounced when moving to extended SSDs, as seen by observing field sizes at the phantom for different SIDs in table 7.1.

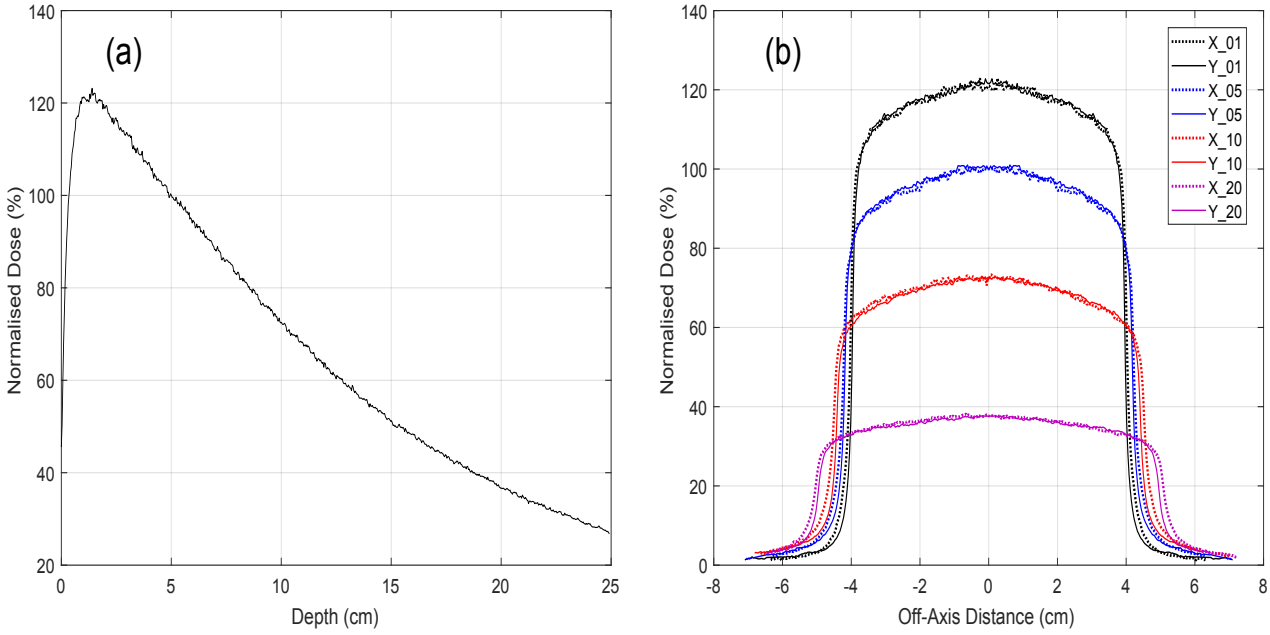

Figure 7.2: EBT3 film measurements outside of the magnetic field for a 9.0 × 8.8 cm^2 at SSD 0.743 m. (a) PDD and (b) profiles at different depths. Legend in (b) specifies X/Y profile and the depth (cm) of the profile. Error in film measurements is ± 4%.

7.3.2 1 T measurements

The high electron contamination dose at the surface, caused by fringe field electron focusing, was characterised in chapter 6. This effect is evident in PDDs for SID 2.869 m shown in figure 7.3, the surface dose increases with field size. These contaminant electrons are absorbed by a depth of 20 mm into the phantom however they travel beyond D_{max} therefore dose was normalised at 5 cm depth. Note that the maximum dose was not at the surface rather it falls somewhere between 0-1 mm, this was observed with MO*Skin*^{TM} measurements in chapter 6. Using this data for modelling in the TPS proved to be challenging; electron contamination modelling in Pinnacle^3 was not capable of producing this sort of PDD. Initially it was considered to separate the components by using two models, one for the photon beam dose and one for the electron beam dose and when calculating the dose for a treatment plan, the two models could be summed together. However it was decided to collect beam data with a beam spoiler in place, primarily to remove the high surface dose for patient treatments but also to observe if this made modelling the beam in Pinnacle^3 more feasible.

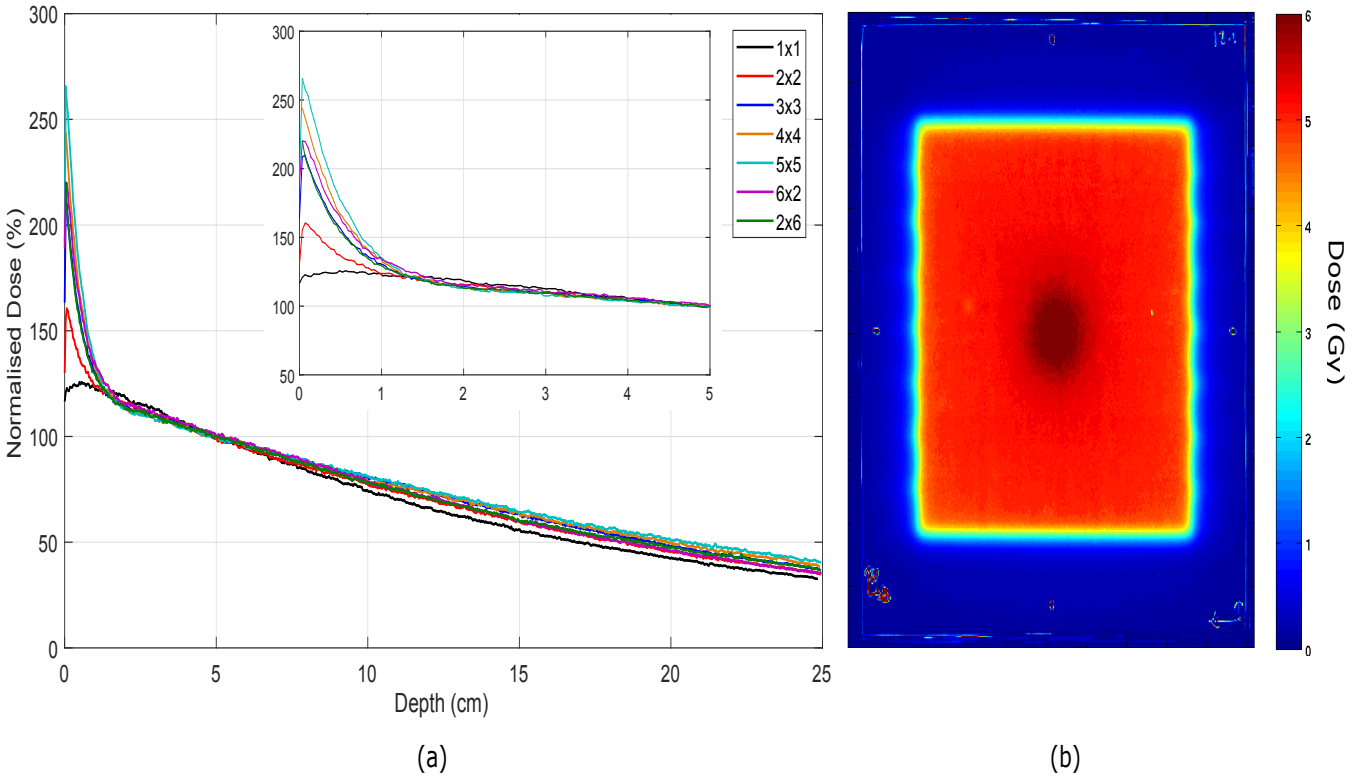

Figure 7.3: (a) PDDs for all fields sizes without a beam spoiler measured with EBT3 film at SID of 2.869 m. (b) A 2D dose distribution of the 4 x 4 cm^2 field at 1 cm depth.

In the profiles at depth 1 cm in figures 7.4-7.6 the electron contamination region is also visible; for this SID (2.869 m) it appears to be approximately 4 cm in diameter (note at 1 cm depth) in the off-axis plane. In order to verify the film dosimetry methods were accurate, measurements were taken with STARCHECK$^{MAXI\ MR}$ and are shown on the right hand side of figures 7.4-7.6 compared with film at 10 cm depth. It should be noted that the resolution of the STARCHECK$^{MAXI\ MR}$ is 3 mm whereas film is 0.35 mm and therefore differences are seen in the penumbra between measurements. For the 5×5 cm^2 in figure 7.5b the film profile is asymmetric, also observed in figure 7.6b, this was likely due to the fact that the film was not flat between the solid water pieces i.e. it would bow, this was difficult to avoid when positioning the slabs and film vertically. To minimise this, a dedicated stand was manufactured to hold the solid water tightly together. The data obtained at 2.869 m from the source was not used for beam modelling however was useful in critiquing the methods for future measurements at closer SIDs.

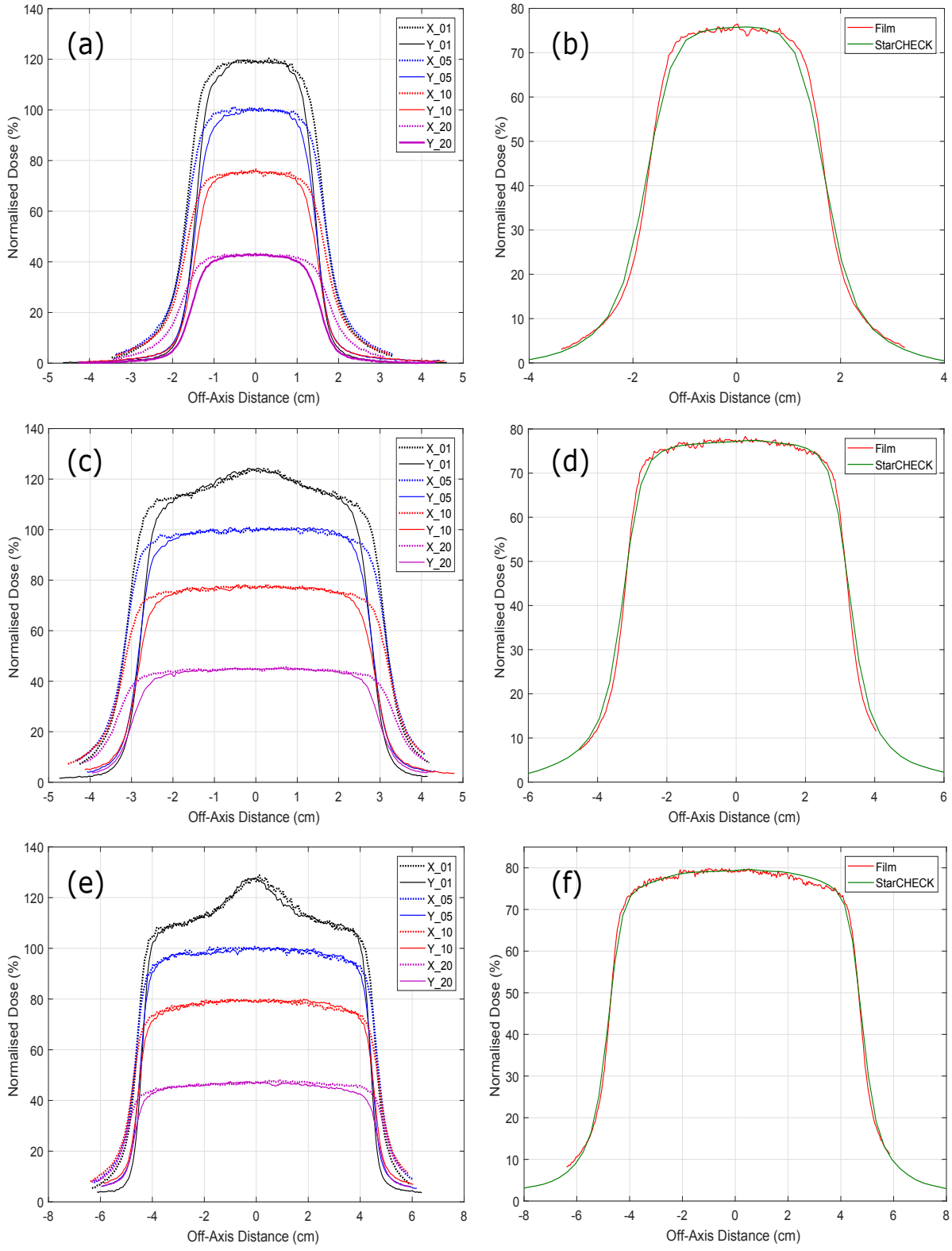

Figure 7.4: Profiles measured with film (a,c,e) for varying depths (given in cm in legend) and X profiles at depth 10 cm comparing film to STARCHECK$^{MAXI\ MR}$ (b,d,f). The nominal field sizes are (a-b) 1×1 cm^2, (c-d) 2×2 cm^2, (e-f) 3×3 cm^2. SID of 2.869 m, without a beam spoiler.

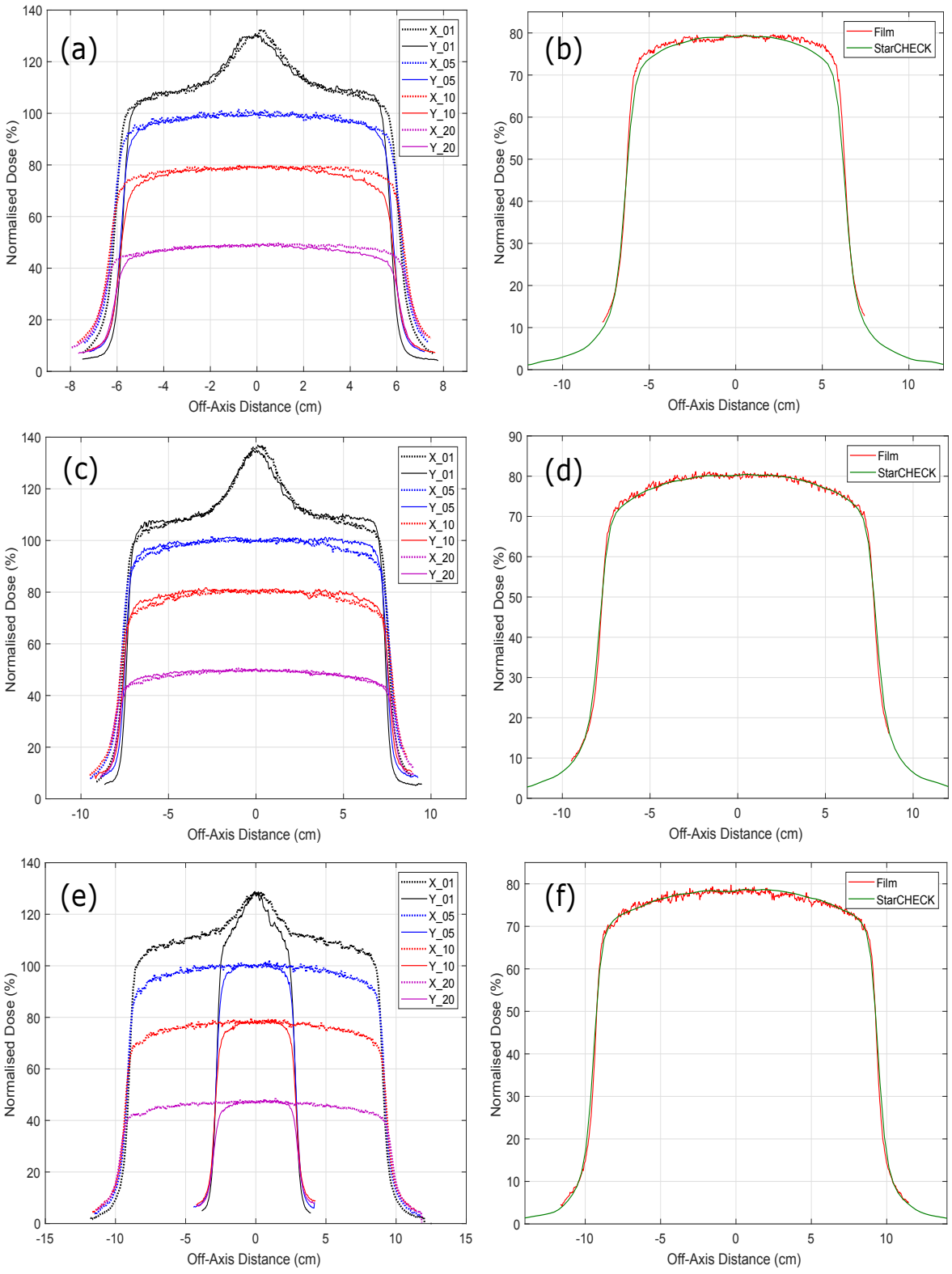

Figure 7.5: Profiles measured with film (a,c,e) for varying depths (given in cm in legend) and X profiles at depth 10 cm comparing film to STARCHECK$^{MAXI\ MR}$ (b,d,f). The nominal field sizes are (a-b) 4×4 cm^2, (c-d) 5×5 cm^2, (e-f) 6×2 cm^2. SID of 2.869 m, without a beam spoiler.

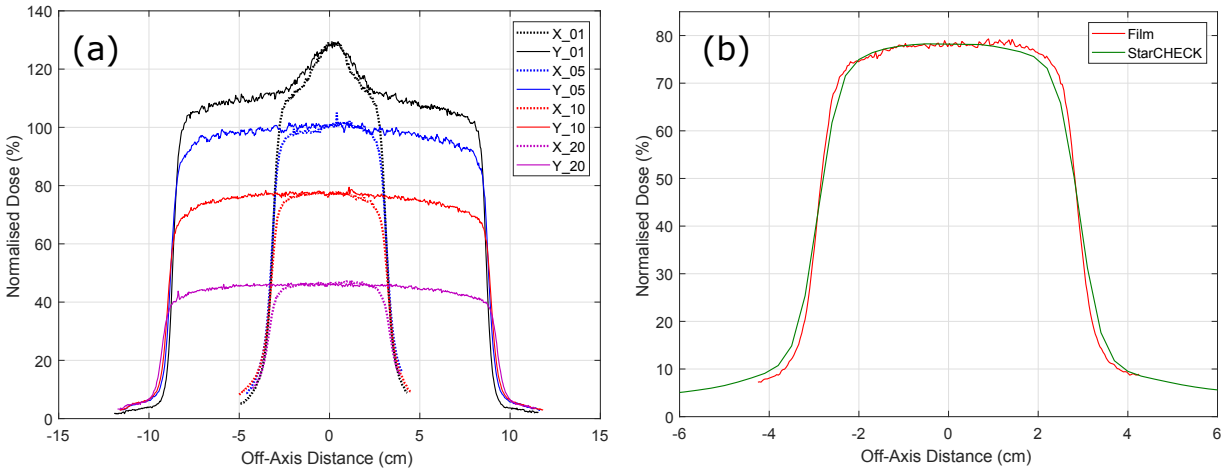

Figure 7.6: Profiles measured with film (a) for varying depths (given in cm in legend) and X profiles at depth 10 cm comparing film to STARCHECK$^{MAXI\ MR}$ (b). The nominal field size was 2×6 cm^2. SID of 2.869 m, without a beam spoiler.

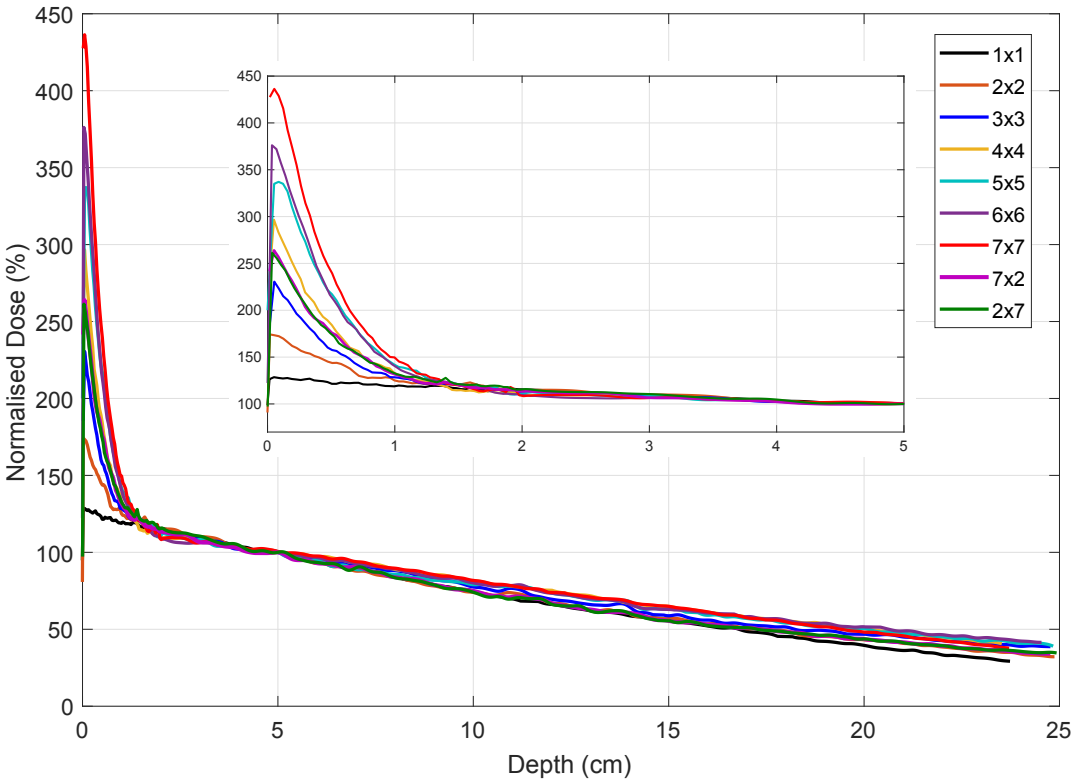

Figure 7.7: PDDs for all fields sizes without a beam spoiler measured with EBT3 film at SID of 2.469 m.

PDDs measured at an SID of 2.469 m without a beam spoiler are shown in figure 7.7. Similarly to the previous SID, the trend of increasing surface dose with increasing field size was observed. The depth at which D_{max} occurs within the first 1 mm for all field

sizes however there is a large uncertainty of dose and depth near the surface therefore no conclusions can be drawn on trends related to field size.

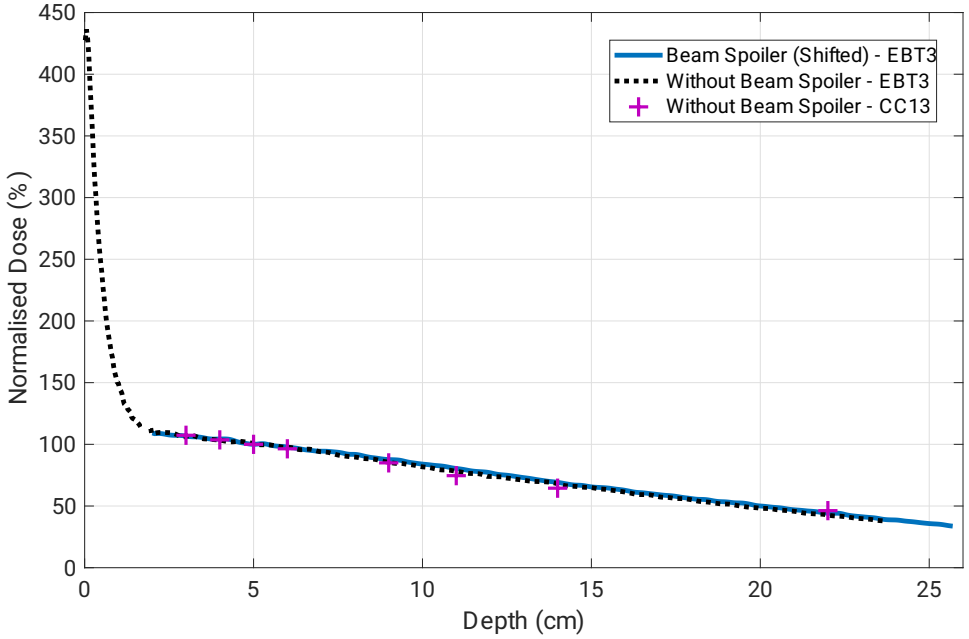

Figure 7.8: PDDs for nominal field size 7 $\times$ 7 cm^2 with and without a beam spoiler measured with EBT3 film and CC13 at SID of 2.469 m. PDD with a beam spoiler was shifted by 2 cm to align with the PDD without a beam spoiler. Note that some data was removed at depths as marks on the film were placed to indicate the lasers and therefore produced spikes in the PDD.

For PDDs with a 2 cm beam spoiler in front of the phantom it was expected that by shifting the curves to 2 cm depth the PDDs should align with the same field size PDD without a beam spoiler. An example of two PDD curves compared is shown in figure 7.8 for a nominal field size of 7 $\times$ 7 cm^2 (the largest field measured for SID of 2.469 m). Figure 7.8 also includes the PDD measured with a CC13 ion chamber, this data verifies the methods of acquiring PDD data with film. Note that data was removed at some depths as this was where marks on the film were placed to indicate the lasers.

Profiles acquired for an SID of 2.469 m are displayed in figures 7.9. The processing of the data involved removing laser mark artefacts, smoothing using a moving average function, centring and symmetrising profiles. Overall, profile symmetry (as measured on the films) was improved when using the dedicated stand to reduce gaps in the vertical solid water phantom.

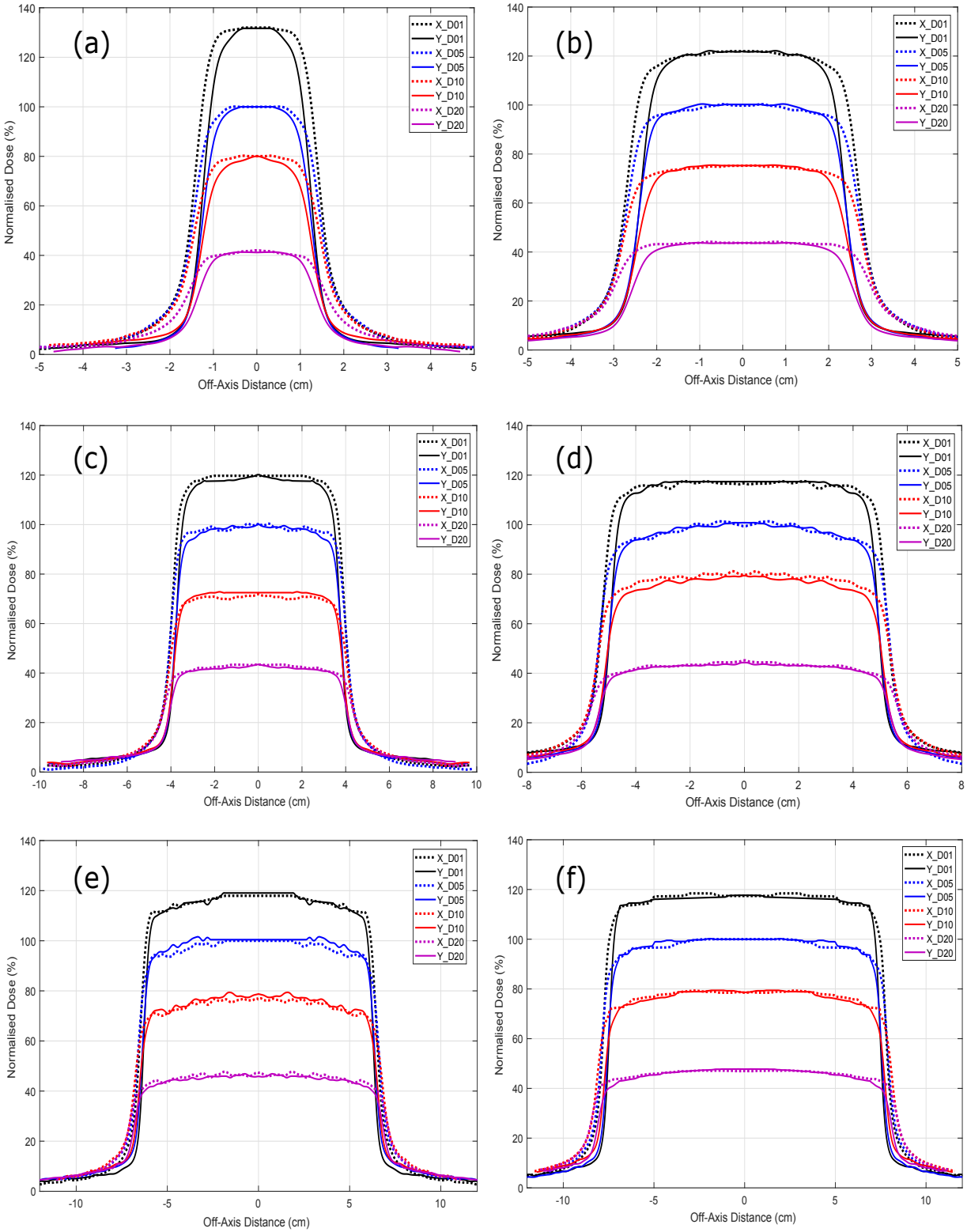

Figure 7.9: Profiles measured with film for varying depths (given in cm in legend). The nominal field sizes are (a) 1×1 cm^2, (b) 2×2 cm^2, (c) 3×3 cm^2, (d) 4×4 cm^2, (e) 5×5 cm^2 and (f) 6×6 cm^2. SID of 2.469 m, a 2cm beam spoiler was placed 5 cm in front of phantom.

A range of measurements were performed for an SID of 1.819 m however for brevity

only PDDs are included. All PDDs without a beam spoiler are shown in figure 7.10 and a comparison of the PDDs with and without a beam spoiler for a nominal field size of 9×9 cm^2 is shown in figure 7.11.

The maximum doses for PDDs (without a beam spoiler) can be compared for film measurements in this chapter and MO*Skin*^{TM} measurements from chapter 6. With the data expressed as dose normalised at 5 cm depth (note this is different to how it is expressed in table 6.2), a maximum dose of 131% from film and 128.8% from MO*Skin*^{TM} was measured for a 1×1 cm^2 nominal field size. For a 6×6 cm^2 nominal field the PDD film maximum dose was 409.7% and for MO*Skin*^{TM} was 414.2%. It was noted that the PDDs measured with MO*Skin*^{TM} and parallel film did not agree within the first 2 cm of the phantom, this could be the result of two factors: the uncertainty in film depth and an over-response of film to the low energy electrons due to its parallel orientation. The range of these very low energy electrons (energy spectra shown in figure 6.13) could be decreased when traversing through film, as opposed to water, therefore resulting in an over-response. For measurements of the high electron contamination region on the Australian MRI-linac, using film in the parallel orientation to obtain PDDs appears not as accurate as solid state detectors, since PDDs obtained with these detectors agreed with each other and film orientated perpendicular to the beam. In the case of measurements where the electron contamination has been removed, by placing a beam spoiler in front, the PDD films, once aligned, agree with the MO*Skin*^{TM} and microDiamond measurements from chapter 6 as well as the measurements without a beam spoiler (figure 7.8).

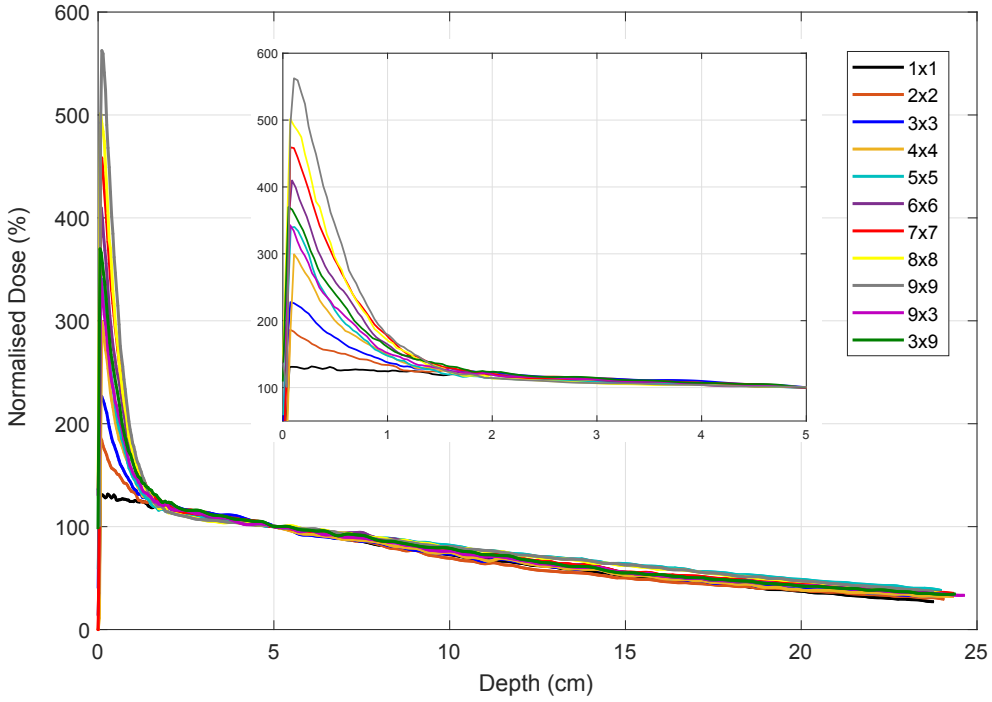

Figure 7.10: PDDs for all fields sizes without a beam spoiler measured with EBT3 film at SID of 1.819 m.

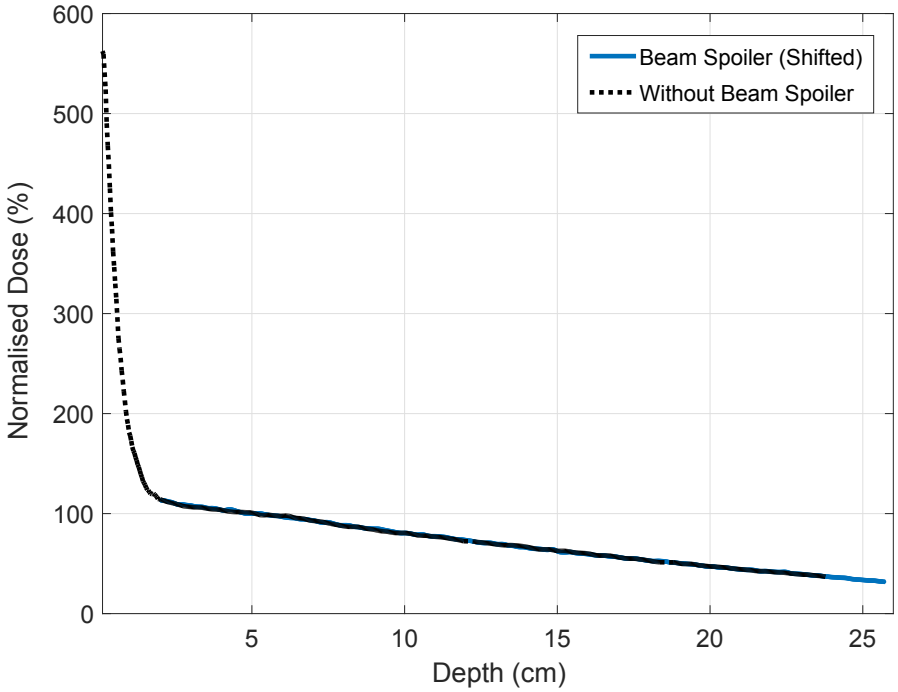

Figure 7.11: PDDs for nominal field size 9 $\times$ 9 cm^2 with and without a beam spoiler measured with EBT3 film at SID of 1.819 m. PDD with a beam spoiler was shifted by 2 cm to align with the PDD without a beam spoiler. Note that some data was removed at depths as marks on the film were placed to indicate the lasers and therefore produced spikes in the PDD.

7.3.3 Near Surface Dose as function of SID

Figure 7.12 shows the near surface maximum dose as a function of field size for the three different SIDs investigated. The trend of increasing surface dose as a function of SID was observed. The fringe field as measured with a gauss meter at the MLC were 0.008 T, 0.02 T and 0.05 T for SID 2.849 m, 2.469 m and 1.819 m respectively. These results show that the magnitude of the high electron contamination region is dependent on the proximity of the linac components (particularly the MLC) to the MRI and importantly its fringe field. Note that for the furthest SID the curve plateaus at larger field size.

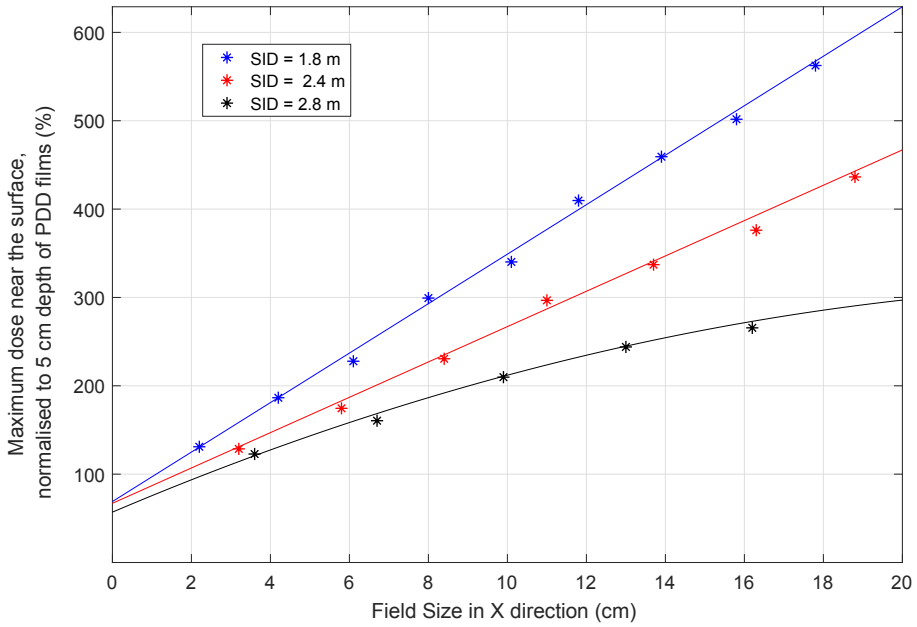

Figure 7.12: Measure of the maximum dose near the surface for PDDs without a beam spoiler as measured with EBT3 film for all approximately square field sizes.

7.4 Conclusion

Methods were developed to acquire radiation data to be used for beam modelling for an inline MRI-linac system. The initial data obtained (SID of 2.849 m) yielded asymmetric profiles due to air gaps between solid water slabs therefore a stand was manufactured to hold the solid water tightly together. TPS beam modelling was challenging with the high electron contamination present therefore it was decided to remove the contamination (by absorption) with a beam spoiler and use this beam data for TPS modelling.

Due to this high electron contamination region, acquiring PDDs with film parallel to the radiation beam proved to be problematic. This method was not as accurate as those described in chapter 6. However using a beam spoiler and thus removing the electron contamination, measurements could be performed in this way for beam modelling data.

Electron contamination at the surface increased with increasing field size, the same trend was observed as in chapter 6. Measurements performed at the 3 different SIDs showed that the electron contamination was also highly dependent on the proximity of the linac components to the MRI and importantly its fringe field. The beam data collected

at SIDs of 2.469 m and 1.819 m with a beam spoiler in place were sufficient for beam modelling.

Chapter 8

Treatment Beam Model Commissioning for an Inline MRI-linac

Some of the results presented in this chapter have been published in the Journal of Physics: Conference Series.

N. Roberts, B. Oborn, U. Jelen, B. Dong, J. Begg, A. George, S. J. Alnaghy, T. Causer, T. Alharthi, L. Holloway, P. Metcalfe, "Modelling the x-ray source for the Australian MRI-Linac", J. Phys: Conf. Ser. 1154, p. 012025, 2019.

8.1 Overview

As a prerequisite for patient treatments, a radiation beam model must be developed in the treatment planning system in order to generate patient plans. For MRI-guided radiotherapy, treatment planning and dose calculations should include any significant effects the magnetic field has on beam characteristics consequently reducing deviations between planned and delivered dose. Current commercial TPSs are not capable of modelling the complete magnetic field, including the fringe field. Begg et al. [164] have shown that beyond the electron contamination region of the Australian MRI-linac, the relative dose deposition in water along the central axis remained unchanged with different inline magnetic fields strength. Although there are small changes to penumbral widths in water, these changes could be modelled in the TPS. Therefore, it is expected that a convolution-based TPS system should be able to model an inline MRI-linac if the magnetically focussed electron contaminants are removed. Differences in lung tissue

will be more significant than water [113] and therefore will need to be closely assessed. To verify deviations caused by the magnetic field are minimal the Australian MRI-linac program has proposed a Monte Carlo dose verification system to calculate dose with and without the magnetic field. This chapter describes the development of a beam model with Geant4 (Monte Carlo) and Pinnacle^3 (TPS).

8.2 Materials and Methods

8.2.1 Geant4 Model

The Monte Carlo toolkit, Geant4 [166] version 10.5 was used to model the beam. The physics processes modelled were compton scattering, photoelectric effect, pair production, gamma conversion, bremsstrahlung, multiple scattering, ionisation and annihilation. The range cuts were set to 0.1 mm for all particles and a step limit of 1 mm. The simulations were two stages: an electron beam hitting the target and scoring all particles in a phasespace that cross a plane before the MLC, in the second stage the particles pass through the MLC and dose deposited inside the phantoms was stored. The number of electrons hitting the target were 4×10^{10} and particles were recycled 49 times in stage 2 of the simulations. Geometry and materials for the model were based upon manufacturer specifications and physical measurements of some components. The linear accelerator model includes a tungsten target, a primary collimator, a monitor chamber as well as the housing of the accelerator. The dose deposited in the phantoms was scored with voxel size of $2 \times 2 \times 2$ mm^3, unless otherwise specified.

Electron beam parameters were varied in order to obtain a match between the simulation results and measurements. The parameters optimised were mean energy, FWHM of the energy distribution and focal spot size. The target density was also varied to observe the effect this had upon beam profiles. To determine a parameter the others were kept fixed. These fixed values were 6.0 MeV for mean energy, 0.2 MeV for the FWHM of the energy spread and a Gaussian spatial distribution of 1.3 mm in the x and y direction. The tungsten target density was 19.3 g/cm^3.

For simulations which included the magnetic field delta one step was set to 10 μm, delta

intersection was 1 μm and the miss distance set to 25 μm. A 3D magnetic field map was generated using COMSOL Multiphysics (Stockholm, Sweden) software with a finite element method. The magnetic field component in each direction was stored in a lookup table which was read in to the simulations.

Measurements for comparison with modelling data were acquired with different detectors/dosimeters dependent on the application. 0 T measurements which were used for Monte Carlo modelling were obtained at an SSD of 164 mm so to fine tune electron beam parameters. Whereas for 1 T measurements included those collected at the MRI isocentre both with and without beam spoiler in place.

8.2.2 Pinnacle^3 Model

The TPS model was developed in Pinnacle^3 (Philips Healthcare, Fitchburg, WI, USA). When adding a new machine in the physics module, physical machine characteristics must be included; these are settings for the jaw, couch, collimator, gantry, delivery and other compensators/collimators. Since many of these components are non-existent on the Australian MRI-linac system or can not be varied they were set to default values. For example the gantry angle was set to 90° and the jaws were fixed to a 40 $\times$ 40 cm^2 field. The main machine characteristics of interest were the primary collimator angle (0.1572 rad) and the MLC settings. The projected width of leaves at isocentre was varied based on measurements of field size at isocentre. At the SID of 2.469 m the projected width of the inner leaves were 1.3 and the outer leaves were 2.6. The MLC-to-source distance was calculated based off these projections and set to 50.6 cm (typically this value for a Varian linac is 53.9 cm).

Experimental data presented in chapter 7 was converted to the appropriate ASCII file format and imported into the software. Firstly, the phantom size was set to match experiments and a grid resolution of 0.4 cm was used; this was later decreased to 0.2 cm when fine tuning the model.

The process for photon beam modelling allows for variation of the energy spectrum, to determine the shape of the PDD, and electron contamination, to determine the build-up

region of the depth dose curve [227]. The energy spectrum was expected to have a high low-energy component as it is a FFF beam. The electron contamination model in Pinnacle^3 is defined as a function of depth, off axis distance and field size. Exactly how each parameter contributes to the dose is given in figure 8.1, which is taken from the Pinnacle^3 software [228].

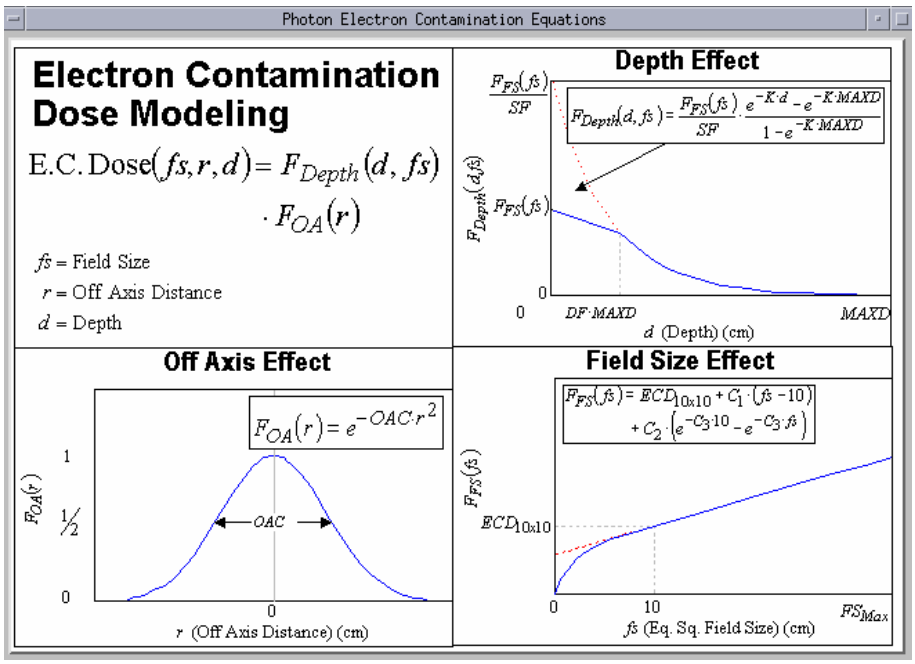

Figure 8.1: The electron contamination equations used in Pinnacle^3 [228], screenshot taken from the software.

To change profile shape, parameters which determine in field and out of field dose can be modified. In field model parameters include flattening filter attenuation and spectral off-axis softening [229]. An arbitrary profile was used to model flattening filter attenuation as this is typical for FFF beams [230]. Out of field parameters include effective source size which is modelled by a Gaussian, the parameters (in directions X and Y) influence the penumbra of profiles. While profile tails are determined by scatter contributions from the flattening filter and jaw/MLC transmission.

A 0 T model was included here as it was used as a building block for the 1 T model. 0 T open field measured data was collected in a water tank prior to the MRI being installed (measurements courtesy of J. Begg). Pinnacle^3 beam modelling, intended to be used for patient planning, requires a full set of beam data therefore the measured data collected at isocentre with SID of 2.469 m was used for the 1 T model. The high skin

dose of the Australian MRI-linac, discussed in chapter 6, was in the first instance to be removed with a beam spoiler. The measured data imported into Pinnacle^3 was therefore the data collected with a beam spoiler in place.

Output factors were entered into the 1 T model from measurements performed during commissioning. These were measured with farmer chamber and microDiamond, the microDiamond was required for the smallest field as the ion chamber was underestimating the output. Detectors were placed at 10 cm depth in the phantom, located at isocentre, and measurements were acquired for all field sizes and normalised to the $\approx 10 \times 10$ cm^2 field for that SID. Note that an exact 10×10 cm^2 field is not achievable as leaf projections in the Y direction are determined by MLC width in that plane.

8.3 Results and Discussion

8.3.1 Geant4 Model

0 T

Varying the electron mean energy results in changes to the PDD as this will effect the photon energy spectrum and thus the range of the electrons that deposit dose in the patient/phantom. The left graph of figure 8.2 shows simulated PDDs with different electron mean energies compared to the PDD measured with microDiamond. An SSD of 164 mm was used for this setup as the dose curves are more sensitive to changes in electron beam parameters when the phantom is closer to the source therefore a more precise model can be obtained. All simulated depth dose curves agree beyond the build-up region although differences can be seen around D_{max}, the closest match for this region was a mean energy of 6.0 MeV.

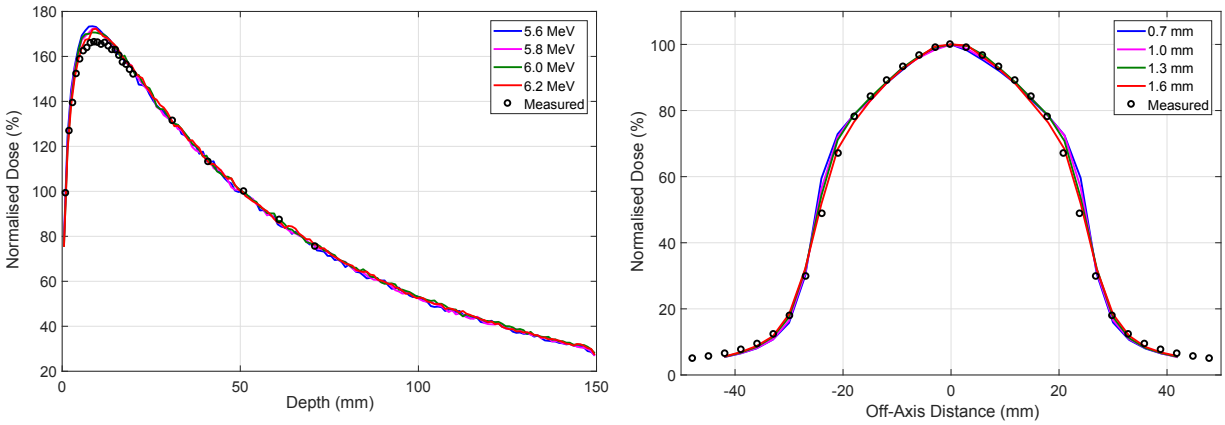

Figure 8.2: Monte Carlo (—) and measured (o) PDD (left) and profile (right) data. Comparing variations of initial mean electron energy (left) and focal spot size (right). Measurements were acquired with microDiamond (PDD) and STARCHECK$^{MAXI\ MR}$ (Profiles) at SSD = 164 mm, 0 T conditions.

The focal spot size of the electron beam hitting the target effects the penumbral width of profiles therefore these are compared in figure 8.2 in the graph on the right. The closest match to measured data was for a 1.6 mm focal spot size.

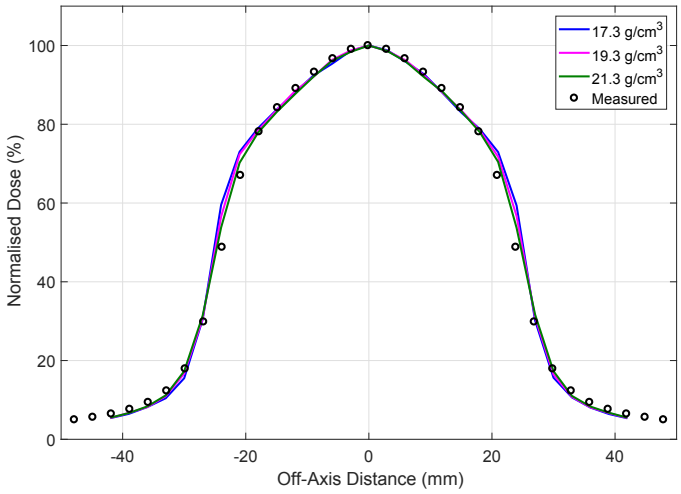

Figure 8.3: Monte Carlo (—) and measured (o) profile data. Comparing variations of the tungsten target density. Measurements were acquired with STARCHECK$^{MAXI\ MR}$ at SSD = 164 mm, 0 T conditions.

Changing the density of the target should have greater impact on the dose profiles [231] and therefore these are shown in figure 8.3 for different simulated target densities. A density of 21.3 g/cm^3 was shown to have the nearest agreement with measured profiles. The optimised parameters were mean energy of 6.0 MeV (FWHM of 0.2 MeV), focal spot size of 1.6 mm and target density of 21.3 g/cm^3. Comparing simulations to measurements

for these settings, more than 95% of points passed when applying a gamma criteria of 2%/2 mm.

1 T

The optimised parameters found from the 0 T simulations were used to generate phase space files scored at a plane before the MLC. Simulations were then run for different MLC field sizes, with the magnetic field on. Figure 8.4 shows a simulated PDD of a 3×3 cm^2 (left) and 6×6 cm^2 (right) without a beam spoiler at SID of 2.469 m and the phantom surface 10 cm in front of isocentre. Differences in the first 2 cm can be attributed to uncertainties in the measured data which were discussed in chapter 7. It is also suspected that a magnetic field map for each MLC field size should be generated as the MLCs could be altering the fringe field and will therefore change the amount of contaminants that are magnetically focussed. The current magnetic field map does not include the shielding around the target which would also change these conditions.

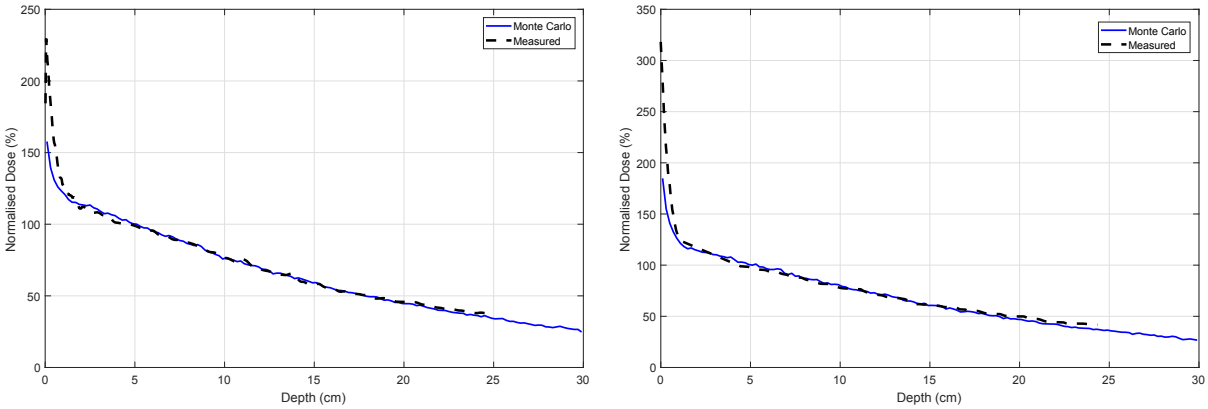

Figure 8.4: Monte Carlo (—) and measured (- - -) PDD data for MLC nominal field size of 3×3 cm^2 (left) and 6×6 cm^2 (right) without a beam spoiler. Measurements were acquired with EBT3 film at SID = 2.469 m, 1 T conditions.

Figure 8.5 shows profiles from simulations of a 3×3 cm^2 with a 2 cm beam spoiler in front of the phantom compared to measurements of the same set up. The shape of profiles agree implying that the MLC model and its location with respect to the source is accurate. The magnetic field alters the penumbra of profiles measured in water [113] therefore when the magnetic field map is updated profiles will need to be reassessed, although it is expected that the magnetic field at the region of the phantom will not vary and therefore profile penumbra should not be affected.

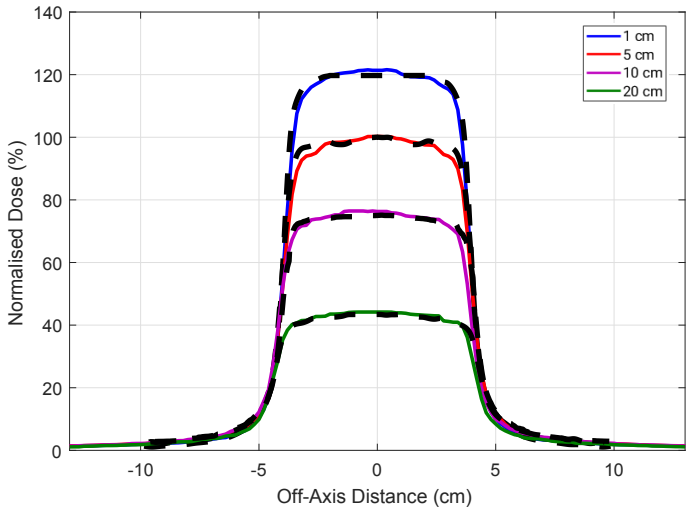

Figure 8.5: Monte Carlo (—) and measured (- - -) profile data for MLC nominal field size of 3 × 3 cm^2 with a beam spoiler. Measurements were acquired with EBT3 film at SID = 2.469 m, 1 T conditions.

8.3.2 Pinnacle^3 Model

0 T

Only limited measured data was available for modelling the 0 T beam in Pinnacle^3. Figure 8.6 shows the match between modelled and measured open field beam data at SSD 2.8 m. Figure 8.7 includes data for a 10 × 10 cm^2 field at SSD 0.8 m. Applying a gamma acceptance criterion of 2%/2 mm the pass rates for all PDDs and profiles were ≥95% of points.

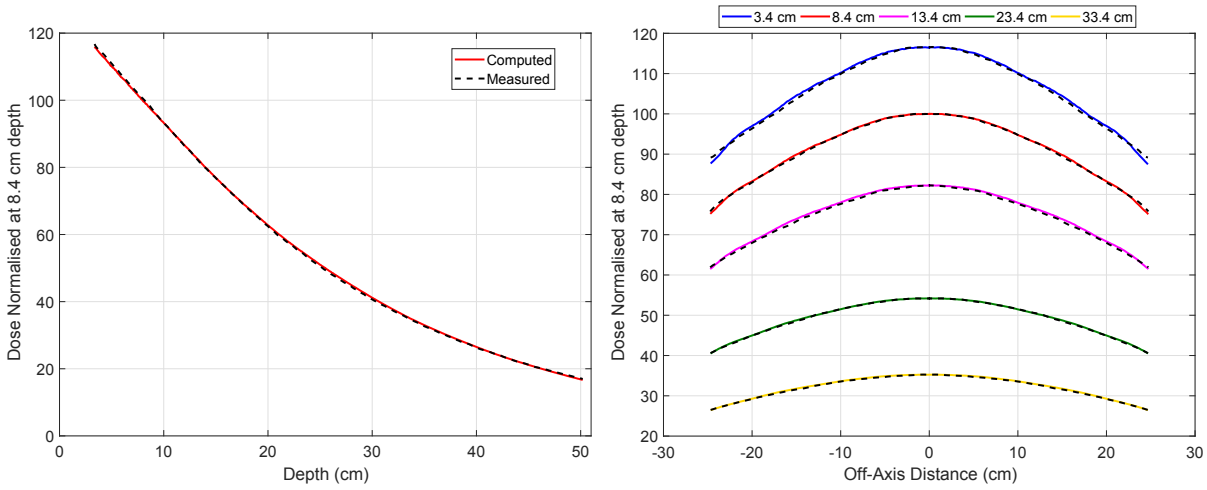

Figure 8.6: Pinnacle^3-computed (—) and measured (- - -) PDD (left) and profile (right) data for open field measured in a water tank. Measurements acquired with CC13 ion chamber, data courtesy of J. Begg. SSD = 2.8 m, 0 T conditions.

With the inclusion of a beam spoiler for the 1 T model, it was expected that the build-up would vary quite a lot therefore there was more of a focus on matching the depth dose's shape beyond the build-up region. Due to the limited measured data used for the 0 T model, it was predicted that the modelling parameters would vary from 0 T for the 1 T model. However, this data was useful for determining the correct physical machine characteristics e.g. primary collimator angle and MLC settings such as source-to-MLC distance.

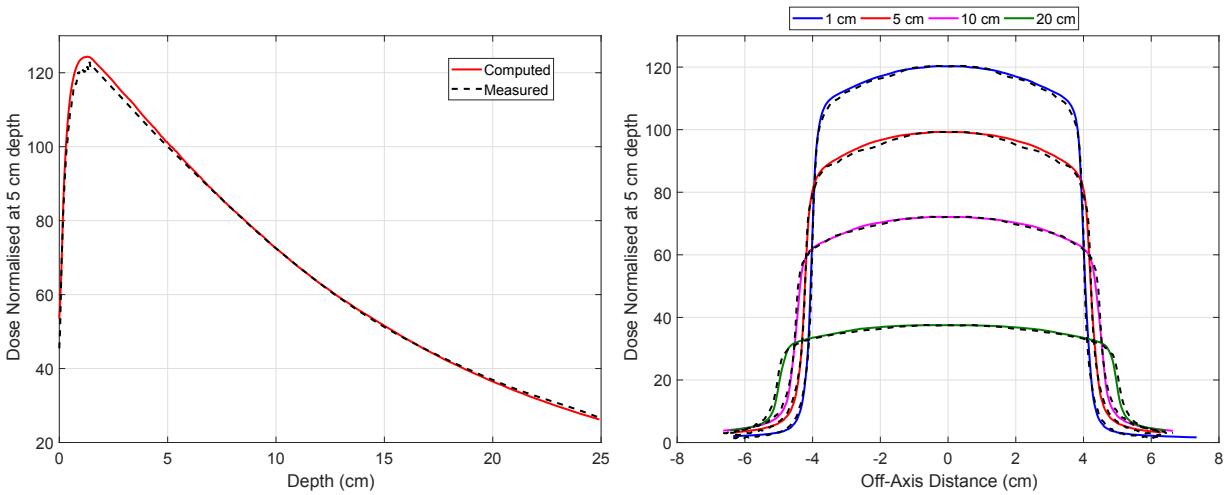

Figure 8.7: Pinnacle^3-computed (—) and measured (- - -) PDD (left) and profile (right) data for a 10 $\times$ 10 cm^2 field measured in a solid water phantom. Measured data acquired with EBT3 film. SSD = 0.8 m, 0 T conditions. PDD measured data near the surface is noisy, no smoothing was applied as this reduces the dose in this region.

1 T

Figure 8.8 (a-c) shows Pinnacle^3 computed profiles for nominal field sizes 2 $\times$ 2 cm^2, 4 $\times$ 4 cm^2 and 6 $\times$ 6 cm^2 compared to measured and the PDD for 6 $\times$ 6 cm^2 field is displayed in figure 8.8(d). Computed profiles were in agreement with measured data. To match these profiles an effective source size of 0.1 cm was used and flattening filter scatter source was set to a Gaussian height of 0.05 and width of 0.15. The MLC transmission was set to 0.01187; these parameters changed from the 0 T as a result of including more MLC data. Electron contamination parameters were also varied in order to try to reduce the build-up region. However for photon beam modelling it was difficult to completely remove the build-up region, a very short build-up is still present in figure 8.8(d). This shows the limitations of using convolution based photon beam model to match data which is lacking a standard build-up region.

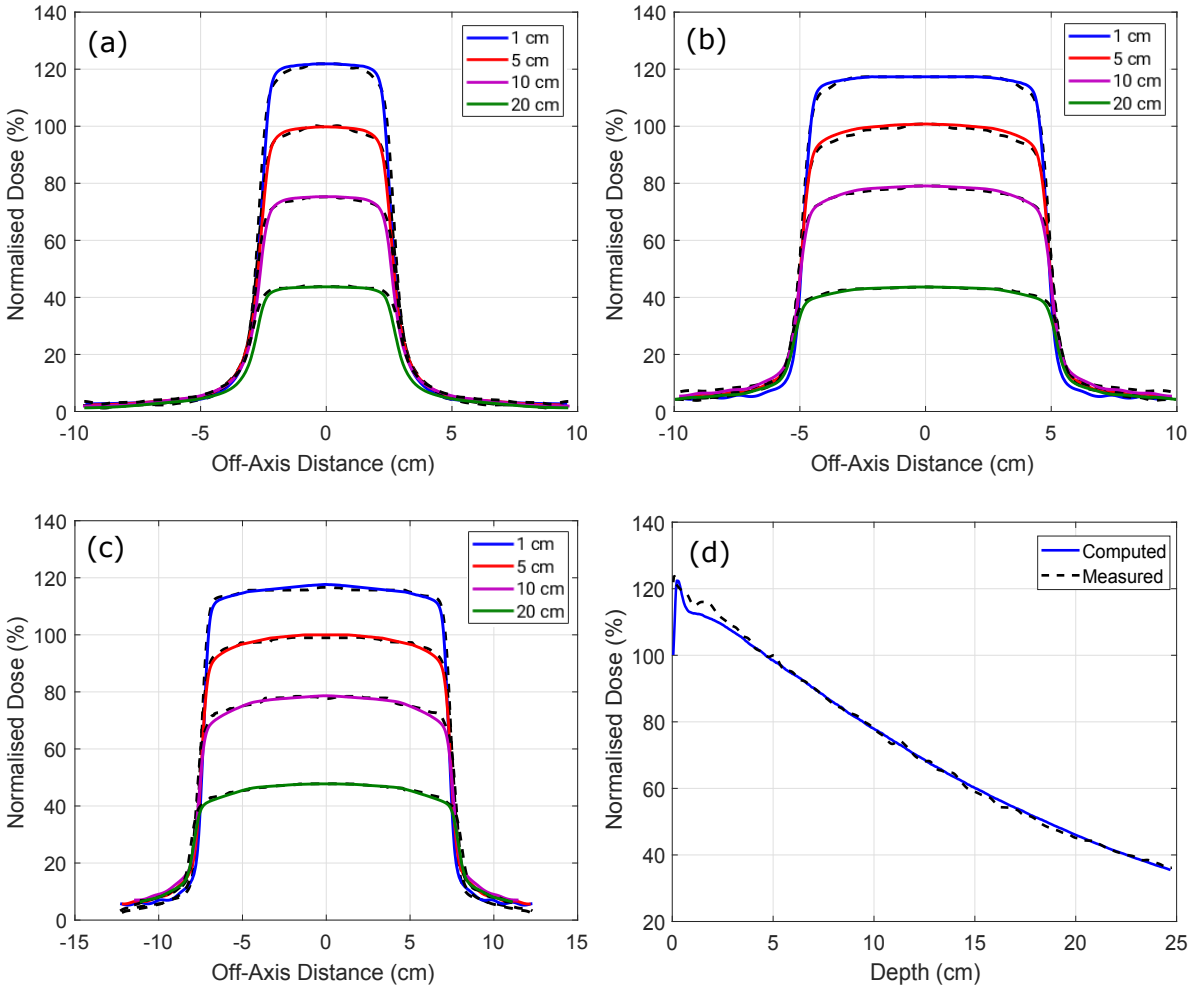

Figure 8.8: Pinnacle^3-computed (solid) and measured (dashed) data for nominal field sizes (a) 2 × 2 cm^2, (b) 4 × 4 cm^2 and (c-d) 6 × 6 cm^2. The depths of profiles are given in the legend. Measured data acquired with EBT3 film, with a beam spoiler in place. SID = 2.469 m, 1 T conditions. PDD measured data in (d) near the surface is noisy, a result of measuring with film. The computed data in (d) shows the limitations of using convolution based photon beam model to match data which is lacking a standard build-up region.

8.4 Conclusion

This chapter has described the development of the beam model for the Australian MRI-linac with Geant4 and Pinnacle^3 (TPS). The Monte Carlo incident electron beam at 0 T was characterised with the following parameters: mean energy of 6.0 MeV (FWHM of 0.2 MeV), focal spot size of 1.6 mm and target density of 21.3 g/cm^3. The 1 T simulations were shown to agree with measurements beyond the electron contamination region, however the magnetic field map needs to be updated to improve agreement in the first 2 cm of the phantom.

The TPS beam model for 0 T was in close agreement to measured data, with more than 95% of points passing for a 2%/2 mm gamma criteria. For the 1 T model, the profiles were consistent with measurements, however the PDD in the first few millimeters was difficult to match due to being unable to remove the build-up region completely for photon beam modelling.

This work has demonstrated that in order to accurately model dose deposited near the surface for an inline magnetic field it is necessary to use Monte Carlo alongside the TPS. Plans could still be created with a commercial TPS however the dose should be verified with Monte Carlo as the TPS was not capable of removing the build-up region typically present in PDDs.

Chapter 9

Discussion

Respiration-induced motion can detract from the therapeutic benefits of lung SBRT if not correctly managed. Despite the fact that many motion-management techniques have been proposed, there are still challenges for these treatments and areas which could be improved on. Accurate dose calculations are important for evaluating the different motion management strategies and their associated risks. The calculations should therefore take into account motion as well as correctly model electronic disequilibrium conditions which exist in low density media (lung) and for the small fields used in SBRT. The first few chapters of this thesis (chapters 3-4) focused on the development of a 4D Monte Carlo dose calculation tool for lung SBRT and explored some uncertainties for current treatments. These uncertainties were also briefly explored for inline MRI-linacs, by modelling a uniform magnetic field in the first instance (chapter 5).

Real time MRI-guidance has the potential to more effectively deliver lung SBRT. The dose calculation accuracy is highly important for these treatments as the magnetic field causes significant dose differences at tissue-air interfaces. For inline MRI-linacs, it has been shown that the changes caused by the magnetic field in lung depend on tumour size, density and location [115]. It is unknown if tumour motion will significantly alter the dose for inline systems, a question which could be answered with 4D dose calculations. To have a complete understanding of lung SBRT treatments for MRI-guided radiotherapy, it becomes obvious that patient- and machine- specific dose calculations should be performed. The last section of this thesis (chapters 6-8) was focused on translation of the 4D Monte Carlo dose calculation tool for the Australian MRI-linac. This involved developing experimental and computational methods for the system.

9.1 Research Aims

The aims of this thesis (outlined in chapter 1) and how they were specifically addressed is described in detail here:

9.1.1 4D Monte Carlo Dose Calculations

Aim 1: To incorporate temporal information (4D) into an in-house Monte Carlo dose calculation system in order to take into account respiratory motion and the dynamic delivery of radiation.

In chapter 3 a 4D Monte Carlo method for lung SBRT dose calculations was developed and implemented. The method was compared with 3D Monte Carlo as well as 3D- and 4D- convolution calculation methods. This work showed deviations in 3D and 4D calculations when evaluating DVH metrics for one of the treatment techniques investigated. Differences in Monte Carlo and TPS calculations demonstrated collapsed cone convolution for lung SBRT fields should be used with caution. The 4D simulations were compared with experimental film measurements taken in a dynamic thorax phantom. Overall, the 4D Monte Carlo calculated dose showed closest agreement to measured data with 3%/3 mm global pass rates greater than 95% for all plans. This tool could be used in inform on which motion management techniques are appropriate for specific patient cases.

Aim 2: To assess motion and radiation beam delivery uncertainties for lung volumetric arc therapy (VMAT) stereotactic body radiotherapy (SBRT) for current treatments and on inline MRI-linacs.

In chapter 3 motion and delivery uncertainties for current motion management techniques were also investigated with a dynamic phantom. For the plan which used a motion-encompassing margin, the interplay effect showed minor dose differences whereas MLC delivery errors were more significant; for MLC field size errors greater than 1 mm there was more than $\pm 5\%$ difference in DVH metrics. The plan which was intended for dynamic couch tracking exceeded these differences for 2 mm MLC field size error. The higher sensitivity of the motion-encompassing margin plan to systematic

MLC errors was due to the larger beam apertures it utilised. Additionally, MLC errors which resulted in significant differences were delivered and detectable with EBT3 film.

In chapter 4 motion and delivery uncertainties were simulated with patient lung datasets. A range of motion amplitudes and tumour geometries were investigated. The effect of interplay between MLC motion and target motion was minimal for all observed patient plans implying that for the mid-ventilation technique which was used for these patients, is not prone to these uncertainties. Errors in MLC leaf positions impacted the plans more significantly, in particular OAR DVH metrics were sensitive to these errors, with at least one of the OAR DVH metrics varying by more than 2% compared to the baseline plan. No clear trends as a function of motion amplitude or tumour size were observed for the cohort of patients considered.

In chapter 5 delivery uncertainties for inline MRI-linac systems were simulated for different magnetic field strengths. The impact of MLC uncertainties did not vary with magnetic field strength however it is suspected that this might not be the case for smaller target volumes. For extended source-to-isocentre distances, such is the case for the Australian MRI-linac, any errors in MLC leaf gaps or modelling the leaf ends are magnified and therefore should be considered carefully.

9.1.2 Dosimetry for inline MRI-linacs

Aim 3: To assess different methods of acquiring dosimetric data on an inline MRI-linac; the data should be suitable for beam modelling.

In chapter 6 the microDiamond and MO*Skin*™ were tested for use in inline magnetic fields. The high surface dose caused by magnetically focused contaminant electrons on the Australian MRI-linac was measured with these detectors for a range of field sizes; dose from the contaminants was shown to increase with field size as was expected. The extremely high dose gradient and electronic disequilibrium conditions of this region pose challenges to dosimetry; the MO*Skin*™ detector was advantageous for measurements under these conditions. The relative response of the microDiamond and MO*Skin*™ detectors, beyond the electron contamination region, were shown to be unaffected by the

1 T inline magnetic field since there was agreement between measurements at near 0 T and 1 T and both agreed with film within uncertainty. It was demonstrated that these detectors were useful for obtaining high resolution PDD data in an inline magnetic field.

In chapter 7 methods were developed to acquire radiation data for Monte Carlo and TPS beam modelling for an inline MRI-linac system. Due to this high electron contamination region, acquiring PDDs with film parallel to the radiation beam proved to be problematic. This method was not as accurate as those described in chapter 6. However using a beam spoiler and thus removing the electron contamination, measurements could be performed in this way for beam modelling data. Measurements performed at the 3 different SIDs showed that the electron contamination was also highly dependent on the proximity of the linac components to the MRI and importantly its fringe field. The beam data collected was of suitable quality for beam modelling purposes.

Aim 4: To model the Australian MRI-linac radiation beam in a convolution-based treatment planning system and with Monte Carlo.

In chapter 8 the work demonstrated that in order to accurately model dose deposited for an inline magnetic field it is necessary to use Monte Carlo alongside the TPS as the fringe field impacts the dose in the first few centimetres. Plans could still be created with a convolution-based TPS however the dose should be verified with Monte Carlo as the TPS is not capable of modelling the high electron contamination region at the surface.

9.2 Future Work

For future work, the 4D Monte Carlo dose calculation system should be used to investigate a larger cohort of lung cancer patients, different motion-management techniques and other uncertainties for lung SBRT. It would also be a useful tool in a study to inform on suitable dosimeters to detect clinically relevant uncertainties for current treatments of moving targets.

In terms of treatments on MRI-linacs, the next step once the treatment beam is modelled would be to investigate the effect of tumour motion on the dose distribution.

More broadly, the 4D tool could be used to inform on the appropriate magnetic field strength and orientation for lung SBRT. It could be applied to MRI-linac treatments for other clinical sites e.g. breast, cervix, pancreas, prostate, and rectum. Also of interest would be to test the accuracy of the convolution-based TPS for optimisation and dose calculations of plans in lung using the Monte Carlo model.

The high electron contamination region at the surface on the Australian MRI-linac was observed in chapter 6 and 7, methods to remove this from the primary beam should be tested experimentally. Treating off-axis is a potential solution or previously simulated solutions include purging the electrons at the level of the MLC and placing a helium gas region between the linac and patient in order to reduce the interactions which occur in the air column. This would also resolve some issues that were encountered when measuring and modelling the beam (in the TPS). In terms of the Monte Carlo model it is advised that the magnetic field map is updated for future simulation work for this system.

The assessment of delivery uncertainties for inline MRI-linac systems was somewhat limited in that it was only observed on a lung phantom for one motion pattern and tumour size. The beam model used was also for a standard clinical beam and using a uniform inline magnetic field across the phantom. Simulations using this 4D MC framework should be performed with the Australian MRI-linac beam model, and the updated magnetic field map, at the intended treatment SSD. It is recognised that a workflow would also need to be set up to convert the MRI images to electron density so that the 4D dose calculations can be performed without having to also CT patients.

Chapter 10

Conclusion

This thesis has demonstrated a functional workflow for 4D Monte Carlo dose calculations for treatment plans of lung SBRT using both current (dynamic) deliveries and MRI-guided radiotherapy. The small fields, high dose gradients, varying density in lung and variation as a result of motion in lung SBRT contribute to differences between planned and measured dose. The 4D tool improved the agreement to measurements performed in a dynamic phantom, particularly in regions where significant density variations occur as a result of motion.

MRI-guided radiotherapy for lung SBRT treatments will require modelling both the magnetic field and motion as both alter the dose distribution. With this 4D tool it is recommended that studies be performed which observe various motion patterns and amplitudes, tumour locations and sizes as well as magnetic fields to investigate how these variables effect changes in the dose distribution.

4D simulation studies were performed to investigate both motion and delivery tolerances for lung SBRT. The lung patient study demonstrated that small shifts in MLCs had significant impact on plans. Considering that for MRI-linac systems the change in dose distributions is strongly dependent on the field size, translation of this study for these systems is important. In the first instance this was carried out for a phantom study with uniform magnetic fields. The study showed negligible variation from 0 T results however with a more complex geometry i.e. patients, smaller tumour sizes and for realistic magnetic field models, this could change.

While transverse MRI-linacs are available commercially, inline MRI-linacs demonstrate promising qualities, particularly for lung SBRT. In this thesis, methods were developed to experimentally and computationally characterise an inline MRI-linac. The 4D tool developed in this work as well as the novel dosimetry methods presented will assist with future clinical decisions for the treatment of lung SBRT using MRI-linacs.

Bibliography

[1] Glide-Hurst CK, Chetty IJ, "Improving radiotherapy planning, delivery accuracy, and normal tissue sparing using cutting edge technologies," *J Thorac Dis*, vol. 6, no. 4, pp. 303–318, 2014.

[2] Keall PJ, Magera GS, Balter JM et al, "The management of respiratory motion in radiation oncology report of AAPM Task Group 76," *Med Phys*, vol. 33, no. 10, pp. 3874–3900, 2006.

[3] Lagendijk J J W, Raaymakers B W, Raaijmakers A J E et al, "MRI/linac integration," *Radiother Oncol*, vol. 86, pp. 25–29, 2008.

[4] Raaijmakers AJE, Raaymakers BW, Lagendijk JJW, "Integrating a 1.5 T MRI scanner with a 6 MV radiotherapy accelerator: dose increase at tissue-air interfaces in a lateral magnetic field due to returning electrons," *Phys Med Biol*, vol. 50, pp. 1363–1376, 2005.

[5] Marks LB, Yorke ED, Jackson A et al, "Use of Normal Tissue Complication Probability Models in the Clinic," *Int J Radiat Oncol Biol Phys*, vol. 76, no. 3, pp. S10–S19, 2010.

[6] McRobbie DW, Moore EA, Graves MJ, Prince MR , *MRI from Picture to Proton*. Cambridge University Press, 2006.

[7] Bushberg JT, Seibert JA, Leidholdt EM, Boone JM, *The essential physics of medical imaging*. Lippincott Williams & Wilkins, 2011.

[8] Geva T, "Magnetic resonance imaging: historical perspeactive," *J Cardiovasc Magn Reson*, vol. 8, no. 4, pp. 573–580, 2006.

[9] Metcalfe P, Liney GP, Holloway L et al, "The Potential for an Enhanced Role For MRI in Radiation-Therapy Treatment Planning," *Technol Cancer Res Treat*, vol. 12, no. 5, pp. 429–446, 2013.

[10] The International Commision on Radiation Units and Measurements, "Prescribing, Recording and Reporting Photon Beam Therapy. ICRU Report 62," *J ICRU*, 1999.

[11] The International Commision on Radiation Units and Measurements, "Prescribing, Recording and Reporting Photon-Beam Intensity-Modulated Radiation Therapy (IMRT). ICRU Report 83," *J ICRU*, vol. 10, no. 1, p. (94pp.), 2010.

[12] The International Commision on Radiation Units and Measurements, "Prescribing, Recording and Reporting Small Beam SRT. ICRU Report 91.," *J ICRU*, vol. 14, no. 2, p. (145pp.), 2014.

[13] Vinod SK, Jameson MG, Min M, Holloway LC, "Uncertainties in volume delineation in radiation oncology: A systematic review and recommendations for future studies," *Radiather Oncol*, vol. 121, no. 2, pp. 169–179, 2016.

[14] Ahnesjo A, Aspradakis MM, "Dose calculations for external photon beams in radiotherapy," *Phys Med Biol*, vol. 44, pp. R99–R155, 1999.

[15] Jaffray DA, Lindsay PE, Brock KK, Deasy JO, Tomé WA, "Accurate accumulation of dose for improved understanding of radiation effects in normal tissue," *Int J Radiat Oncol Biol Phys*, vol. 76, pp. S135–S139, 2010.

[16] Papanikolaou N, Battista J, Boyer AL, et al, "Tissue inhomogeneity corrections for megavoltage photon beams. The report of Task Group No. 65 of the radiation therapy committee of the AAPM," *Med Phys*, 2004.

[17] Meredith WJ, "40 years of development in radiotherapy," *Phys Med Biol*, vol. 29, no. 2, pp. 115–120, 1984.

[18] Metcalfe P, Kron T, Hoban P, *The Physics of Radiotherapy X-rays and Electrons*. Medical Physics Publishing, 2007.

[19] Mayles P, Nahum A, Rosenwald JC, *Handbook of Radiotherapy Physics: Theory and Practice*. Taylor and Francis Group, 2007.

[20] Oelkfe U, Scholz C, *Dose Calculation Algorithms. In: Schlegel W., Bortfeld T., Grosu AL. (eds) New Technologies in Radiation Oncology.* Springer, 2006.

[21] Knöös T, Wieslander E, Cozzi L et al, "Comparison of dose calculation algorithms for treatment planning in external photon beam therapy for clinical situations," *Phys Med Biol*, vol. 51, pp. 5785–5807, 2006.

[22] Ahnesjo A, "Collapsed cone convolution of radiant energy for photon dose calculation in heterogenous media," *Med Phys*, vol. 16, no. 4, pp. 577–592, 1989.

[23] McNutt T, "Pinnacle^3 White Paper: Collapsed Cone Convolution Superposition and Delta Pixel Beam," *Royal Phillips Electronics*, 2002.

[24] Boyer A, Mok E, "A photon dose distribution model employing convolution calculations," *Med Phys*, vol. 12, pp. 169–177, 1985.

[25] Mackie TR, Scrimger JW, Battista JJ, "A convolution method of calculating dose for 15-MV x rays," *Med Phys*, vol. 12, pp. 188–196, 1985.

[26] Mackie TR, Bielajew AF, Rogers DW, Battista JJ, "Generation of photon energy deposition kernels using the EGS Monte Carlo code," *Phys Med Biol*, vol. 33, pp. 1–20, 1988.

[27] Bedfore JL, "Calculation of absorbed dose in radiotherapy by solution of the lineat Boltzmann transport equations," *Phys Med Biol*, vol. 64, p. 02TR01 (21pp), 2019.

[28] Jaffray DA, Siewerdsen JH, Wong JW, Martinez AA, "Flat-panel cone-bea, computed tomogrpahy fr image-guided radiation therapy," *Int J Radiat Oncol Biol Phys*, vol. 53, no. 5, pp. 1337–1349, 2002.

[29] Herman MG, "Clinical use of electronic portal imaging," *Semin Radiat Oncol*, vol. 15, no. 3, pp. 157–167, 2005.

[30] Timmmerman R, Park C, Kavanagh BD, "The North American Experience with Stereotactic Body Radiation Therapy in Non-small Cell Lung Cancer," *J Torac Oncol*, vol. 2, pp. S101–S112, 2007.

[31] Guckenberger M, Andratschke, Alheit H et al, "Definition of stereotactic body radiotherapy: Principles and practice for the treatment of stage I non-small cell lung cancer," *Strahlenther Onkol*, vol. 190, pp. 26–33, 2014.

[32] Nagata Y, Takayama K, Matsuo Y et al, "Clinical outcomes of a phase I/II study of 48 Gy of stereotactic body radiotherapy in 4 fractions for primary lung cancer using a stereotactic body frame," *Int J Radiat Oncol Biol Phys*, vol. 63, pp. 1427–1431, 2005.

[33] Baumann P, Nyman J, Hoyer M et al, "Outcome in a prospective phase II trial of medically inoperable stage I non-small-cell lung cancer patients treated with stereotactic body radiotherapy," *J Clin Oncol*, vol. 27, pp. 3290–3296, 2009.

[34] Timmmerman R, Filippi AR, Guarneri A, "Stereotactic body radiation therapy for inoperable early stage lung cancer," *JAMA*, vol. 303, no. 11, pp. 1070–1076, 2010.

[35] Nagata Y, Matsuo Y, Takayama K et al, "Current status of stereotactic body radiotherapy for lung cancer," *Int J Clin Oncol*, vol. 12, pp. 3–7, 2007.

[36] Smilowitz JB, Das IJ, Feygelman V, "AAPM Medical Physics Practice Guideline 5.a.: Commissioning and QA of treatment planning dose calculations - Megavoltage photon and electron beams," *J Appl Clin Med Phys*, vol. 16, no. 5, pp. 14–34, 2015.

[37] Das IJ, Cheng CW, Watts RJ et al, "Accelerator beam data commisioning equipment and procedures: Report of TG-106 of the Therapy Physics Committee of the AAPM," *Med Phys*, vol. 35, no. 8, pp. 4186–4215, 2008.

[38] Klein EE, Janley J, Bayouth J, "AAPM Task Group 142 report: Quality assurance of medical accelerators," *Med Phys*, vol. 36, no. 9, pp. 4197–4212, 2009.

[39] Parsai H, Cho PS, Phillips MH, Giansiracusa S, Axen D, "Random and systematic beam modulator errors in dynamic intensity modulated radiotherapy," *Phys Med Biol*, vol. 48, no. 9, pp. 1109–1121, 2001.

[40] Mu G, Ludlum E, Xia P, "Impact of MLC leaf position errors on simple and complex IMRT plans for head and neck cancer," *Phys Med Biol*, vol. 53, no. 1, pp. 77–88, 2008.

[41] Rangel A, Dunscombe P, "Tolerances on MLC leaf position accuracy for IMRT delivery with a dynamic MLC," *Med Phys*, vol. 36, no. 7, pp. 3304–3309, 2009.

[42] Oliver M, Gagne I, Bush K, Zavgorodni S, Ansbacher W, and Beckham W, "Clinical significance of multi-leaf collimator positional errors for volumetric modulated arc therapy," *Radiother Oncol*, vol. 97, no. 3, pp. 554–560, 2010.

[43] Oliver M, Bush K and Zavgorodni S, "Understanding the impact of the Rapidarc therapy delivery errors for prostate cancer," *J Appl Clin Med Phys*, vol. 12, no. 3, pp. 32–43, 2011.

[44] Pogson EM, Arumugam S Hansen CR et al, "Multi-institutional comparison of simulated treatment delivery errors for ssIMRT manually planned VMAT and autoplan-VMAT plans for nasopharyngeal radiotherapy," *Phys Med*, vol. 42, pp. 55–66, 2017.

[45] Blake SJ, Arumugam S, Holloway L et al, "Investigating the impact of treatment delivery uncertaintie on treatment effectiveness for lung SABR," *Australia Phys Eng Sci Med*, vol. 40, no. 4, pp. 823–829, 2017.

[46] Sapkaroski D, Osborne C, Knight KA, "A review of stereotactic body radiotherapy - is volumetric modulated arc therapy the answer?," *J Med Radiat Sci*, vol. 62, pp. 142–151, 2015.

[47] Balter JM, Ten Haken RK, Lawrence TS et al, "Uncertainties in CT-based radiation therapy treatment planning associated with patient breathing," *Int J Radiat Oncol Biol Phys*, vol. 36, pp. 167–174, 1996.

[48] Wolthaus JW, Scheider C, Sonke JJ, Herk Mv, Belderbos oS, Rossi MM, "Mid-ventilation CT scan construction from four-dimensional respiration-correlated CT scans for radiotherapy planning of lung cancer patients," *Int J Radiat Oncol Biol Phys*, vol. 65, no. 5, pp. 1560–1571, 2006.

[49] Keall PJ, Kini VR, Vdem SS, Mohan R, "Potential radiotherapy improvements with respiratory gating," *Australas Phys Eng Sci Med*, vol. 25, no. 1, p. (6pp.), 2002.

[50] Wolthaus JW, Sonke JJ, Herk Mv et al, "Comparison of different strategies to use four-dimensional computed tomography in treatment planning for lung cancer patients," *Int J Radiat Oncol Biol Phys*, vol. 70, no. 4, pp. 1229–1238, 2008.

[51] Dobler B, Walter C, Knopf A, Fabri D, Loeschel R, Polednik M, Schneider F, Wenz F, Lohr F, "Optimization of extracranial stereotactic radiation therapy of small lung lesions using accurate dose calculation algortihms," *Radiat Oncol*, vol. 1, no. 45, p. (11pp), 2006.

[52] Tian Y, Wang Z, Ge H, Zhang T, Cai J, Kelsey C, Yoo D, Yin FF, "Dosimetric comparison of treatment plans based on free breathing, maximum, and average intensity projection CTs for lung cancer SBRT," *Med Phys*, vol. 39, no. 5, pp. 2754–2760, 2012.

[53] Krieger T, Sauer OA, "Monte Carlo- versus pencil-beam-/collapsed-cone dsoe calculation in a heterogenous multi-layer phantom," *Phys Med Biol*, vol. 50, pp. 859–868, 2005.

[54] Vanderstraeten B, Reynaert N, Paelinck L et al, "Accuracy of patient dose calculation for lung IMRT: A comparison of Monte Carlo, convolution/superposition, and pencil beam computations," *Med Phys*, vol. 33, no. 9, pp. 3149–3158, 2006.

[55] Hasenbalg F, Neuenschwander H, Mini R, Born EJ, "Collapsed cone convolution and analytical anisotrpoic algorithm dose calculations compared to VMC++ Monte Carlo simulations in clinical cases," *Phys Med Biol*, vol. 52, pp. 3679–3691, 2007.

[56] Calvo OI, Gutiérrez AN, Stathakis S, Esquivel C, Papanikolaou N, "On the quantification of the dosimetric accuracy of colllapsed cone convolution superposition (CCCS) algorithm for small lung volumes using IMRT," *J Appl Clin Med Phys*, vol. 13, no. 3, pp. 43–59, 2012.

[57] Fogliata A, Cozzi L, "Dose calculation algorithm accuracy for small fields in non-homogenous media: The lung SBRT case," *Phys Med*, vol. 44, pp. 157–162, 2017.

[58] Panettieri V, Wennberg B, Gagliardi G, Duch MA, Ginjaume M, Lax I, "SBRT of lung tumours: Monte Carlo simulation with PENELOPE of dose distributions including respiratory motion and comparison with treatment planning systems," *Phys Med Biol*, vol. 52, pp. 4265–4281, 2007.

[59] Li J, Galvin J, Harrison A, Timmerman R, Yu Y, Xiao Y, "Dosimetric verification using Monte Carlo calculations for tissue heterogeneity-corrected conformal treatment plans following RTOG 0813 dosimetic criteria for lung cancer stereotactic body radiotherapy," *Int J Radiat Oncol Biol Phys*, vol. 84, no. 2, pp. 508–513, 2012.

[60] Hardcastle NG, Oborn BM, Haworth A, "On the use of a convolution-superposition algorithm for plan checking in lung stereotactic body radiation therapy," *J Appl Clin Med Phys*, vol. 17, no. 5, pp. 1–12, 2016.

[61] Bortfeld T, Jiang SB, Rietzel E, "Effects of motion on the total dose distribution," *Semin Radiat Oncol*, vol. 14, no. 1, pp. 41–54, 2004.

[62] Keall P, Siebers JV, Joshi S, Mohan R, "Monte Carlo as a four-dimensional radiotherapy treatment planning tool to account for respiratory motion," *Phys Med Biol*, vol. 49, no. 16, pp. 3639–3648, 2004.

[63] Guckenberger M, Wilbert J, Krieger T et al, "Four-dimensional treatment planning for stereotactic body radiotherapy," *Int J Radiat Oncol Biol Phys*, vol. 69, no. 1, pp. 276–285, 2007.

[64] Glide-Hurst CK, Hugo GD, Liang J, Yan D, "A simplified method of four-dimensional dose accumulation using the mean patient density representation," *Med Phys*, vol. 35, no. 12, pp. 5269–5277, 2008.

[65] Vinogradskiy Y, Balter P, Followill DS, Alvarez PE, White RA, Startschall G, "Comparing the accuracy of four-dimensional photon dose calculations with three-dimensional calculations using moving and deforming phantoms," *Med Phys*, vol. 36, no. 11, pp. 5000–5006, 2009.

[66] Ding M, Newman F, Gaspar L et al, "A 4D treatment planning tool for the evaluation of motion effects on lung cancer treatments," *J Phys Conf Ser*, vol. 102, p. 012008, 2008.

[67] Seco J, Sharp GC, Wu Ziji, Gierga D, Buettner F, Paganetti H, "Dosimetric impact of motion in free-breathing and gated lung radiotherapy: A 4D Monte Carlo study of intrafraction and interfraction effects," *Med Phys*, vol. 35, no. 1, pp. 356–366, 2008.

[68] Jensen MD, Abdellatif A, Chen J, Wong E, "Study of IMRT interplay effect using a 4DCT Monte Carlo dose calculation," *Phys Med Biol*, vol. 57, no. 8, pp. N89–N99, 2012.

[69] Zou Q, Yin L, Shen J, Corradetti MN et al, "Dynamic simulation of motion effects in IMAT lung SBRT," *Rad Oncol*, vol. 9, no. 1, p. 225, 2014.

[70] Freislederer P, von Münchow A, Kamp F et al, "Comparison of planned dose on different CT image sets to four-dimensional Monte Carlo dose recalculation using the patients actual breathing trace for lung stereotactic body radiation therapy," *Med Phys*, vol. 46, pp. 3268–3277, 2019.

[71] Rao M, Wu J, Cao D et al, "Dosimetric impact of breathing motion in lung stereotactic body radiotherapy treatment using image-modulated radiotherapy and volumetric modulated arc therapy," *Int J Radiat Oncol Biol Phys*, vol. 83, no. 2, pp. 251–256, 2012.

[72] Ehrbar S, Lang S, Stieb S et al, "Three-dimensional versus four-dimensional dose calculation for volumetric modulated arc therapy of hypofractionated treatments," *Z Med Phys*, vol. 26, pp. 45–53, 2016.

[73] Kurup G, "CyberKnife: A new paradigm in radiotherapy," *J Med Phys*, vol. 35, no. 2, pp. 63–64, 2010.

[74] Shah AP, Kupelian A, Waghorn BJ et al, "Real-time tumor tracking in the lung using an electromagnetic tracking system," *Int J Radiat Oncol Biol Phys*, vol. 86, no. 3, pp. 477–483, 2013.

[75] Sonke JJ, Rossi M, Wolthaus J, van Herk M, Damen E, Belderbos J, "Frameless stereotactic body radiotherapy for lung cancer using four-dimensional cone beam CT guidance," *Int J Radiat Oncol Biol Phys*, vol. 74, no. 2, pp. 567–574, 2009.

[76] Nioutsikou E, Seppenwoodle Y, Symonds-Tayler N, Heijmen B, Evans P, Webb S, "Dosimetric investigation of lung tumor motion compensation with a robotic respiratory tracking system: an experimental study," *Med Phys*, vol. 35, no. 4, pp. 1232–1240, 2008.

[77] Falk M, Munck af Rosenschold P, Keall P et al, "Real-time dynamic MLC tracking for inversely optimised arc radiotherapy," *Radiother Oncol*, vol. 94, no. 2, pp. 218–223, 2010.

[78] Bertholet J, Knopf A, Eiben B et al, "Real-time intrafraction motion moniroting in external beam radiotherapy," *Phys Med Biol*, vol. 44, no. 15TR01, p. 33pp, 2019.

[79] Bainbridge H Salem A, Tijseen RHN et al, "Review Article: Magnetic resonance imaging in precision radiation therapy for lung cancer," *Transl Lung Cancer Res*, vol. 6, no. 6, pp. 689–707, 2017.

[80] Mutic S, Dempsey JF, "The ViewRay system: magnetic resonance-guided and controlled radiotherapy.," *Semin Radiat Oncol*, vol. 24, pp. 196–199, 2014.

[81] Lagendijk JJW, Raaymakers BW, van Vulpen M, "The magnetic resonance imaging-linac system," *Semin Radiat Oncol*, vol. 24, pp. 207–209, 2014.

[82] Fallone BG, "The rotating biplanar linac–magnetic resonance imaging system," *Semin Radiat Oncol*, vol. 24, pp. 200–202, 2014.

[83] Keall PJ, Barton M, Crozier S, "The Australian magnetic resonance imaging–linac program," *Semin Radiat Oncol*, vol. 24, pp. 20–206, 2014.

[84] Kolling S, Oborn B, Keall P, "Impact of the MLC on the MRI field distortion of a prototype MRI-linac," *Med Phys*, vol. 40, no. 12, pp. 121705–(1–10), 2013.

[85] Burke B, Lamey M, Rathee S, Murray B, Fallone BG, "Radio frequency noise from clinical linear accelerators," *Phys Med Biol*, vol. 54, no. 8, pp. 2483–2492, 2009.

[86] Burke B, Ghila A, Fallone BG, Rathee S, "Radiation induced current in the RF coils of integrated linac-MR systems: The effect of buildup and magnetic field," *Med Phys*, vol. 39, no. 8, pp. 5004–5014, 2012.

[87] Raaymakers BW, Lagendijk JJW, Overweg J et al, "Integrating a 1.5 T MRI scanner with a 6 MV accelerator: proof of concept," *Phys Med Biol*, vol. 54, pp. N229–N237, 2009.

[88] St-Aubin J, Steciw S, Fallone BG, "Magnetic decoupling of the linac in a low field biplanar linac-MR system," *Med Phys*, vol. 37, no. 9, pp. 4755–4761, 2010.

[89] Lamey M, Burke B, Blosser E, Rathee S, De Zanche N, Fallone B, "Radio frequency shielding for a linac-MRI system," *Phys Med Biol*, vol. 55, no. 4, pp. 995–1006, 2010.

[90] Liney GP, Dong B, Begg J et al, "Technical Note: Experimental results from a prototype high-field inline MRI-linac," *Med Phys*, vol. 43, no. 9, pp. 5188–5194, 2016.

[91] St-Aubin J, Santos D, Steciw S, Fallone BG, "Effect of longitudinal magnetic fields on a simulated in-line 6 MV linac," *Med Phys*, vol. 37, no. 9, pp. 4916–4923, 2010.

[92] St-Aubin J, Steciw S, Kirkby C, Fallone BG, "An integrated 6 MV linear accelerator model from electron gun to dose in a water tank," *Med Phys*, vol. 37, no. 5, pp. 2279–2288, 2010.

[93] Constantin DE, Fahrig R, Keall PJ, "A study of the effect of in-line and perpendicular magnetic fields on beam characteristics of electron guns in medical linear accelerators," *Med Phys*, vol. 38, no. 7, pp. 4174–4185, 2011.

[94] Constantin DE, Holloway L, Keall PJ, Fahrig R, "A novel electron gun for inline MRI-linac configurations," *Med Phys*, vol. 41, no. 2, p. 022301 (10pp.), 2014.

[95] Whelan B, Holloway L, Constantin D, Oborn B, Bazalova-Carter M, Fahrig R, Keall P, "Performance of a clinical gridded electron gun in magnetic fields: Implications for MRI-linac therapy," *Med Phys*, vol. 43, no. 11, pp. 5903–5914, 2016.

[96] Santos DM, St-Aubin J, Fallone BG, Steciw S, "Magnetic shielding investigation for a 6 MV in-line linac with the parallel configuration of a linac-mr system," *Med Phys*, vol. 39, no. 2, pp. 788–797, 2012.

[97] Overweg J, Raaymakers B, Lagendijk J, Brown K, "System for MRI guided Radiotherapy," *Proc Int Soc Magn Reson Med*, vol. 17, p. 594, 2009.

[98] Whelan B, Kolling S, Oborn BM, Keall P, "Pasive magnetic shielding in MRI-Linac systems," *Phys Med Biol*, vol. 63, p. 075008 (15pp.), 2018.

[99] Raaijmakers AJE, Raaymakers BW, Lagendijk JJW, "Magnetic-field-induced dose effects in MR-guided radiotherapy systems: dependence on magnetic field strength," *Phys Med Biol*, vol. 53, pp. 909–923, 2008.

[100] Gargett M, Oborn B, Metcalfe P, Rosenfeld AB, "Monte Carlo simulation of the dose response of a novel 2D silicon diode array for use in hybrid MRI-LINAC systems," *Med Phys*, vol. 42, pp. 856–865, 2015.

[101] Raaymakers BW, Raaijmakers AJE, Kotte ANTJ, Jette D, Lagendijk JJW, "Integrating a 1.5 T MRI scanner with a 6 MV radiotherapy accelerator: dose deposition in a transverse magnetic field," *Phys Med Biol*, vol. 49, pp. 4109–4118, 2004.

[102] Raaijmakers AJE, Raaymakers BW, Lagendijk JJW, "Integrating a 1.5 T MRI scanner with a 6 MV radiotherapy accelerator: impact of the surface orientation on the entrance and exit dose due to the transverse magnetic field," *Phys Med Biol*, vol. 52, no. 4, pp. 929–939, 2007.

[103] Keyvanloo A, Burke B, Warkentin B et al, "Skin dose in longitudinal and transverse linac-MRIs using Monte Carlo and realistic 3D MRI field models," *Med Phys*, vol. 39, no. 10, pp. 6509–6521, 2012.

[104] Hackett SL, van Asselen B, Wolthaus JWH et al, "Spiraling contaminent electrons increase doses to surfaces outside the photon beam of an MRI-linac with a perpendicular magnetic field," *Phys Med Biol*, vol. 63, p. (10pp.), 2018.

[105] Bielajew AF, "The effect of strong longitudinal magnetic fields on dose deposition from electron and photon beams," *Med Phys*, vol. 20, no. 4, pp. 1171–1179, 1993.

[106] Oborn BM, Metcalfe PE, Butson MJ, Rosenfeld AB, Keall PJ, "Electron contamination modeling and skin dose in 6 MV longitundinal field MRIgRT: Impact of the MRI and MRI fringe field," *Med Phys*, vol. 39, no. 2, pp. 874–890, 2012.

[107] Oborn BM, Kolling S, Metcalfe PE, Crozier S, Litzenberg DW, Keall PJ, "Electron contamination modeling and reduction in a 1 T open bore inline MRI-linac system," *Med Phys*, vol. 41, no. 5, p. 0517908, 2014.

[108] Keyvanloo A, Burke B, St-Aubin J, "Minimal skin dose increase in longitudinal rotating biplanar linac-MR systems: examination of radiation energy and flattening filter design," *Phys Med Biol*, vol. 61, pp. 3527–3539, 2016.

[109] Ghila A, Steciw S, Fallone BG, Rathee S, "Experimental verification of EGSnrc Monte Carlo calculated depth doses within a realistic parallel magnetic field in a polystyrene phantom," *Med Phys*, vol. 44, no. 9, pp. 4804–4815, 2017.

[110] Menten MJ, Wetscherek A, Fast MF, "MRI-guided lung SBRT: Presnt and future developments," *Phys Med*, vol. 44, pp. 139–149, 2017.

[111] Raaijmakers AJE, Hardemark B, Raaymakers BW, Raaijmakers CPJ, Lagendijk JJW, "Dose optimization for the MRI-accelerator: IMRT in the presence of a magnetic field," *Phys Med Biol*, vol. 52, no. 23, pp. 7045–7054, 2007.

[112] Bol GH, Lagendijk JJW, Raaymakers BW, "Compensating for the impact of non-stationary spherical air cavities on IMRT dose delivery in transverse magnetic fields," *Phys Med Biol*, vol. 60, pp. 755–768, 2015.

[113] Alnaghy SJ, Begg J, Causer T et al, "Technical Note: Penumbral width trimming in solid lung dose profiles for 0.9 and 1.5 T MRI-Linac prototypes," *Med Phys*, vol. 45, no. 1, pp. 479–487, 2018.

[114] Kirkby C, Murray, Rathee S, Fallone BG, "Lung dosimetry in a linac-MRI radiotherapy unit with a longitudinal magnetic field," *Med Phys*, vol. 37, no. 9, pp. 4722–4732, 2010.

[115] Oborn BM, Ge Y, Hardcastle N, Metcalfe PE, Keall PJ, "Dose enhancement in radiotherapy of small lung tumours using inline magenetic fields: A Monte Carlo based planning study," *Med Phys*, vol. 43, no. 1, pp. 368–377, 2016.

[116] Oborn BM, Gargett MA, Causer TJ et al, "Experimental verification of dose enhancement effects in lung phantom from inline magnetic fields," *Radiother Oncol*, vol. 125, pp. 433–438, 2017.

[117] Edmund JE, Nyholm T, "A review of substitute CT generation for MRI-only radiation therapy," *Rad Oncol*, vol. 12, no. 28, p. 15pp., 2017.

[118] Brock KK, "Results of a multi-institution deformable registration accuracy study (MIDRAS)," *Int J Radiat Oncol Biol Phys*, vol. 76, pp. 583–596, 2010.

[119] Fransson A, Andreo P, Pötter R, "Aspects of MR image distortions in radiotherapy treatment Planning," *Strahlenther und Onkol*, vol. 177, no. 2, pp. 59–73, 2001.

[120] Wang D, Strugnell W, Cowin G, Doddrell DM, Slaughter R, "Geometric distortion in clinical MRI systems: Part I: evaluation using a 3D phantom," *Magn Reson Imaging*, vol. 22, no. 9, pp. 1211–1221, 2004.

[121] Wild J, Marshall H, Bock M et al, "MRI of the lung (1/3): methods," *Insights Imaging*, vol. 3, pp. 345–353, 2012.

[122] Kumar S, Liney G, Rai R, Holloway L, Moses D, Vinod SK, "Magnetic resonance imaging in lung: a review of its potential for radiotherapy," *Br J Radiol*, vol. 89, p. 20150431, 2016.

[123] Cai J, Chang Z, Wang Z, Paul Segars W, Yin FF, "Four-dimensional magnetic resonance imaging (4D-MRI) using image-based respiratory surrogate: a feasibility study," *Med Phys*, vol. 38, pp. 6384–6394, 2011.

[124] Hu Y, Caruthers SD, Low DA, Parikh PJ, Mutic S, "Respiratory amplitude guided 4-dimensional magnetic resonance imaging," *Int J Radiat Oncol Biol Phys*, vol. 86, pp. 198–204, 2013.

[125] Yang W, Fan Z, Tuli R, Deng Z, Pang J, Wachsman A, Reznik R, Sandler H, Li D and Fraass BA, "Four-dimensional magnetic resonance imaging With

3-dimensional radial sampling and self-gating-based K-space sorting: early clinical experience on pancreatic cancer patients," *Int J Radiat Oncol Biol Phys*, vol. 93, p. S19, 2015.

[126] Stemkens B, Tijssen RH, de Senneville BD, Heerkens HD, van Vulpen M, Lagendijk JJ, van den Berg CA, "Optimizing 4-dimensional magnetic resonance imaging data sampling for respiratory motion analysis of pancreatic tumors," *Int J Radiat Oncol Biol Phys*, vol. 91, no. 3, pp. 571–578, 2015.

[127] Stemkens B, Paulson ES, Tijssen RH, "Nuts and bolts of 4D-MRI for radiotherapy," *Phys Med Biol*, vol. 21TR01, p. 23pp, 2018.

[128] Meijsing I, Raaymakers BW, Raaijmakers AJE et al, "Dosimetry for the MRI accelerator: the impact of a magnetic field on the response of a farmer NE2571 ionization chamber," *Phys Med Biol*, vol. 54, p. 2993–3002, 2009.

[129] Reynolds M, Fallone BG, Rathee S, "Dose response of selected ion chambers in applied homogeneous transverse and longitudinal magnetic fields," *Med Phys*, vol. 40, p. 042102, 2013.

[130] Reynolds M, Fallone BG, Rathee S, "Dose response of selected solid state detectors in applied homogeneous transverse and longitudinal magnetic fields," *Med Phys*, vol. 41, no. 9, p. 092103, 2014.

[131] Hackett SL, van Asselen B, Wolthaus JW et al, "Consequences of air around an ionization chamber: Are exisiting solid phantoms suitable for reference dosimetry on an MR-linac?," *Med Phys*, vol. 43, no. 7, pp. 3961–3968, 2016.

[132] Podgorsak EB, *Radiation Oncology Physics: a handbook for teachers and students*. IAEA, 2005.

[133] Smit K, Kok JGM, Aalbers AH, Lagendijk JJW, Raaymakers BW, "Towards reference dosimetry for the MR-linac: magnetic field correction of the ionization chamber reading," *Phys Med Biol*, vol. 58, pp. 5945–5957, 2014.

[134] Smit K, Sjöholm J, Kok JGM, Lagendijk JJW, Raaymakers BW, "Relative dosimetry in a 1.5 T magnetic field: an MR-linac compatible prototype scanning water phantom," *Phys Med Biol*, vol. 59, pp. 4099–4109, 2014.

[135] Goddu S, Green OP, Mutic S, "TG-51 calibration of first commercial MRI-guided IMRT system in the presence of 0.35 tesla magnetic field," *Med Phys*, vol. 39, p. 3968, 2012.

[136] Malkov VN, Rogers DW, "Sensitive volume effects on Monte Carlo calculated ion chamber response in magnetic fields," *Med Phys*, vol. 44, p. 4854–4858, 2017.

[137] Spindeldreier CK, Schrenk O, Bakenecker et al, "Radiation dosimetry in magnetic fields with Farmer-type ionisation chambers: determination of magnetic field correction factors for different magnetic field strengths and field orientations," *Phys Med Biol*, vol. 62, no. 16, pp. 6708–6728, 2017.

[138] Reynolds M, Fallone BG, Rathee S, "Technical Note: Response measurement of select radiation detectors in magnetic fields," *Med Phys*, vol. 42, no. 6, pp. 2837–2840, 2015.

[139] O'Brien DJ, Dolan J, Pencea S, Schupp N, Sawakuchi GO, "Relative dosimetry with an MR-linac: Response of ion chambers, diamond, and diode detectors off-axis, depth dose, and output factor measurements," *Med Phys*, vol. 45, no. 2, pp. 884–897, 2018.

[140] Woodings SJ, Wolthaus JWH, van Asselen B et al, "Performance of a PTW 60019 microDiamond detector in a 1.5T MRI-linac," *Phys Med Biol*, vol. 63, p. (9pp.), 2018.

[141] Wegener S, Weick S, Sauer OA, "Influence of a transverse magnetic field on the response of different detectors in a high energy photon beam near the surface," *Z Med Phys*, vol. 29, no. 1, pp. 22–30, 2018.

[142] Smit K, Kok JGM, Lagendijk JJW, Raaymakers BW, "Performance of a multi-axis ionization chamber array in a 1.5 T magnetic field," *Phys Med Biol*, vol. 59, pp. 1845–1855, 2014.

[143] Perik TJ, Kaas JJ, Greilich S, Wolthaus JWH, Wittkamper FW, "The characterisation of a large multi-axis ionization chamber array in a 1.5 T MRI linac," *Phys Med Biol*, vol. 63, p. 225007 (9pp.), 2018.

[144] Gargett M, Oborn B, Alnaghy SJ et al, "A high resolution 2D array detector system for small-field MRI-linac applications," *Biomed Phys Eng*, vol. 4, p. 035041, 2018.

[145] Alnaghy SJ, Causer T, Gargett M, Roberts N, Petasecca M, Oborn BM, Rosenfeld AB, Holloway L, Metcalfe P, "A feasibility study for high-resolution silicon array detector performance in the magnetic field of a permanent magnet system," *Med Phys*, vol. 46, no. 9, pp. 4224–4232, 2019.

[146] Torres-Xirau I, Olaciregui-Ruiz I, Baldvinsson G, Mijnheer BJ, van der Heide UA, Mans A, "Characterization of the a-Si EPID in the unit MR-linac for dosimetric applications," *Phys Med Biol*, vol. 63, p. 025006 (9pp), 2018.

[147] Torres-Xirau I, Olaciregui-Ruiz I, van der Heide UA, Mans A, "Two-dimensional EPID dosimetry for an MR-linac: Proof of concept," *Med Phys*, vol. 46, no. 9, pp. 4193–4203, 2019.

[148] Williams M, Metcalfe P, "Radiochromic film dosimetry and its applications in radiotherapy," *AIP Conf Proc*, vol. 1345, pp. 75–99, 2011.

[149] Wen N, Lu S, Kim J et al, "Precise film dosimetry for stereotactic radiosurgery and stereotactic body radiotherapy quality assurance using Gafchromic EBT3 films," *Radiather Oncol*, vol. 11, no. 132, p. (11pp), 2016.

[150] Reynoso FJ, Curcuru A, Green O, Mutic S, Das IJ, Santanam L, "Technical Note: Magnetic field effects on Gafchromic-film response in MR-IGRT," *Med Phys*, vol. 43, no. 12, pp. 6552–6556, 2016.

[151] Delfs B, Schonfeld AA, Poppinga D et al, "Magnetic fields are causing small, but significant changes of the radiochromic EBT3 film response to 6 MV photons," *Phys Med Biol*, vol. 63, p. 035028, 2018.

[152] Barten DLJ, Hoffmans D, Palacios MA, Heukelom S, van Battum LJ, "Suitability of EBT3 Gafchromic film for quality assurance in MR-guided radiotherapy at 0.35 T with and without real-time MR imaging," *Phys Med Biol*, vol. 63, p. 165014 (10pp), 2018.

[153] Billas I, Bouchard H, Oelfke U, Duane S, "The effect of magnetic field strength on the response of Gafchromic EBT-3 film," *Phys Med Biol*, vol. 64, p. 06NT03 (9pp), 2019.

[154] Wooten HO, Green O, Yang M et al, "Quality of intensity modulated radiaiton therapy treatment plans using a ^{60}Co magnetic resononance image guidamce radiation therapy system," *Int J Radiat Oncol Biol Phys*, vol. 92, no. 4, pp. 771–778, 2015.

[155] Wooten HO, Rodriguez V, Green O, "Benchmark IMRT evaluation of a Co-60 MRI-guided radiation therapy system," *Radiat Oncol*, vol. 114, pp. 402–405, 2015.

[156] Hissoiny S, Ozell B, Bouchard H, Deprés P, "GPUMCD: A new GPU-oriented Monte Carlo dose calculation platform," *Med Phys*, vol. 38, no. 2, pp. 754–764, 2011.

[157] Goldman SP, Thurnball D, Johnson C, Chen JZ, Battista JJ, "Real-time fast inverse dose optimization for image guided adaptive radiation therapy - Enhancements to fast inverse dose optimization (FIDO)," *J Appl Phys*, vol. 105, p. 102008, 2009.

[158] St-Aubin J, Keyvanloo A, Vassiliev O, Fallone BG, "A deterministic solution of the first order linear Boltzmann transport equation in the presence of external magnetic fields," *Med Phys*, vol. 42, pp. 780–793, 2015.

[159] St-Aubin J, Keyvanloo A, Fallone BG, "Discontinuous finite element space-angle treatment of the first order linear Boltzmann transport equation with magnetic fields: application to MRI-guided radiotherapy," *Med Phys*, vol. 43, pp. 195–204, 2016.

[160] Yang R, Fallone BG, St-Aubin J, "An energy-adaptive finite element angular discretization towards a fast deterministic fose calculation in magnetic fields," *Med Phys*, vol. 23, p. e562, 2018.

[161] Yang R, Zelyak O, Fallone BG, St-Aubin J, "A novel upwind stabilized discontinuous finited element angular framework for deterministic dose calculations in magnetic fields," *Phys Med Biol*, vol. 63, p. 035018, 2018.

[162] Yang R, Santos DM, Fallone BG, St-Aubin J, "A novel transport sweep architecture for efficient deterministic patient dose calculation in MRI-guided radiotherapy," *Phys Med Biol*, vol. 64, p. 185012 (14pp), 2019.

[163] Schrenk O, Spindeldreier CK, Burigo LN,Hoerner-Rieber J, Pfaffenberger A, "Effects of magnetic field orientation and strength on the treatment planning of nonsmall cell lung cancer," *Med Phys*, vol. 44, no. 12, pp. 6621–6631, 2017.

[164] Begg J, Alnaghy SJ, Causer T, Alharthi T, George A, Glaubes L, Dong B, Goozee G, Keall P, Jelen U, Liney G, Holloway L, "Technical Note: Experimental characterization of the dose deposited in parallel MRI-linacs at various magentic field strengths," *Med Phys*, 2019. https://doi.org/10.1002/mp.13767.

[165] Kawrakow I, Rogers DWO, "The EGSnrc System, a Status Report. In: Kling A., Baräo F.J.C., Nakagawa M., Távora L., Vaz P. (eds) Advanced Monte Carlo for Radiation Physics, Particle Transport Simulation and Applications.," *Springer, Berlin, Heidelberg*, pp. 135–140, 2001.

[166] Agostinelli S, Allison J, Amako K et al, "GEANT4 - a simulation toolkit," *Nucl. Inst. Meth.*, vol. 506, pp. 250–303, 2003.

[167] Malkov VN, Rogers DWO, "Charged particle transport in magnetic fields in EGSnrc," *Med Phys*, vol. 43, no. 7, pp. 4447–4458, 2016.

[168] Kirkby C, Stanescu T, Rathee S, Carlone M, Murray, Fallone BG, "Patient dosimetry for hybrid MRI-radiotherapy systems," *Med Phys*, vol. 35, no. 3, pp. 1019–1027, 2008.

[169] Malkov VN, Rogers DW, "Monte Carlo study of ionization chamber magnetic field correction factors as a function of angle and beam quality," *Med Phys*, vol. 45, no. 2, pp. 908–925, 2018.

[170] Raaijmakers AJE, Raaymakers BW, Lagendijk JJW, "Experimental verification of magnetic field dose effects for the MRI-accelerator," *Phys Med Biol*, vol. 52, pp. 4283–4291, 2007.

[171] O'Brien DJ, Roberts DA, Ibbott GS, Sawakuchi GO, "Reference dosimetry in magnetic fields: formalisation and ionization chamber correction factors," *Med Phys*, vol. 43, no. 8, pp. 4915–4927, 2016.

[172] Benedict SH, Yenice KM, Followill D et al, "Stereotactic body radiation therapy: The report of AAPM Task Group 101," *Med Phys*, vol. 37, no. 8, pp. 4078–4101, 2010.

[173] McGrath S, Matuszak MM, Yan D, Kestin LL, Martinez AA, Grills IS, "Volumetric modulated arc therapy for delivery of hypofractionated stereotactic lung radiotherapy: A dosimetric and treatment efficiency analysis," *Radiother Oncol*, vol. 95, no. 2, pp. 153–157, 2010.

[174] Wilbert J, Meyer J, Baier K et al, "Tumor tracking and motion compensation with an adaptive tumor tracking system (ATTS): System description and prototype testing," *Med Phys*, vol. 35, no. 9, pp. 3911–3921, 2008.

[175] Haas OCL, Skworcow P, Paluszczyszyn D, Sahih A, Ruta M, Mills JA, "Couch-based motion compensation: modelling, simulation and real-time experiments," *Phys Med Biol*, vol. 57, no. 18, pp. 5787–5807, 2012.

[176] Lang s, Zeimetz J, Ochsner G, Daners MS, Riesterer O, Klöck S, "Development and evaluation of a prototype tracking system using the treatment couch," *Med Phys*, vol. 41, no. 2, p. 021720, 2014.

[177] Oborn BM, Williams M, Bailey M, Carolan MG, "IMRT treatment monitor unit verification using absolute calibrated BEAMnrc and GEANT4 Monte Carlo simulations," *J Phys: Conf Ser*, vol. 489, no. 1, p. 012020, 2014.

[178] Seppendwoolde Y, Shirato H, Kitamura K et al, "Precise and real-time measurement of 3D tumor motion in lung due to breathing and heatbeat, measured during radiotherapy," *Int J Radiat Oncol Biol Phys*, vol. 53, pp. 822–834, 2002.

[179] Kutcher G, Coia L, Gillin M et al, "Comprehensive QA for radiation oncology: Report of AAPM Radiation Therapy Committee Task Group 40," *Med Phys*, vol. 21, no. 4, pp. 581–618, 1994.

[180] Arumugam S, Young T, Xing A, Thwaites D, Holloway L, "Benchmarking the gamma pass score using ArcCHECK for routine dosimetric QA of VMAT plans," *J Phys Conf Ser*, vol. 573, p. 012040, 2015.

[181] Computerized Imaging Reference Systems Inc, "Dynamic Thorax Phantom," 2013. http://www.cirsinc.com/products/all/18/dynamic-thorax-phantom/.

[182] Ong C, Verbakel WF, Cuijpers JP, Slotman BJ, Senan S, "Dosimetric impact of interplay effect on RapidArc lung stereotactic treatment delivery," *Int J Radiat Oncol Biol Phys*, vol. 79, no. 1, pp. 305–311, 2011.

[183] Stambaugh C, Nelms BE, Dilling T et al, "Experimentally studied dynamic dose interplay does not meaningfully affect target dose in VMAT SBRT lung treatments," *Med Phys*, vol. 40, no. 9, p. 091710, 2013.

[184] Li X, Yang Y, Li T, Fallon K, Heron E, Huq M.S., "Dosimteric effect of respiratory motion on volumetric-modulated arc therapy-based lung SBRT treatment delivered by TrueBeam machine with flattening filter-free beam," *J Appl Clin Med Phys*, vol. 14, no. 6, pp. 195–204, 2013.

[185] Mutaf Y, Scicutella C, Michalski D, "A simulation study of irregular respiratory motion and its dosimetric impact on lung tumors," *Phys Med Biol*, vol. 56, no. 3, pp. 845–859, 2011.

[186] Gholampourkashi S, Vujicic M, Belec J, Cygler JE, Heath E, "Experimental verification of 4D Monte Carlo simulations of dose delivery to a moving anatomy," *Med Phys*, vol. 44, no. 1, pp. 299–310, 2017.

[187] Schwarz M, Cattaneo GM, Marrazzo L, "Geometrical and dosimetrical uncertainties in hypofractionated radiotherapy of the lung: A review," *Phys Med*, vol. 36, pp. 126–139, 2017.

[188] Guckenberger M, Wilbert J, Meyer J, Baier K, Richter A, Flentje M, "Is a single respiratory correlated 4D-CT sufficient for evaluation of breathing motion?," *Int J Radiat Oncol Biol Phys*, vol. 67, pp. 1352–1359, 2007.

[189] Corradetti MN, Mitra N, Bonner Millar LP et al, "A moving target: Image guidance for stereotactic body radiation therapy for early-stage non-small cell lung cancer," *Pract Radiat Oncol*, vol. 3, pp. 307–315, 2013.

[190] Hansen CR, Bertelsen A, Riis HL, "Plan quality and delivery accuracy of flattening filter free beam for SBRT lung treatments," *Acta Oncol*, vol. 54, no. 3, pp. 422–427, 2015.

[191] Alharthi T, Pogson EM, Arumugam S, Holloway L, Thwaites D, "Pre-treatment verification of lung SBRT VMAT plans with delivery errors: Toward a better understanding of the gamma index analysis," *Phys Med*, vol. 49, pp. 119–128, 2010.

[192] Piper J, "SU-FF-I-68: Evaluation of An Intensity-Based Free-form Deformable Registration Algorithm," *Med Phys*, vol. 34, no. 6, pp. 2353–2354, 2007.

[193] Chan MKH, Kwong DLW, Ng SCY, Tong ASM, Tam EKW, "Experimental evaluation of the accuracy of 3D and 4D planning in robotic tracking SBRT for lung cancers," *Med Phys*, vol. 40, no. 4, p. 041712 (11pp.), 2013.

[194] Vlades G, Lee C, Tenn S et al, "The relative accuracy of 4D dose accumulation for lung radiotherapy using rigid dose projection verses dose recalculation on every breathing phase," *Med Phys*, vol. 44, no. 3, pp. 1120–1127, 2017.

[195] Samavati N, Velec M, Brock KK, "Effect of deformable registration uncertainty on lung SBRT dose accumulation," *Med Phys*, vol. 43, p. 233, 2016.

[196] Azcona JD, Huesa-Berral C, Moreno-Jiménez M,Barbés B, Javier Aristu J, Burguete J, "A novel concept to include uncertainties in the evaluation of stereotactic body radiation therapy after 4D dose accumulation using deformable image registration," *Med Phys*, vol. 46, no. 10, pp. 4346–4355, 2019.

[197] Aso T, Kimura A, Yamashita T, Sasaki T, "Optimization of patient geometry based on CT data in Geant4 for medical application," *Proc IEEE Nucl Sci Symp Conf Rec (NSS)*, vol. 4, pp. 2576–2580, 2007.

[198] PTW, "User manual. microDiamond type 60019. Technical Report," *PTW, PTW-Freiburg*, 2014. D930.131.00/02 en.

[199] The International Commission on Radiological Protection, "The biological basis for dose limitation in the skin. A report of a Task Group of Committee 1 of the ICRP," *Ann ICRP*, vol. 22, no. 2, pp. 1–104, 1992.

[200] Thorpe N, Rosenfeld A, Metcalfe P, Cutajar D, Cai M, "Development of quality assurance dosimetry systems for MRI brachytherapy and MRI-linac technology," *The Royal Australian and New Zealand College of Radiologists*, 2014. 10.1594/ranzcr2014/R-0280.

[201] Jong WL, Wong JHD, Ung NM et al, "Characterization of MOSkin detector for in vivo skin dose measurement during megavoltage radiotherapy," *J Appl Clin Med Phys*, vol. 15, no. 5, pp. 120–132, 2014.

[202] Qi Z, Deng X, Huang S, Zhang L, He Z, Li XA et al, "In vivo verification of superficial dose for head and neck treatments using intensity-modulated techniques," *Med Phys*, vol. 36, no. 1, pp. 59–70, 2009.

[203] Rosenfeld AB, "Advanced Semiconductor dosimetry in radiation therapy, In A. Rosenfeld (Eds.), Concepts and trends in medicial radiation dosimetry," *Melville, NY: American Institute of Physics*, pp. 48–74, 2011.

[204] Griessbach I, Lapp M, Bohsung J, Gademann G, Harder D, "Dosimetric characteristics of a new unshielded silicon diode and its application in clinical photon and electron beams," *Med Phys*, vol. 32, no. 12, pp. 3750–3754, 2005.

[205] Niroomand-Rad A, Blackwell C R, Coursey B M et al, "Radiochromic film dosimetry: Recommendations of AAPM Radiation Therapy Committee Task Group 55," *Med Phys*, vol. 25, no. 11, pp. 2093–2115, 1998.

[206] Report No. IEC-60976, "Medical electrical equipment - Medical electron accelerators - Functional performace characteristics," *International electrotechincal commission*, 1996.

[207] Report No. IEC-60977, "Medical electrical equipment - Medical electron accelerators in the range of 1 MeV to 50 MeV - Guidelines for funtional performance characteristics," *International electrotechincal commission*, 1989.

[208] Ciancaglioni I, Marinelli M, Milani E et al, "Dosimetric charaterization of a synthetic single crystal diamond detector in clinical radiation therapy small photon beams," *Med Phys*, vol. 39, no. 7, pp. 4493–4501, 2012.

[209] Ralston A, Tyler M, Liu P, McKenzie D, Suchowerska N, "Over-response of synthetic microDiamond detectors in small radiation fields," *Phys Med Biol*, vol. 59, pp. 5873–5881, 2014.

[210] Sorriaux J, Kacperekc A, Rossomme S et al, "Evaluation of Gafchromic(R) EBT3 films characteristics in therapy photon, electron and proton beams," *Phys Med*, vol. 29, pp. 599–606, 2013.

[211] Scott AJ, Kumar S, Nahum AE, Fenwick JD, "Characterizing the influence of detector density on dosimeter response in non-equlibrium small photon fields," *Phys Med Biol*, vol. 57, pp. 4461–4476, 2012.

[212] Lárraga-Gutiérrez JM, Ballesteros-Zebadúa P, Rodríguez-Ponce M, García-Garduño OA, de la Cruz OOG, "Properties of a commercial PTW-60019 synthetic diamond detector for the dosimetry of small radiotherapy beams," *Phys Med Biol*, vol. 60, no. 2, pp. 905–924, 2015.

[213] Wang Y, Khan MK, Ting JY, Easterling SB, "Surface dose investigation of the flattening filter-free photon beams," *Int J Radiat Oncol Biol Phys*, vol. 83, no. 2, pp. e281–e285, 2012.

[214] Ding GX, "Energy spectra, angular spread, fluence profiles and dose distributions of 6 and 18 MV photon beams: results of Monte Carlo simulations for a Varian 2100EX accelerator," *Phys Med Biol*, vol. 47, pp. 1025–1046, 2002.

[215] Villarreal-Barajas JE, Khan RFH, "Energy response of EBT3 radiochromic films: implications for doimetry in kilovoltage range," *J Appl Clin Med Phys*, vol. 15, no. 1, pp. 331–338, 2014.

[216] Oborn BM, Metcalfe PE, Butson MJ, Rosenfeld AB, "High resolution entry and exit Monte Carlo dose calculations from a linear accelerator 6 MV beam under influence of transverse magnetic fields," *Med Phys*, vol. 36, no. 8, pp. 3549–3559, 2009.

[217] Oborn BM, Metcalfe PE, Butson MJ, Rosenfeld AB, "Monte Carlo characterizarion of skin doses in 6 MV transverse field MRI-linac systems: Effect of field size, surface orientation, magnetic field strength, and exit bolus," *Med Phys*, vol. 37, no. 10, pp. 5208–5217, 2010.

[218] van Heijst TCF, den Hartogh MD, Lagendijk JJW, van den Bongard HJGD, van Asselen B, "MR-guided breast radiotherapy feasibility and magnetic-field impact on skin dose," *Phys Med Biol*, vol. 58, no. 17, pp. 5917–5930, 2013.

[219] Liney GP, Jelen U, Byrne H et al, "Technical Note: The first live treatment on a 1.0 Tesla inline MRI-linac," *Med Phys*, vol. 46, no. 7, pp. 3254–3258, 2019.

[220] Green OP, Goddu S, Mutic S, "Commissioning and Quality Assireance of the First Commercial Hybrid MRI-IMRT System," *Med Phys*, vol. 39, no. 6, p. 3765, 2012.

[221] Smit K, "Dosimetry for the MR-Linac," *Doctoral Dissertation*, 2015.

[222] Woodings SJ, Bluemink JJ, de Vries JHW et al, "Beam characterisation of the 1.5T MRI-linac," *Phys Med Biol*, vol. 63, p. 085015 (12pp), 2018.

[223] Dutreix J, Dutreix A, "Film dosimetry of high-energy electrons," *In: Annals of th e New York Academy of Science*, vol. 161, no. 1, pp. 33–43, 1969.

[224] Suchowerska N, Hoban P, Butson M, Davidson A, Metcalfe P, "Directional dependence in film dosimetry: radiographic and radiochromic film," *Phys Med Biol*, vol. 46, no. 5, pp. 1391–1397, 2001.

[225] Jelen U, Dong B, Begg J, Roberts N, Whelan B, Keall P, Liney G, "Dosimetric optimization and commissioning of a high field inline MRI-linac," *Front Oncol*, vol. 10:136, 2020.

[226] Report No. IEC-60731, "Medical Electrical Equipment – Dosimeters With Ionization Chambers as Used in Radiation Therapy," *International electrotechincal commission*, 1997.

[227] Starkschall G, Steadham RE, Popple RA, Ahmad S, Rosen II, "Beam-commissioning methodology for a three-dimensional

convolution/superposition photon dose algorithm," *J Appl Clin Med Phys*, vol. 1, no. 1, pp. 8–27, 2000.

[228] Philips Medical Systems, *Pinnacle*^{3} *Physics, Release 9.8*. 4598 004 22371 A, 2013.

[229] Bedford JL, Chulds PJ, Nordmark Hansen V, Mosleh-Shirazi MA, Verhaegen F, Warrington AP, "Commisioning and quality assurance of the Pinnacle^3 radiotherapy treatment planning system for external beam photons," *Br J Radiol*, vol. 76, pp. 163–176, 2003.

[230] Saenz DL, Narayanasamy G, Cruz W, Papanikolaou N, Stathakis S, "Pinnacle^3 modeling and end-to-end dosimetric testing of a Versa HD linear accelerator with the Agility head and flattening filter-free modes," *J Appl Clin Med Phys*, vol. 17, no. 1, pp. 192–206, 2016.

[231] Keall PJ, Siebers JV, Libby B, Mohan R, "Determining the incident electron fluence for Monte Carlo-based photon treatment plannning using a standard measured data set," *Med Phys*, vol. 30, no. 4, pp. 574–582, 2003.